University of Tennessee, Knoxville

TRACE: Tennessee Research and Creative Exchange

Doctoral Dissertations

Graduate School

8-2001

Growth and characterization of epitaxially aligned titanium nitride thin films on silicon by orthogonally crossed-beam pulsed laser deposition

Sukill Kang

Follow this and additional works at: https://trace.tennessee.edu/utk_graddiss

Recommended Citation

Kang, Sukill, "Growth and characterization of epitaxially aligned titanium nitride thin films on silicon by orthogonally crossed-beam pulsed laser deposition. " PhD diss., University of Tennessee, 2001.
https://trace.tennessee.edu/utk_graddiss/8525

This Dissertation is brought to you for free and open access by the Graduate School at TRACE: Tennessee Research and Creative Exchange. It has been accepted for inclusion in Doctoral Dissertations by an authorized administrator of TRACE: Tennessee Research and Creative Exchange. For more information, please contact trace@utk.edu.

To the Graduate Council:

I am submitting herewith a dissertation written by Sukill Kang entitled "Growth and characterization of epitaxially aligned titanium nitride thin films on silicon by orthogonally crossed-beam pulsed laser deposition." I have examined the final electronic copy of this dissertation for form and content and recommend that it be accepted in partial fulfillment of the requirements for the degree of Doctor of Philosophy, with a major in Physics.

T. A. Callcott, Major Professor

We have read this dissertation and recommend its acceptance:

D. H. Lowndes, James R. Thompson, John J. Quinn

Accepted for the Council:

Carolyn R. Hodges

Vice Provost and Dean of the Graduate School

(Original signatures are on file with official student records.)

To the Graduate Council:

I am submitting herewith a dissertation written by Sukill Kang entitled " Growth and Characterization of Epitaxially Aligned Titanium Nitride Thin films on Silicon by Orthogonally Crossed-Beam Pulsed Laser Deposition." I have examined the final copy of this dissertation for form and content and recommend that it be accepted in partial fulfillment of the requirements for the degree of Doctor of Philosophy, with a major in Physics.

T. A. Callcott, Major Professor

We have read this dissertation

and recommend its acceptance:

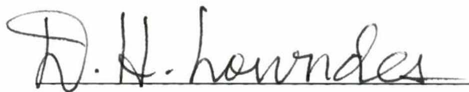

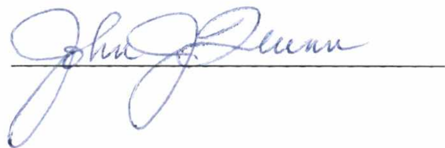

Accepted for the Council:

Vice Provost and Dean of Graduate Studies

GROWTH AND CHARACTERIZATION OF EPITAXIALLY ALIGNED TITANIUM NITRIDE THIN FILMS ON SILICON BY ORTHOGONALLY CROSSED-BEAM PULSED LASER DEPOSITION

A

Dissertation

Presented for the

Doctor of Philosophy Degree

The University of Tennessee, Knoxville

Sukill Kang

August 2001

To my parents

ACKNOWLEDGMENTS

I would like to express my sincere appreciation to Dr. T. A. Callcott, Dr. D. H. Lowndes, Dr. J. J. Quinn, and Dr. J. R. Thompson for kindly serving on my dissertation committee. Especially, I would like to thank Dr. Callcott for serving as a supervisory committee chairman. I am also grateful to Dr. Lowndes for his constant professional, educational guidance, encouragement and support during my research.

It has been my great privilege to work with Dr. C. M. Rouleau and his valuable discussions and assistance regarding this research are gratefully acknowledged. I also would like to thank Dr. M. Kim for theoretical calculations and EELS measurement. I also want to thank Dr. J. Budai for X-ray diffraction measurements.

Finally, I would like to thank my parents and family for their love and support during the course of my studies.

ABSTRACT

TiN thin films have been grown epitaxially on Si(111) substrates by crossing orthogonally a pulsed molecular N_2 jet with a pulsed-laser generated Ti plume. This so-called reactive crossed-beam pulsed laser deposition technique was demonstrated as a modification of conventional pulsed laser deposition and was used to grow high quality binary compound materials. Time-of-flight (TOF) measurements of species impinging onto the substrate were performed using an *in-situ* ion probe, and these measurements were used to optimize the growth conditions. Average plume kinetic energies ranged from 45 to 155 eV. Under essentially fixed N_2 jet conditions, the crystallographic quality of the films was found to be a stronger function of kinetic energy than growth temperature, with optimal films resulting for a plume mean kinetic energy of ~ 92 eV and substrate temperatures near 750 °C.

Scattering processes within the interaction regime were explained by Singh's model and it was determined that the processes between the laser plume and the pulsed gas expansion were responsible for the enhanced reactivity in crossed-beam PLD.

Film-growth mechanisms and microstructure were investigated using *in-situ* reflection high energy electron diffraction (RHEED), scanning electron microscopy (SEM), high-resolution transmission electron microscopy (HR-TEM), and scanning transmission electron microscopy (STEM). It was found that TiN thin films grow essentially in a Stranski-Krastanov growth mode under optimal growth conditions. Although TiN is highly mismatched with respect to Si (lattice constant mismatch of

22.3%), single crystal TiN/Si heterostructures are entirely feasible through a process known as domain-matching epitaxy. The epitaxial relationship between TiN and Si by domain-matching epitaxy is discussed in detail in this thesis.

The crystalline quality and electrical properties of the films were investigated using X-ray diffraction and four-point Van der Pauw measurements, respectively. Films grown under optimal conditions were highly textured and had mosaic spreads of ~18 arc-min and ~26 arc-min for a rocking curve around the TiN(111) pole and a ϕ-scan through the TiN(002) pole, respectively. All the films showed metallic behavior with resistivities that varied linearly with temperature above 75 K. The best film had a room temperature resistivity of 3.76 μΩ-cm. Implications of low-resistivity epitaxial TiN/Si heterostructure device fabrication are discussed.

Full-Potential Linearized Augmented Plane Wave (FLAPW) density functional theory (DFT) calculations, as implemented in the WIEN97 codes, have been employed to compare experimental electron energy loss spectroscopy (EELS) results with theoretical calculations since the cross section of electron near-edge structure (ELNES) is proportional to the unoccupied density of states. The implications of these results are discussed.

TABLE OF CONTENTS

Chapter 1 INTRODUCTION..1

Chapter 2 PULSED LASER DEPOSITION (PLD) SYSTEM AND THEORETICAL MODEL OF THE PLD PROCESS........................6

2.1. Conventional Pulsed Laser Deposition..6

2.1.1. The advantages and disadvantages of PLD..............................6

2.2. Physics and Theoretical Model of the PLD Process........................11

2.2.1. Interaction of the laser beam with the target material..................13

2.2.2. Plasma generation and three-dimensional isothermal expansion.......15

2.2.3. Adiabatic plasma expansion and recondensation.........................24

Chapter 3 REACTIVE CROSSED-BEAM PULSED LASER DEPOSITION AND DEPOSITION SYSTEM CONSTRUCTION........................28

3.1. General Background..28

3.2. Reactive Scattering Process...32

3.3. Preparation of a Reactive Crossed-Beam PLD Growth System...............41

3.3.1. Target carousel...46

3.3.2. Substrate holder and heater..46

3.3.3. Pulsed-valve system..48

3.3.4. Laser and optics..48

3.3.5. Ion probe..50

3.3.6. Pumping, vacuum-control and gas-flow systems..............................50

3.3.7. Temperature controller...53

Chapter 4 CHARACTERIZATION TECHNIQUES FOR TiN THIN FILMS.........55

4.1. Thickness Determination...55

4.2. Atomic Force Microscopy (AFM)..56

4.3. Scanning Electron Microscopy (SEM)...58

4.4. Transmission Electron Microscopy (TEM)..61

4.5. High-Resolution Scanning Transmission Electron Microscopy (STEM)..63

4.6. Electron Energy Loss Spectroscopy (EELS).......................................65

4.7. X-Ray Diffraction (XRD)..66

4.8. Energy Dispersive X-ray (EDX) Analysis...68

4.9. Reflection High Energy Electron Diffraction (RHEED).......................69

4.10. Electrical Resistivity..71

Chapter 5 TiN THIN-FILM GROWTH BY CROSSED-BEAM REACTIVE PLD AND ITS CHARACTERIZATION...74

5.1. Substrate Preparation..74

5.1.1. Substrate temperature calibration...74

5.1.2. Substrate cleaning...76

5.2. TiN Film Growth...80

5.3. Time-of-Flight (TOF) Measurements..........81

5.4. Epitaxial Growth of TiN Thin Films..........83

5.4.1. Thin film growth modes..........83

5.5. RHEED Analysis..........88

5.6. X-Ray Diffraction Analysis..........92

5.6.1. Structure of lattice-mismatched systems..........92

5.6.2. Dependence of film quality on the kinetic energy of the ablated species..........105

5.7. Surface Morphology Analysis..........105

5.8. Epitaxial Growth in a Large-Lattice-Mismatch System..........120

5.9. Theoretical Calculations..........130

5.10. Electrical Resistivity Measurement and Analysis..........139

Chapter 6 CONCLUSION..........147

6.1. Principal Results of This Work..........147

6.2. Suggestions for Future Work..........149

REFERENCES..........150

VITA..........160

LIST OF FIGURES

Figure 2.1. Schematic diagram of a pulsed laser deposition system: T = target, S = substrate....7

Figure 2.2. Schematic drawing of laser window apparatus for preventing window coating....12

Figure 2.3. Evolution of the degree of ionization of a Ti plume by inverse bremsstra -hlung during the irradiation with a 10 J/cm^2, 20-ns laser pulse duration at 248 nm for different initial plasma temperatures, calculated using the Saha equation, Eq. (2.3) (From Willmott et. al)....18

Figure 2.4. Schematic diagram showing the density (n), pressure (P) and velocity (v) gradients employed in Singh's model. The density and pressure are linearly decreasing from the target surface while the velocity is linearly increasing....22

Figure 3.1. Principal setup of orthogonally crossed-beam pulsed-laser deposition......31

Figure 3.2. Change in visual image of a YSZ ablation plume propagating into a vacuum (above) and crossed with O_2 gas pulse (below, ⊗: O_2 gas-pulse direction)....33

Figure 3.3. Different time-of-flight signals in vacuum as a function of laser energy density on the Ti target....35

Figure 3.4. TOF signals with different laser delays at fixed 2.0 μs vacuum TOF while the gas pulse and the laser plume are crossing....36

Figure 3.5. Velocity components before and after an elastic collision.....................38

Figure 3.6. Face A and side view of PLD chamber..43

Figure 3.7. Schematic diagram of the reactive crossed-beam PLD system..............45

Figure 3.8. Schematic diagram of the target carousel flange assembly for *in-situ* multilayer deposition..47

Figure 3.9. Schematic diagram of the rotating substrate heater assembly designed for the PLD process..49

Figure 3.10. Schematic drawing of the re-imaging optics and beam lines used in the crossed-beam PLD technique..51

Figure 3.11. Home-made ion probe circuit for the time-of-flight (TOF) measurements...52

Figure 3.12. Home-made temperature controller circuit for the substrate heater.........54

Figure 4.1. AFM principle..57

Figure 4.2. Schematic drawing of AFM feed back loop.......................................59

Figure 4.3. Electron and photon signals during electron-beam impingement on the specimen surface..60

Figure 4.4. Schematic ray diagram in the TEM under imaging and diffraction conditions...62

Figure 4.5. Schematic drawing of STEM...64

Figure 4.6. A X-ray diffractometer. a) block diagram and b) schematic drawing of the Picker 4-circle diffractometer geometry and relevant angles..........67

Figure 4.7. A schematic drawing of a RHEED system, with a beam of electrons

coming from an electron gun, impinging at grazing incidence onto the surface of a film, and forming a diffraction pattern on a phosphor screen..70

Figure 4.8. Schematic drawing of home-made Hall effect measurement system...72

Figure 4.9. Van der pauw method for measuring electrical resistivity...................73

Figure 5.1. Plot of silicon substrate surface temperatures obtained using optical pyrometry vs. monitored thermocouple temperatures...............75

Figure 5.2. RHEED patterns recorded at various temperatures along the <110> azimuth of Si...78

Figure 5.3. Ablated species time-of-Flight versus the delay between the pulsed valve driver trigger and the laser trigger.................................82

Figure 5.4. Three basic growth modes. (a) layer by layer (Frank-Van der Merwe), (b) island (Volmer-Weber), and (c) Stranski-Krasstanov. 86

Figure 5.5. Schematic of a cap-shaped nucleus on a substrate surface..................87

Figure 5.6. RHEED patterns with different TOFs. (2×2) structure were observed. The azimuth of the electron beam is parallel to the [110] direction...90

Figure 5.7. Illustration of a lattice-mismatched heterostructure that is either strained or unstrained (relaxed to the bulk lattice constant)..............93

Figure 5.8. Illustration of the angle ψ relative to the sample surface for measuring lattice parameters (N_s = normal to the sample surface,

N_r = normal to planes reflecting the x-ray beam)....................................96

Figure 5.9. Lattice parameters as a function of the angle ψ for different times-of-flight (TOF). Lattice constant were measured while varying the angle ψ. Out-of-plane lattice constants, a(⊥), were obtained at ψ=0° and in-plane lattice constants, a(||), were obtained at ψ=90°, as listed in Table 5.2....................................97

Figure 5.10. Dependence of tetragonal distortion on different times-of-flight (TOFs)....................................99

Figure 5.11. X-ray θ-2θ diffraction pattern for TiN grown with a 2.6 μs TOF....................................100

Figure 5.12. X-ray rocking curve and phi-scan of TiN film grown with (a) a 2.0 μs TOF, (b) a 2.6 μs TOF, (c) a 3.3 μs TOF, and (d) a 3.7 μs TOF....................................101

Figure 5.13. TOF-dependence of rocking curve and mosaic spread....................................106

Figure 5.14. AFM images of a TiN film grown at T=750 °C with (a) a 2.0 μs TOF, (b) a 2.6 μs TOF, (c) a 3.3 μs TOF, and (d) a 3.7 μs TOF....................................107

Figure 5.15. SEM micrograph of a TiN film grown at 750 °C with a 2.0 μs TOF....................................112

Figure 5.16. Target morphology for (a) bare target, (b) 2.0 μs TOF (the corresponding laser energy density on the target was 4.11 J/cm^2), (c) with a 2.6 μs TOF (2.86 J/cm^2), (d) with a

3.3 μs TOF (2.16 J/cm^2), and (e) with a 3.7 μs TOF
(1.74 J/cm^2)..113
Figure 5.17. SEM micrograph of a TiN film grown at 750 °C with a 2.6 μs TOF..117
Figure 5.18. SEM micrograph of a TiN film grown at 750 °C with a 3.3 μs TOF..118
Figure 5.19. SEM micrograph of a TiN film grown at 750 °C with a 3.7 μs TOF..119
Figure 5.20. Schematic Illustration of domain-matching epitaxial growth in large-lattice mismatch system..121
Figure 5.21. Electron diffraction pattern from TiN/Si interface. (a) SAED pattern and (b) corresponding indexed pattern (TiN: open circles, Si: solid circles)..123
Figure 5.22. High-resolution cross-sectional TEM lattice image from TiN/Si, viewed along [110]..124
Figure 5.23. STEM images of TiN/Si along [110]. (a) Bright-field and (b) Z-contrast dark-field..127
Figure 5.24. Schematic drawing of bonding between TiN and Si substrate..........128
Figure 5.25. EELS spectra as the scan line crossed the TiN/Si interface. Ti-*d* edges, $d\text{-}t_{2g}$ and $d\text{-}e_g$, were shown..129
Figure 5.26. Theoretical determination of an equilibrium lattice constant by the LDA. The predicted lattice constant is determined by

the minimum in the curve..133

Figure 5.27. Theoretical determination of an equilibrium lattice constant by the GGA. The predicted lattice constant is determined by the minimum in the curve..134

Figure 5.28. Calculated density of states (DOS) for TiN by LDA. (a) Ti and (b) N..136

Figure 5.29. Calculated density of states (DOS) for TiN by GGA. (a) Ti and (b) N..137

Figure 5.30. Convoluted density of states..140

Figure 5.31. Schematic electrical resistivity variation as a function of temperature for a metal. Thermal (phonon), defect, and impurity contributions are shown..142

Figure 5.32. Resistivities as a function of temperature of TiN films grown (a) with 2.0, 3.3, and 3.7 μs TOFs, and (b) with a 2.6 μs TOF. Inset shows T^5 dependence at low temperatures..143

LIST OF TABLES

Table 2.1. Comparison of fundamental deposition parameters for conventional growth techniques........8

Table 3.1. Targets used and films grown by crossed-beam reactive pulsed laser deposition. (Our case[a], and Willmott et al.[b])........42

Table 5.1. Specifications of Si substrates used to grow TiN thin films........77

Table 5.2. Lattice parameters, strains and distortions of the TiN films with different times-of-flight........98

Chapter 1

INTRODUCTION

The discovery and application of new materials is one of the major challenges in solid state and materials physics. Since most semiconductor technology is still based on silicon, many efforts have been made to incorporate novel materials into well-established silicon technology.

Research utilizing TiN thin films with Si has been conducted for over two decades. TiN is an attractive material and is both potentially and actually important for semiconductor thin-film devices since its excellent properties include high electrical conductivity, high surface hardness, high thermal stability, chemical inertness and good wear resistance. Because of its hardness and its corrosion resistance, TiN also is used widely as a hard coating material for tools and wear parts.[1-3] TiN thin films have a variety of applications such as diffusion barriers[4-6] in ultra large scale integration (ULSI) circuits, contact metallization in semiconductor devices,[7-9] a replacement for heavily doped polycrystalline Si as the gate electrodes in metal oxide-semiconductor field-effect transistors (MOSFETs)[10] and, when grown very thin, transparent conducting electrodes for flat-panel displays. TiN is also taken into consideration as a possible buffer layer for GaN/Si heterostructures because of its chemical similarity to GaN. Rouleau et. al.[11] have grown GaN thin films on Si and on sapphire (Al_2O_3) substrates using TiN buffer layers. Tiwari et al.[12] also have made epitaxial Pt films on Si(100) by using a TiN buffer layer grown by pulsed laser deposition (PLD). Such a buffer layer is potentially

technologically important since it would provide a means of integrating Si-based electronics with GaN-based optoelectronic devices.[13] TiN also is considered as a heat mirror due to its stability at high temperature and its high reflectivity in the infrared region.[14,15]

In spite of these promising attributes, most TiN films were polycrystalline with resistivity values higher than 50 μΩ-cm, which is too high to be used as a contact material in microelectronic devices. Also, polycrystalline TiN can cause a non-uniform p-n junction by impurity or dopant diffusion because of columnar structure in the TiN films.

Consequently, a number of attempts have been made by many research groups to grow single crystalline, highly conducting TiN thin films using various growth techniques including magnetron sputtering,[16-18] chemical vapor deposition (CVD),[19,20] ionized metal plasma (IMP) deposition,[21] energetic cluster impact deposition (ECID),[22] cathodic arc deposition (CAD),[23] and pulsed laser deposition (PLD).[12,24,25] Recently, single crystalline and low resistivity TiN thin films were fabricated on Si(100) by Chowdhury et al.[26] The room temperature resistivity was found to be ~15 μΩ-cm and the full-width-at half-maximum (FWHM) of the x-ray rocking curve was 0.75°.

For device applications, low-temperature film growth is critical for Si-based technology and there have been great demands for low temperature manufacturing processes for use in Si-based very large scale integration (VLSI) techniques. Conventional thermal CVD of TiN requires high temperatures ranging between 1050°C and 1200°C which is not applicable for submicron device designs. In the CVD process,

titanium tetrachloride, $TiCl_4$, together with a reducing agent, NH_3, is the most widely used for TiN film growth. This chemistry requires high-temperature processing which is not suitable at metallization levels. The incorporation of Cl atoms and impurities in the TiN films also is a major concern for long-term reliability of devices. Metalorganic chemical vapor deposition, (MOCVD) was also introduced for TiN film growth. In this method, tetrakis dimethylamido titanium (TDMAT), $Ti[N(CH_3)_2]_4$ and tetrakis diethylamido titanium (TDEAT), $Ti[N(CH_2CH_3)_2]_4$ are used frequently as the metalorganic precursors. The grown films, however, show high electrical resistivity (> 2000 μΩ-cm) and significant high levels of impurities such as oxygen and carbon.[27] Plasma enhanced chemical vapor deposition (PE- CVD) also has been introduced[28] to minimize the impurity content and for lowering the growth temperature. However, there were particle formation and poor step coverage because of the fast reaction in the gas phase. PLD, which is known as a relatively low temperature growth technique, was introduced as a possible alternative for TiN growth to overcome these problems.

The PLD technique was demonstrated for the first time by Smith and Tuner [29] and became known as a promising growth technique when Ge heteroepitaxy at 300 °C was demonstrated by Sankur et al.,[30] and Josephson junction devices made from cuprate superconductors were fabricated by Gross et al.[31] Since then, PLD has been used extensively by many research groups to grow compound semiconductors, multi-component oxides and nitrides, ceramic superconductors and dielectric materials. A detailed description of the PLD technique is presented in Chapter 2.

Even though the conventional PLD technique has many advantages for film growth, there also have been several problems with it. Commonly available target materials for PLD are usually hot-pressed sintered compound targets which sometimes deteriorate the quality of grown films because of low target purity and density. For semiconductor applications, these are critical problems since high chemical purity and highly crystalline thin films are needed for device fabrication. However, for binary compounds, these problems can be overcome completely by ablating a melt-cast high purity elemental metal target through a high purity reactive gas. For example, Xiao et al.[32] have grown high quality GaN thin films by ablation of a liquid Ga target in NH_3 background gas. Also, high quality AlN films were successfully grown using a high purity metallic Al target in reactive nitrogen gas by Verardi et al.[33]

As an adaptation of PLD, a *pulsed* gas was introduced for the first time by Gupta et al.[34] for $YBa_2Cu_3O_{7-\delta}$ thin film growth. Using this pulsed supersonic gas jet, they lowered the average background gas pressure (~ 10^{-4} torr) so much that *in situ* vacuum characterization techniques, such as reflection high energy electron diffraction (RHEED), could be used during the growth. Recently, Willmott et al.[35] have refined this approach and have introduced a reactive crossed-beam PLD method to grow CuO on a MgO substrate. Not only does the method promote a region of highly dense mixing where the laser ablation plume and the molecular beam cross, followed by a nearly collisionless expansion of the activated species toward the substrate, but because of the low time-averaged background pressure in the chamber, the substrate is not exposed to high impurity partial pressures, as would be the case in the static-pressure technique.

In this research, the growth of high quality TiN(111) thin films on Si(111) substrates was carried out by orthogonally crossed-beam reactive pulsed laser deposition, using a conventional PLD chamber adapted for the reactive crossed-beam technique. It should be noted that, in contrast to Willmott et al.,[35] the ablation plume and the pulsed jet crossed orthogonally in this work, and the target was a standard metallic disk. To the author's best knowledge, these TiN/Si(111) heterostructures are the best grown to date.

This dissertation is divided into six chapters. In Chapter 2, general and fundamental features of pulsed laser deposition are described and a theoretical model for this technique is reviewed. Chapter 3 provides the general background on PLD with the pulsed-beam technique. The modified pulsed laser deposition system, Orthogonally Crossed-Beam Reactive Pulsed Laser Deposition (OCBR-PLD), used in this research also is described. TiN thin film characterization techniques are described in Chapter 4. In Chapter 5, the experimental details for epitaxial growth of TiN thin films are described and the results also are presented and discussed. Finally, Chapter 6 presents and summarizes the conclusions and the suggestions drawn from this research.

Chapter 2

PULSED LASER DEPOSITION (PLD) SYSTEM AND THEORETICAL MODEL OF THE PLD PROCESS

2.1. Conventional Pulsed Laser Deposition

Pulsed Laser Deposition (PLD) is a film-growth technique in which target materials are ablated by high-power laser pulses to generate a plasma plume and deposit the materials on a substrate. This technique has become known as the simplest method for rapid protyping of films. A schematic diagram of a PLD system is shown in Fig. 2.1. It mainly consists of a vacuum chamber, a substrate holder and a target holder. A high-intensity energetic laser beam (UV-excimer laser) is focused onto the target through the lens and window. Where the laser spot impinges on the target, the surface of the target is vaporized and produces the ablation plasma plume which consists ideally of atoms, ions, and electrons, but may include small molecules and particulates. The plume rapidly expands in the forward direction toward the substrate, and the plume components recondense on the substrate to form a thin film.

2.1.1. The advantages and disadvantages of PLD

PLD has advantages and disadvantages over other thin film deposition techniques.[36] Brief comparisons are listed in Table 2.1 and the advantages of the PLD technique are as follows:

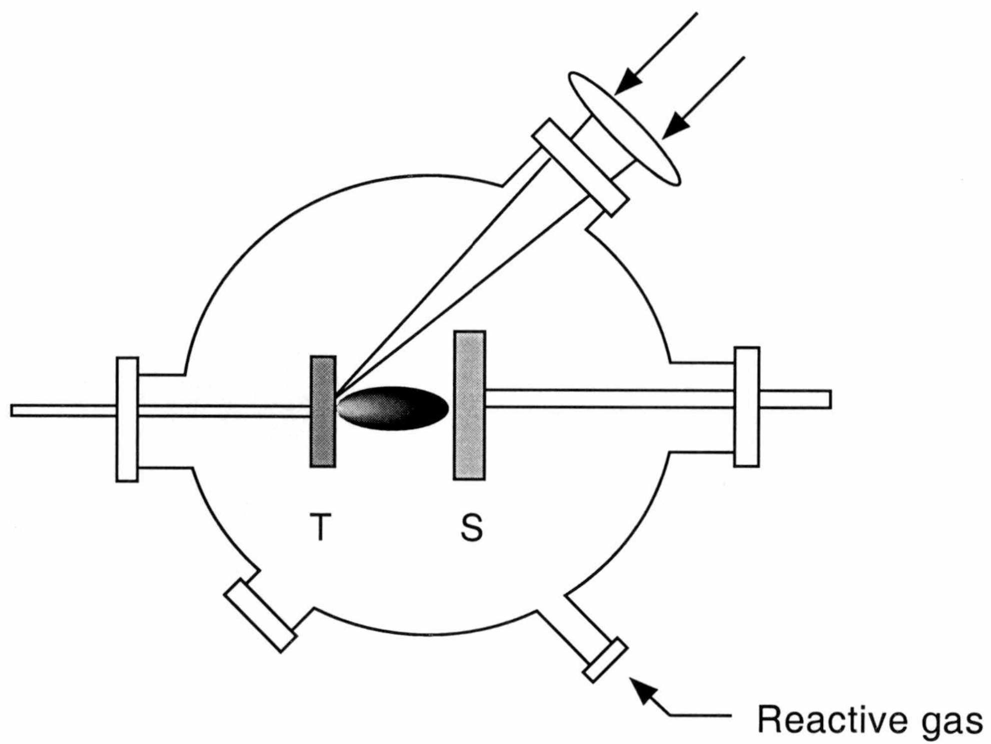

Figure 2.1. Schematic diagram of a pulsed laser deposition system:

T = target, S = substrate.

Table 2.1. Comparison of fundamental deposition parameters for conventional growth techniques.

Growth technique	Deposition rate (Å/s)	Multi-component rate control	Energy range per deposited atom (eV)	Cost	Pressure range (Torr)
Molecular Beam Epitaxy (MBE)	3	Moderate	≤ 0.1	High	10^{-11} - 10^{-9}
Chemical Vapor Deposition (CVD)	20	Moderate	≤ 0.1	Low	10^{-3} - 1
Pulsed Laser Deposition (PLD)	20	Easy	1 – 1000	Low	10^{-9} - 1

(1) Multi-component thin film growth

PLD is the easiest and most convenient method among many techniques for growing chemically complex multilayered epitaxial heterostructures and superlattices containing high temperature superconductors, ferroelectrics, and electrooptic materials using several different targets.

(2) High deposition rate and low cost

High growth rates can be achieved by using a high-power excimer laser. Rates up to 150 Å/s over 4-inch diameter have been reported.[37] Also, less source material is

needed because most of the ablated plume is strongly forward-directed. In the case of expensive and rare materials, the target can be made relatively small since the laser beam can be localized into a small spot. The capital cost for PLD equipment is relatively low in comparison with other growth techniques, the largest cost being the pulsed laser.

(3) Novel materials fabrication

Novel or metastable materials that can't be fabricated by near-equilibrium thermal processing can be produced in PLD by generation of plasma plumes whose electronic states are far from chemical equilibrium.

(4) Low substrate temperature

The generated plume possesses both kinetic energy and potential energy that increases the adatom mobility and sticking coefficients[38] on the surface of the film. Generally, the kinetic energies of impinging ions in PLD are 1 - 100 eV, whereas they are 0.1 eV in the CVD and MBE cases. So, film nucleation can be enhanced[39] and epitaxial film growth can be achieved at low substrate temperature.

(5) Stoichiometric growth and compatibility

The ratios of the elemental components are the same in the target material and in the film grown on the substrate, even for chemically complex materials. Many kinds of solid materials can be ablated so that films grown by other growth techniques often can be made also by the PLD process.

(6) Kinetic energy control

The kinetic energy of the ablated species impinging into the substrate can be varied to a limited degree by changing laser power density and ambient gas pressure. Species with high incident momentum can cause defects in the films. By increasing background gas pressure, the momentum of impinging species can be reduced, and so are the defects in the films.

There also are some limitations in the PLD technique:

(1) Particulates

Deposition of micron-sized particulates on the films during their growth is a major problem in PLD. These particulates, together with point defects produced by energetic species, are the main obstacle for semiconductor device applications because the particulates produce gaps in film continuity and interfere with planar processing. Usually, poorly sintered ceramic targets are the cause of particulates. In the case of metallic targets (e.g. Ti), molten droplets which result from subsurface boiling also cause particulates. The density and size of particulates depend on the laser energy density, E_d, and the surface morphology of the target. A mechanical particle filter and synchronized shutter can be used to block particles and other agglomerates.[40] The off-axis PLD method has been employed by Holzapfel et al.[41] to reduce the particulate problems.

(2) Limitation in large-area growth

For the purpose of commercial production, large-area growth with good film-thickness and compositional uniformity is needed. The PLD technique has been limited for this purpose because of its narrow plume angular distribution over the substrate area. However, a couple of approaches by Greer,[42] Erinton,[43] and Eddy[44] have been used to scan the ablation plume over the substrate and films have been grown on substrates as large as 15 cm to date.

(3) Laser entrance window coating

During film growth, a film is also often deposited on the laser entrance window. Coating rates are different for various target materials and deposition conditions. This is a serious problem because it reduces transmission of the laser radiation and causes poor laser fluence on the target and poor growth rate. For nonmetallic ceramic targets, the deposit can be removed from the laser window by increasing the laser power. For metallic targets, however, the window can be damaged by the high ablation thresholds of most metals. So, it is necessary to clean the laser window by optical polishing after every run. Because of this inconvenience, an alternative method was considered in this work. The problem was solved by installing a small turbomolecular pump (THP 062, Blazer-Pfeiffer Co.) and two apertures between the laser window and the target holder. Ablated species and gas molecules moving toward the laser window were reduced greatly by the two apertures and those that passed the first apertures were pumped away by the turbo-pump. No window coating was found after this modification; a schematic diagram is shown in Fig. 2.2.

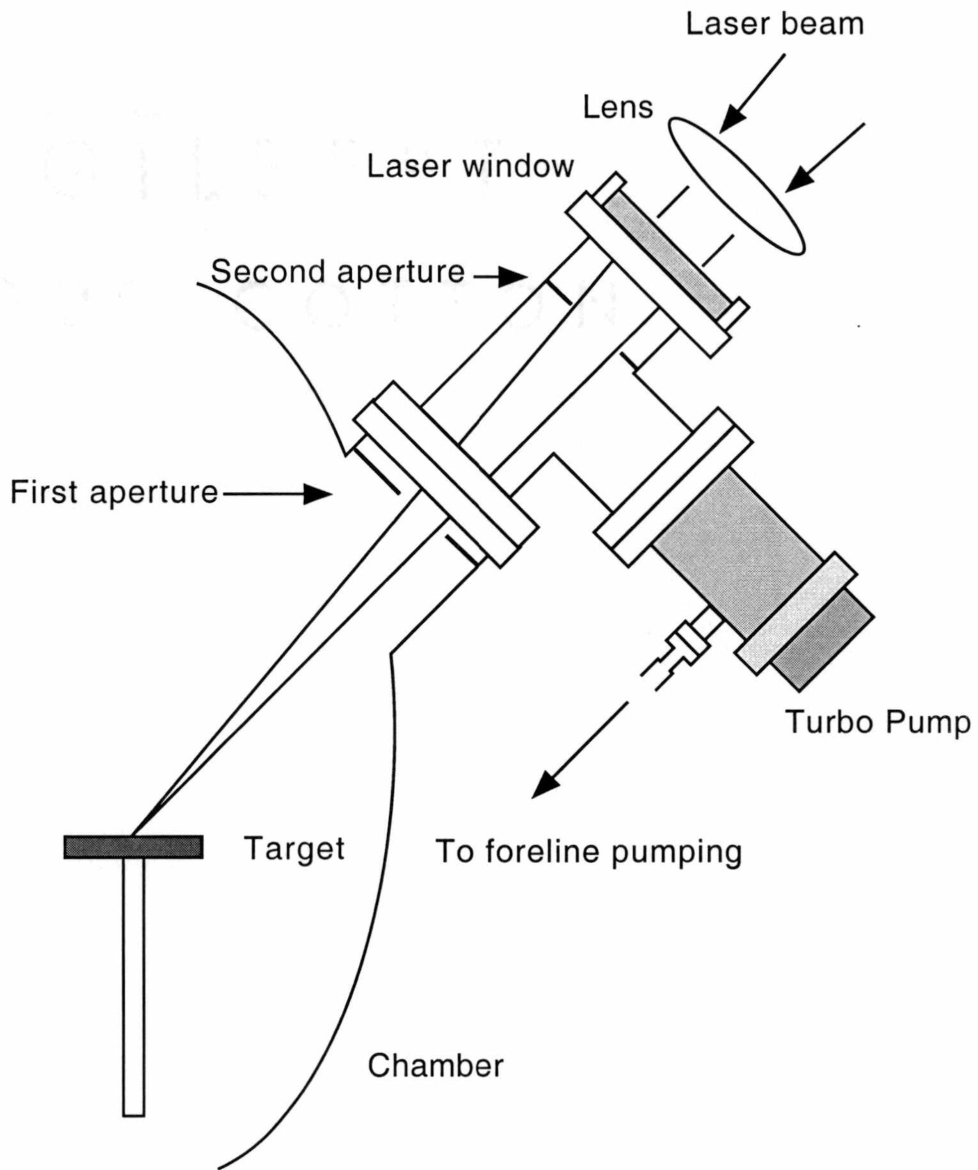

Figure 2.2. Schematic drawing of laser window apparatus for preventing window coating.

2.2. Physics and Theoretical Models of the PLD Process

Singh et al.,[45,46] and Kelly et al.[47] have developed theoretical models for simulating laser-plasma-solid interactions. In their model, Singh et al. classified the physical process of PLD for thin film growth into three separate interaction regimes, based on the nature of interaction of the laser beam with the target and the evaporated material:

- Interaction of the laser beam with the target material.
- Plasma generation and initial three-dimensional isothermal expansion by interaction of the incident laser beam with the *evaporated* target material.
- An anisotropic three-dimensional adiabatic expansion of the laser-induced plasma, leading to deposition of a thin film.

In this model, the first two processes occur when the target is ablated by the front of the laser pulse, while the last process starts after the laser pulse terminates. Also, the initial evaporation of the target material is assumed to be a thermal process, while the plasma generation, accompanied by absorption of the laser beam in the evaporated material, is considered to be highly non-thermal process. The kinetic energy of the evaporated species is much larger than the thermal equilibrium energy, resulting in a sharply forward-directed plasma expansion and deposition.

2.2.1. Interaction of the laser beam with the target material

The removal of target material by laser ablation depends on the coupling of the laser beam with the solid. Intense heating of the surface layers by a high-powered laser results in melting and evaporation of the surface layers. The material removal is controlled by the rate of thermal conduction through the lattice, and research on these thermal effects of interaction between laser beams and target materials has been extensively developed.[48,49] The thickness of the material heated by the laser beam is given as approximately ~ $(D\tau)^{1/2}$, where D is thermal diffusivity and τ is the laser pulse duration. When the excited electrons transfer their energy to the lattice in a few picoseconds, heating starts within the optical absorption depth of the material, $1/\alpha$, where α is the optical absorption coefficient. The reported values for the vaporization threshold energy density are 0.11 to 0.4 J/cm^2 depending on the surface morphology of a $Y_1Ba_2Cu_3O_{7-x}$ target[50,51], for example. When laser energy densities are applied above the vaporization threshold, the laser energy is absorbed in the surface layers to $\sim 1/\alpha$, while intense heating leads to vaporization within a thermal diffusion length of ~ $(D\tau)^{1/2}$. Using an energy balance consideration, the energy deposited by the laser beam should be equal to the energy needed to vaporize the target surface layers plus the absorption losses by the plasma and the conduction losses by the substrate. This can be expressed as

$$(1-R)[E - \text{Energy losses (plasma + conduction)}]$$
$$= \Delta t(\rho C_p \Delta T + \Delta H) \qquad (2.1)$$

where R is the reflectivity, E corresponds to the incident laser energy, and ρ, C_p, ΔT, and ΔH are, respectively, the mass density, heat capacity, temperature difference, and volume latent heat of the target material. The factor Δt corresponds to the thickness of evaporated

target material per laser pulse. The plasma absorption and heat conduction losses represent the threshold energy, E_{th}, that is needed for evaporation. From the above heat balance equation, the thickness of the evaporated layer can be expressed as

$$\Delta t = \frac{(1-R)(E-E_{th})}{\rho C_p \Delta T + \Delta H} \qquad (2.2)$$

This equation is valid when the thermal diffusion length $(2D\tau)^{1/2}$ is longer than the absorption depth of the laser beam, $1/\alpha$. This is suitable for metallic targets which have high absorption coefficients. However, if the thermal diffusion length is smaller than $1/\alpha$, then the thermal conductivity is not a major factor in the evaporation process and the evaporation depth depends simply on the attenuation distance of the laser beam. This is the case for materials for which the absorption coefficient and thermal diffusivity are small, such as insulators, non-metallic solids and polymers.

In the case of metallic targets, the absorption depths are typically of the order of 10 nm, while the thermal diffusion lengths during the laser pulse duration become this small only when femtosecond laser pulses are used.[52] When the thermal diffusion length is longer than $1/\alpha$, all the photonic energy is deposited into the absorption layer and is thermally transported only to a depth of the thermal diffusion length, $(2D\tau)^{1/2}$, during the laser pulse.

2.2.2. Plasma generation and three-dimensional isothermal expansion

The thermionic emission of positive ions and electrons from a hot target surface by nanosecond high-powered laser irradiation has been widely studied.[53-55] The emission

of electrons and of positive ions from a solid surface can be described by the Richardson and the Langmuir-Saha equations, respectively, which show an exponential increase in the fraction of ionized species with temperature. The degree of ionization of the plasma after a nanosecond laser pulse is close to unity for most materials.[52] The mechanism for such a high degree of ionization still remains contentious.

For a gas in local thermodynamic equilibrium, the ratio of singly charged ions to neutrals in the plasma is given by the Saha equation

$$\frac{n_i}{n_n} = 2.4 \times 10^{15} \frac{T^{3/2}}{n_i} e^{-U_i / k_B T}, \tag{2.3}$$

where n_i and n_n are the density of ions and neutrals in cm^{-3}, T is the gas temperature in K, and U_i is the first ionization potential in electronvolts.[56] The exponential factor keeps the fractional ionization, $n_i/(n_i+n_n)$, of the plume very small until the temperature is raised to where U_i is only few times k_BT. The fractional ionization then suddenly rises and the vapor becomes a plasma. The ablation of the target materials has been found to be accompanied by a brilliant glow extending outward from the surface of the target. Even though the temperature of the target surface is high and is close to the vaporization temperature, a higher temperature can be generated in the evaporated plasma by the interaction of the laser irradiation with it.

The absorption of the laser beam by the plasma depends on the electron-ion density, temperature, and the wavelength of the laser pulse[57-62], while the initial temperature of the material evaporated from the surface of the target depends on the absorptive characteristic of the material. The primary absorption mechanism for the

ionized plasma is due to the electron-ion collisions.[53,63] Primarily, the absorption would occur by an inverse bremsstrahlung process that involves the absorption of a photon by a free electron. The absorption coefficient α_p, of the plasma is given by Hughes[63],

$$\alpha_p = 3.69 \times 10^8 \frac{Z^3 n_i^2}{T^{1/2} \nu^3} (1 - e^{-h\nu / k_B T}), \tag{2.4}$$

where Z is average charge, n_i is ion density in cm^{-3}, T is plasma temperature, h is Planck's constant, k_B is the Boltzmann constant, and ν is the frequency of the laser light. Equation (2.4) shows that the plasma absorption coefficient is proportional to n_i^2 so that the plasma absorbs the incident laser radiation at a distance very close to the target where the density of charged species is high. In this equation, Singh assumed that the plasma frequency is smaller than the frequency of the laser wavelength, otherwise, all the radiation would be reflected by the plasma.

For the KrF excimer laser (λ=248 nm), the laser frequency is 1.21×10^{15}/s. The plasma frequency is given by[64]

$$\omega_p = 8.98 \times 10^3 n_e^{1/2} \tag{2.5}$$

where n_e is the electron density in the plasma. Using this equation, the critical electron density for reflection of the laser beam by the plasma is calculated to be $1.35 \times 10^{23}/cm^3$. The high value of critical electron density means that reflection losses by the plasma are not significant for UV-laser induced plasmas.

As the plasma absorbs the laser radiation via the inverse bremsstrahlung process, it will become hotter, more ionized and absorbs still more efficiently. Willmott et al.[52] show the evolution of the plasma using this model for the ablation of a Ti metallic target

and their result is shown in Fig. 2.3. They assumed that as the plasma propagates in the z direction normal to the target surface its cross section remains constant. The degree of ionization after the laser pulse remains under 10^{-3} for the plasma initial temperature T = 3562 K and under 10^{-2} for the initial temperature T = 5000 K. The degree of ionization, however has been found experimentally to be 0.1 - 1.0 right after the laser pulse is terminated. Such a high degree of ionization can occur from an initial temperature of about 10,000 K, but this appears unreasonable. (Usually surface temperatures of targets after laser irradiation are in the range of 2000 - 3000 K.[65]). Only a nonthermal desorption and ionization process, therefore, can induce a locally high density of electrons in the plasma starting at the vaporization temperature. Willmott stated that local nonuniformities in electron density in volumes of dimensions comparable to the mean free path of electrons ($d \sim 1$ μm), considered to be caused by laser irradiated "hot spots" multiphoton ionization, and surface impurities, can seed a runaway breakdown of the entire ablation plasma by the inverse bremsstrahlung process on the time scale of femtoseconds. Dreyfus[66] and Wiedeman et al.[67] show that the probability of this presence depends on the laser energy and flux, but may be unavoidable when one considers that d^3 is about 10^5 times smaller than the volume of the plasma. Right after the laser pulse is terminated, initial temperatures within the localized plasma can exceed 20,000 K. After laser ablation with a nanosecond pulse, the plasma thickness is still a small fraction of a millimeter. In the case of metals, the typical ablation yields 10^{15} particles per pulse, the pressures expected are up to the 7.5×10^6 torr, and such values have been reported. The initial plasma pressure generally will be highest for materials

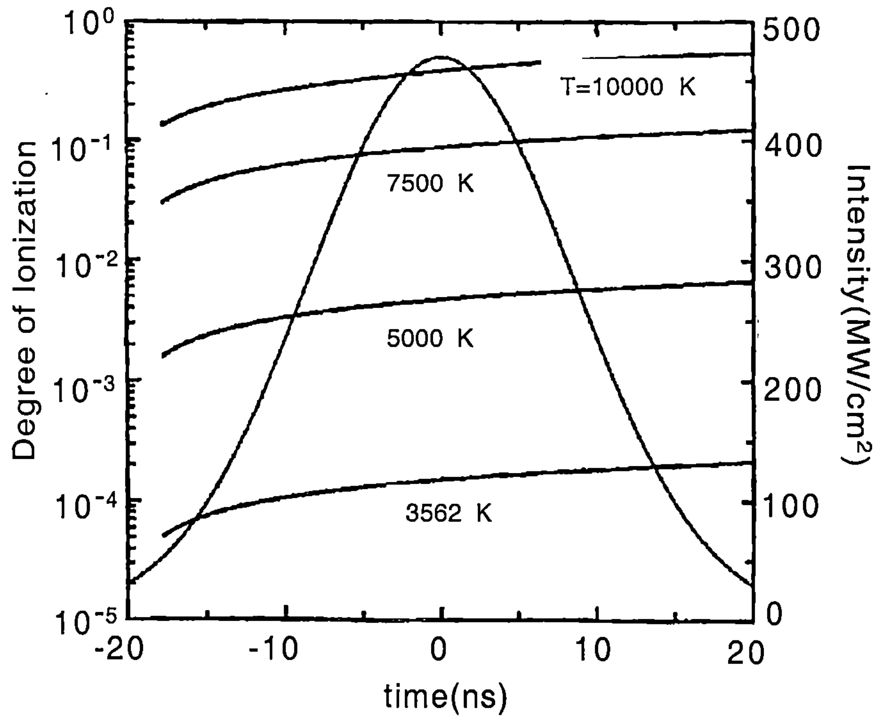

Figure 2.3. Evolution of the degree of ionization of a Ti plume by inverse bremsstrahlung during the irradiation with a 10 J/cm^2, 20-ns laser pulse duration at 248 nm for different initial plasma temperatures, calculated using the Saha equation, Eq. (2.3) (From Willmott et. al[52]).

that have a high bulk optical absorption.

In the initial stage of the plasma expansion, there are numerous collisions due to the high density of particles (the order of ~$10^{19} - 10^{20}/cm^3$). Consequently, the mean free paths of the particles are short and the plasma expansion can be modeled as a continuum fluid expansion by using the equations of gas dynamics. The pressure and density profiles in the plasma are assumed to decrease exponentially with distance from the surface of the target. As demonstrated by Geohegan,[68] the spatial distribution of the plasma has a Gaussian profile, though with quite different Gaussian widths perpendicular and parallel to the target surface. Even though a more realistic assumption of the pressure and density gradient would be an exponentially decreasing profile, Singh assumed that the pressure and density in the plasma decrease linearly from its inner edge. He found that the linear assumption is more tractable mathematically and obtained a similar result with an exponentially decreasing assumption.[45] The density of the plasma at any point (x, y, z) at time $t \leq \tau$ (the laser pulse duration), can be expressed as

$$n(x,y,z,t) = n_0(t)\frac{t}{\tau}\left(1-\frac{x}{X(t)}\right)\left(1-\frac{y}{Y(t)}\right)\left(1-\frac{z}{Z(t)}\right) \qquad t \leq \tau, \qquad (2.6)$$

where n_0 is the density at the center of the laser spot [spatial coordinates (0,0,0)] on the target at time t, and $X(t)$, $Y(t)$, and $Z(t)$ are the dimensions of the expanding plasma in the three orthogonal directions. Since Singh has assumed that the plasma behaves as an ideal gas, the pressure P at any point (x,y,z), at time t in the plasma is related to its density by the ideal gas law, and can be expressed in a similar manner by

$$P(x,y,z,t) = P_0(t)\frac{t}{\tau}\left(1-\frac{x}{X(t)}\right)\left(1-\frac{y}{Y(t)}\right)\left(1-\frac{z}{Z(t)}\right) \qquad t \leq \tau, \qquad (2.7)$$

where $P_0(t)$ is the pressure at point (0,0,0) in the plasma.

The velocity of the plasma should be proportional to distance from the target surface and can be expressed by

$$\vec{v}(x,y,z,t) = \frac{x}{X(t)}\frac{dX(t)}{dt}\hat{i} + \frac{y}{Y(t)}\frac{dY(t)}{dt}\hat{j} + \frac{z}{Z(t)}\frac{dZ(t)}{dt}\hat{k} \tag{2.8}$$

where *dX/dt, dY/dt* and *dZ/dt* are the expansion velocities of the plasma edges *X, Y* and *Z*. According to Eq. (2.8), the velocity of any point (*x*, *y*, *z*) in the plasma depends on the distance from the center of the plasma. The variation of pressure, velocity and density as a function of distance is shown schematically in Fig. 2.4. The equations of gas dynamics that govern the plasma expansion are the equation of motion and the equation of continuity. If the equation of the conservation of linear momentum is applied directly on each fluid element, the rate at which work is done by the plasma in the *x* direction is equal to the rate of kinetic energy increase in the *x* direction. By integrating over the total volume of the plasma, this can be expressed as

$$-\int_0^X \int_0^Y \int_0^Z \frac{\partial P}{\partial x}\frac{\partial x}{\partial t} dxdydz = \frac{1}{2}\frac{d}{dt}\int_0^X \int_0^Y \int_0^Z mn(x,y,z,t)\left(\frac{dx}{dt}\right)^2 dxdydz \tag{2.9}$$

where *m* is the atomic mass of the species in the plasma.

The plasma behaves as an ideal gas and obeys the ideal gas equation

$$P(x,y,z,t) = n(x,y,z,t)k_B T_0 \tag{2.10}$$

where k_B is the Boltzmann constant and T_0 is the isothermal temperature of the plasma. From the Eqs. (2.6), (2.8) and (2.10) we obtain

$$\frac{\partial P}{\partial x} = n_0(t)\left(-\frac{t}{\tau}\right)\frac{1}{X}k_B T_0, \qquad \text{and} \tag{2.11}$$

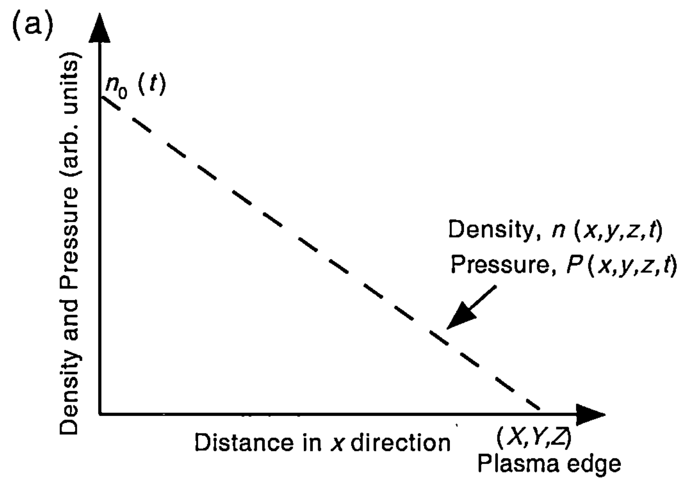

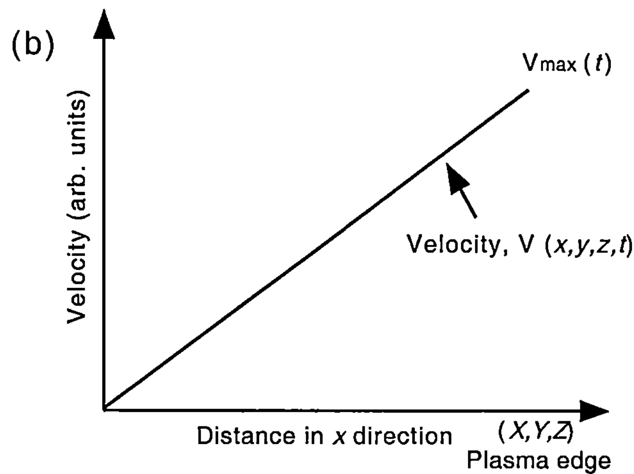

Figure 2.4. Schematic diagram showing the density (n), pressure (P) and velocity (v) gradients employed in Singh's model. The density and pressure are linearly decreasing from the target surface while the velocity is linearly increasing.

$$\frac{\partial x}{\partial t} = \frac{x}{X}\frac{dX}{dt} \tag{2.12}$$

Putting Eqs. (2.11) and (2.12) into the left side of Eq. (2.9), then by integrating, we get the following expression:

$$-\int_0^X n_0(t)k_B T_0\left(-\frac{t}{\tau}\right)\frac{1}{X^2}\frac{dX}{dt}xdx = n_0(t)k_B T_0\left(\frac{t}{\tau}\right)\frac{1}{2}\frac{dX}{dt} \tag{2.13}$$

The right side of Eq. (2.9) becomes

$$\frac{M}{2}\frac{d}{dt}\int_0^X n_0(t)\frac{t}{\tau}\left(1-\frac{x}{X}\right)\frac{x^2}{X^2}\left(\frac{dX}{dt}\right)^2 dx$$

$$= \frac{M}{2}\frac{d}{dt}\left[\frac{1}{X^2}\left(\frac{dX}{dt}\right)^2 n_0(t)\frac{t}{\tau}\int_0^X\left(x^2-\frac{x^3}{X}\right)dx\right] \tag{2.14}$$

$$= \frac{M}{24}\frac{d}{dt}\left[\left(\frac{dX}{dt}\right)^2 Xn_0(t)\frac{t}{\tau}\right] \tag{2.15}$$

$$\left[\text{Equation } \int_0^X\left(x^2-\frac{x^3}{X}\right)dx = \frac{1}{12}X^3 \text{ was used}\right]$$

$$= \frac{M}{24}\left[2\left(\frac{dX}{dt}\right)\left(\frac{d^2X}{dt^2}\right)Xn_0(t)\frac{t}{\tau} + \left(\frac{dX}{dt}\right)^3 n_0(t)\frac{t}{\tau} + \left(\frac{dX}{dt}\right)^2 X\frac{dn_0(t)}{dt}\frac{t}{\tau} + \left(\frac{dX}{dt}\right)^2 Xn_0(t)\frac{1}{\tau}\right] \tag{2.16}$$

By ignoring the second and third term and comparing with Eq. (2.13), we obtain the following differential equation,

$$X(t)\left(\frac{d^2X}{dt^2} + \frac{1}{2t}\frac{dX}{dt}\right) = \frac{6k_B T_0}{M}, \tag{2.17}$$

For the other two directions, x and y, of expansion, similar equations can be obtained. Therefore, the final differential equation governing the plasma expansion in the isothermal region is expressed as

$$X(t)\left(\frac{d^2X}{dt^2}+\frac{1}{2t}\frac{dX}{dt}\right)=Y(t)\left(\frac{d^2Y}{dt^2}+\frac{1}{2t}\frac{dY}{dt}\right)=Z(t)\left(\frac{d^2Z}{dt^2}+\frac{1}{2t}\frac{dZ}{dt}\right)=\frac{6k_BT_0}{M}, \qquad (2.18)$$

This equation initially determines the plasma expansion during the time interval of the laser pulse. As the velocities are controlled by the pressure gradient, the expansion is highly anisotropic in the perpendicular direction to the target. Eq. (2.18) also shows that the acceleration is inversely proportional to initial plasma dimensions when the expansion velocities are low. The initial dimensions of the plasma in the transverse direction are of the order of mm (the laser spot size is typically 2-3 mm), whereas the plasma expands only tens of μm in the perpendicular direction, normal to the target. Once the plasma expansion velocities increase, the acceleration starts to diminish and ultimately becomes zero. Consequently, Eq. (2.18) results in the characteristic elongated PLD plume shape (forward directed) shown in Fig. 2.1.

2.2.3. Adiabatic plasma expansion and recondensation

In this part, the adiabatic expansion of the plasma after the termination of the laser pulse will be examined. Fluid dynamic models have been applied successfully to the expanding plasma by Sibold et. al.,[69] and Kelly et. al.[70] After the termination of the laser pulse, there is no injection of evaporated particles from the target into the plasma. Thus, the continued expansion of the plasma occurs, with its density described by a Gaussian profile, where the temperature can be related to the dimensions of the plasma through the adiabatic thermodynamic equation of state which is given by

$$T[X(t)Y(t)Z(t)]^{\gamma-1} = \text{constant} = \beta \qquad (2.19)$$

where $\gamma = C_p/C_v$, the ratio of the specific heat capacities at constant pressure and volume. The plasma's thermal energy is rapidly converted into kinetic energy during adiabatic expansion, obtaining extremely high expansion velocities. In vacuum, the maximum attainable velocity for any expanding gas is given by[71]

$$v_{max} = 2v_s / \gamma - 1 \tag{2.20}$$

where v_s is velocity of the sound in the medium,

$$v_s = \sqrt{\gamma RT / M} \tag{2.21}$$

In the case of monoatomic gases the value of γ is 1.67, whereas γ is in the lower range of 1.2-1.3 for laser induced-ionized species.[32]

During the adiabatic expansion, the velocity of the plasma increases due to the decrease of the thermal energy of the plasma. Since there is no particle injection into the plasma, its density and pressure can be expressed by neglecting the term (t/τ) in Eqs. (2.6) and (2.7):

$$n(x,y,z,t) = n_0(t)\left(1-\frac{x}{X(t)}\right)\left(1-\frac{y}{Y(t)}\right)\left(1-\frac{z}{Z(t)}\right), \quad t > \tau \tag{2.22}$$

$$P(x,y,z,t) = P_0(t)\left(1-\frac{x}{X(t)}\right)\left(1-\frac{y}{Y(t)}\right)\left(1-\frac{z}{Z(t)}\right), \quad t > \tau \tag{2.23}$$

The velocity expression is the same as in the isothermal regime that is shown in Eq. (2.8). By applying the adiabatic equation of state and Newton's second law of motion, we can get the expression for the plasma expansion in the adiabatic expansion regime.

With the ideal gas law, $P(x,y,z,t) = n(x,y,z,t)k_B T(t)$, and Eqs. (2.22) and (2.23), solving for the x direction yields,

$$\frac{\partial P}{\partial x} = -n_0(t)\frac{1}{X}k_B T(t), \tag{2.24}$$

Solving for the left side of Eq. (2.9) by substituting Eqs. (2.12) and (2.24), we obtain

$$\int_0^X n_0(t) k_B T(t) \frac{1}{X^2}\frac{dX}{dt} x dx = n_0(t) k_B T(t) \frac{1}{2}\frac{dX}{dt} \tag{2.25}$$

Solving for the right side of equation (2.9), we obtain

$$\frac{M}{2}\frac{d}{dt}\int_0^X n_0(t)\left(1-\frac{x}{X}\right)\frac{x^2}{X^2}\left(\frac{dX}{dt}\right)^2 dx$$

$$= \frac{M}{2}\frac{d}{dt}\left[\frac{1}{X^2}\left(\frac{dX}{dt}\right)^2 n_0(t)\int_0^X \left(x^2 - \frac{x^3}{X}\right)dx\right] \tag{2.26}$$

$$= \frac{M}{24}\frac{d}{dt}\left[\left(\frac{dX}{dt}\right)^2 X n_0(t)\right] \tag{2.27}$$

$$= \frac{M}{24}\left[2\left(\frac{dX}{dt}\right)\left(\frac{d^2X}{dt^2}\right)X n_0(t) + \left(\frac{dX}{dt}\right)^3 n_0(t) + \left(\frac{dX}{dt}\right)^2 X \frac{dn_0(t)}{dt}\right] \tag{2.28}$$

By ignoring the second and third terms and comparing with Eq. (2.25), we obtain the following expression,

$$X(t)\frac{d^2X}{dt^2} = \frac{6k_B T(t)}{M} \tag{2.29}$$

Substituting the adiabatic equation, Eq. (2.19) into Eq. (2.29),

$$X(t)\frac{d^2X}{dt^2} = \frac{6k_B}{M}\frac{\beta}{[X(t)Y(t)Z(t)]^{\gamma-1}} \tag{2.30}$$

$$= \frac{6k_B T_0}{M}\left(\frac{X_0 Y_0 Z_0}{X(t)Y(t)Z(t)}\right)^{\gamma-1} \tag{2.31}$$

Also, similar equations for the other two directions of expansion can be obtained. So, the final equation for the plasma expansion in the adiabatic regime is expressed as

$$X(t)\frac{d^2X}{dt^2} = Y(t)\frac{d^2Y}{dt^2} = Z(t)\frac{d^2Z}{dt^2} = \frac{6k_BT_0}{M}\left(\frac{X_0Y_0Z_0}{X(t)Y(t)Z(t)}\right)^{\gamma-1} \quad (2.32)$$

where X_0, Y_0, and Z_0 are the initial orthogonal edges of the plasma after the termination of the laser pulse ($t = \tau$). Eq. (2.32) shows that the acceleration of the plasma varies inversely with its dimensions and also depends on the mass of the species and their initial temperature.

In the previous section, it was stated that the initial dimensions of the plasma are much larger in the transverse directions than in the perpendicular direction. Since the velocities are governed by those dimensions, then the highest velocities are in the direction of the smallest dimension, i.e. the plasma is strongly forward-peaked which is the characteristic elongated plasma shape. Due to the laser-solid interaction, the plasma expansion always occurs in the perpendicular direction to the target surface regardless of the incident angle of the laser beam. When the plasma expands adiabatically it cools down to temperatures typical in the range of 3000-5000 K, as shown by Geohegan.[72] The kinetic energies of the plasma species can be in the range of 1-500 eV depending on the materials, but normally 5-50 eV. Weaver[73] shows that the angular distribution of the plume has been fitted to a $\cos^n\theta$ function, with n ranging from 2 to more than 20. Generally, n depends on the laser fluence and is lower when the plasma propagates into an ambient gas that is dense enough for multiple collisions, which will broaden the angular distribution.[50] In the following chapter, a modified PLD technique, the orthogonally crossed-beam PLD method which was used for this research, will be discussed and compared with the conventional PLD technique.

Chapter 3

REACTIVE CROSSED-BEAM PULSED LASER DEPOSITION AND DEPOSITION SYSTEM CONSTRUCTION

3.1. General Background

Since the kinetic energies of ablated particles from the target material in PLD lie between 10 and several hundred eV(depending on the masses of the ablated species), typically two orders of magnitude higher than those in thermal deposition (< 1 eV), research has been carried out on the use of kinetic energy to enhance surface mobility and surface chemistry and to study their effect on film deposition. Brice et al.[74] have exploited a molecular dynamic model for ion-induced surface and bulk displacements. In their model, they show that the displacement of atoms in the first monolayer from the surface is possible if homonuclear species impinge with kinetic energies that are half the bulk displacement energy, whereas the energy required to displace atoms in the second and deeper layers exceeded the bulk displacement energy.[52] This model predicted that when incident kinetic energies range between 10 and 40 eV, enhanced surface mobility can be achieved without any damage to the bulk Si, for example. Robinzohn et. al.[75] also studied the relationship between the energy of an ion and the displacement of the host atoms and suggested that the use of a low ion energy of around 100 eV produced damage within a tolerable level. With this model, Comfort et al.,[76] and Burger et al.[77] have experimentally shown that high quality epitaxial Si films can be grown using Si ions

possessing such energies. As a consequence of this research, there seems to be a narrow window of kinetic energies that might be employed to enhance the surface mobility of ablated adatoms while maintaining high quality film growth. In this study, kinetic energies in the range of 45 ~ 155 eV were used.

The laser-induced plasma can be modified and its energy redistributed by colliding it with an ambient gas. Wood et al,[78] Powers et al,[79] and Verardi et al.[33] have studied this process and have developed models to explain the plume behavior. Wood et al developed a model to describe the expansion of a laser-generated plume into low-pressure Ar and He gases during ablation of Si to form Si nanoclusters. Powers et al.[79] showed that multiple collisions among the ablated particles result in the production of clusters, which then emerge in a supersonic jet. In this process, the plume is rapidly thermalized by multiple collision processes with an ambient gas until the ablated particles move slowly enough to nucleate and form clusters. Under sufficiently rarified conditions, however, and using a high-purity elemental target, reactive pulsed laser deposition proceeds without the formation of clusters and instead, films result having smooth surface morphologies and high crystalline quality.

As an adaptation of this form of reactive PLD, Gupta et al.[34] used a pulsed source of O_2 gas instead of a continuous flow to compensate oxygen deficiency normally observed during $YBa_2Cu_3O_{7-\delta}$ thin film growth. A pulsed molecular beam valve and laser-pulse trigger were synchronized so that the supersonic gas jet and the ablated fragments arrived at the substrate at the same time. This process provided necessary oxygen to form the YBCO phase while maintaining a low background pressure, which

enables the use of *in-situ* surface analysis techniques such as reflection high energy electron diffraction (RHEED).

Willmott et al.[35] have refined Gupta's approach and have introduced a reactive crossed-beam PLD method to grow CuO on a MgO(100) substrate by ablating Cu metal and crossing the plume with a N_2O gas pulse. They show that if the delay between the laser-pulse trigger and the gas-pulse trigger was set within ± 100 μs of the optimal value, for which the densest portions of both the gas pulse and the plasma crossed, single phase CuO films were produced, whereas all other delays resulted in mostly Cu films with some Cu_2O phase.

There are two essential differences among the experimental setups used by Gupta et al.,[34] Willmott et al.,[35] and that used in this research. One difference is the distance between the laser spot on the target and the nozzle of the pulsed valve. The other difference is that the plume and the pulsed-gas jet cross with different angles. In Gupta's case, both the pulsed gas and the ablated plume were incident on the substrate at 45° and formed a right angle. The distance between the substrate and the pulsed valve nozzle was fixed at 9 cm. In Willmott's case, the distance between the laser spot and the nozzle of the pulsed valve was approximately 10 mm and they crossed each other at 45°. Fig. 3.1 shows the principal setup of the technique used in the present case. As can be observed in the figure, the ablated plume and the pulsed-gas jet cross orthogonally and the distance between the laser spot and pulsed-valve nozzle was ~1.3 cm. For our apparatus, the optimum delay was found to be 315 μs for a corresponding pulsed-valve driver gate width of 140 μs.

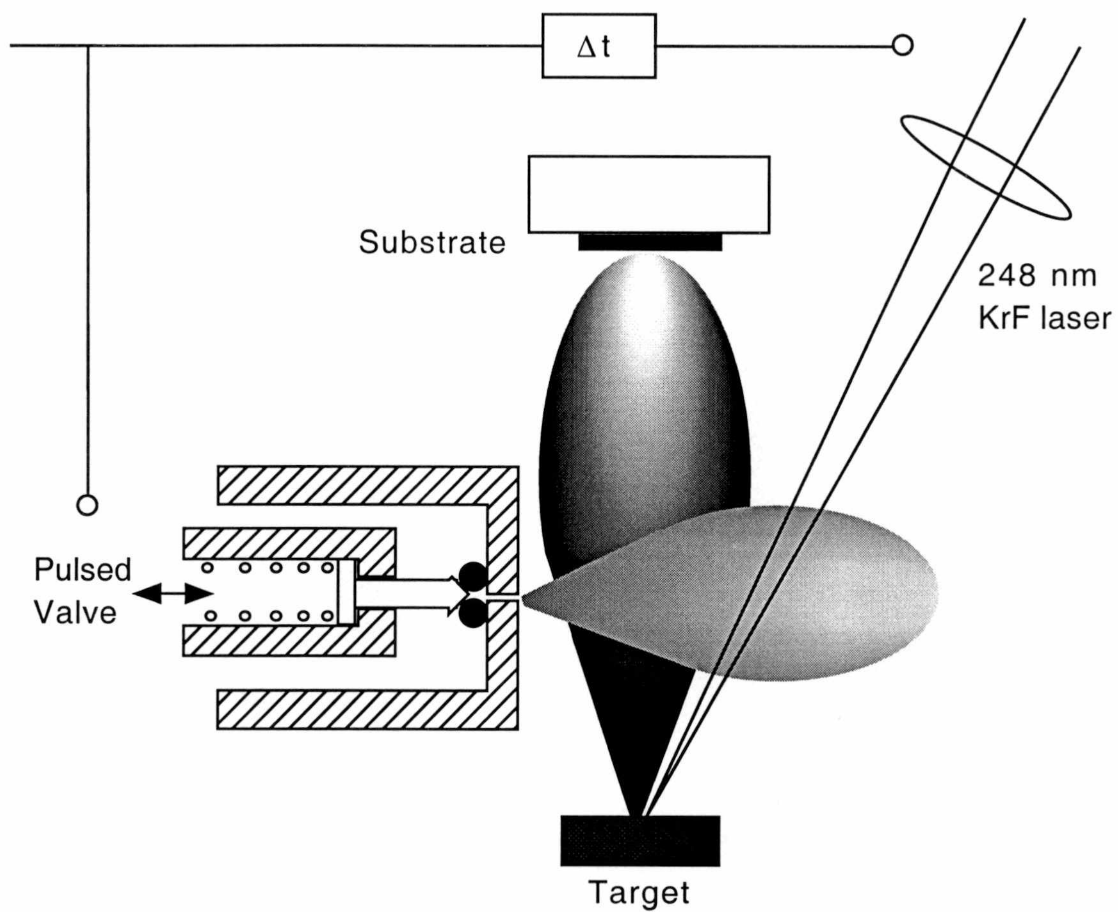

Figure 3.1. Principal setup of orthogonally crossed-beam pulsed-laser deposition.

Independent measurements in a separate chamber using a fast-ionization-gauge placed the delay associated with the gas valve and driver at ~320 μs while that associated with the gas-pulse transit time was ~17 μs/cm. Further measurements on the laser firing system revealed an instrument delay of ~2 μs while that associated with the plume transit time was ~0.6 μs/cm.

Strong interactions occur locally where the expanding gas pulse crosses the ablation plume and these results in an enhanced degree of ionization. For example, Willmott noted that the degree of ionization of the plasma when it crossed with pulsed gas, compared to that for expansion into vacuum increases from less than 10^{-3} to 0.28 ± 0.11.[80] Scattering processes between the laser-induced plasma and the pulsed-gas expansion are responsible for the improved reactivity in crossed-beam reactive pulsed-laser deposition. In the following, the scattering processes in the interaction region between the pulsed gas and the ablation plasma are presented.

3.2. Reactive Scattering Process

An understanding of the dynamics of the physical and chemical interactions of the ablated plasma species with the ambient gas is essential for optimal control of the growth parameters, because these interactions play an important role in the kinetic energy distribution and the chemistry of the ablated plume and scattered species. Fig. 3.2 illustrates the change in the expanding ablation plume when crossed with an expanding gas pulse. In vacuum, or when the plume and gas-pulse are not synchronized, the plume was observed to be relatively small and elongated in the direction of propagation. As the

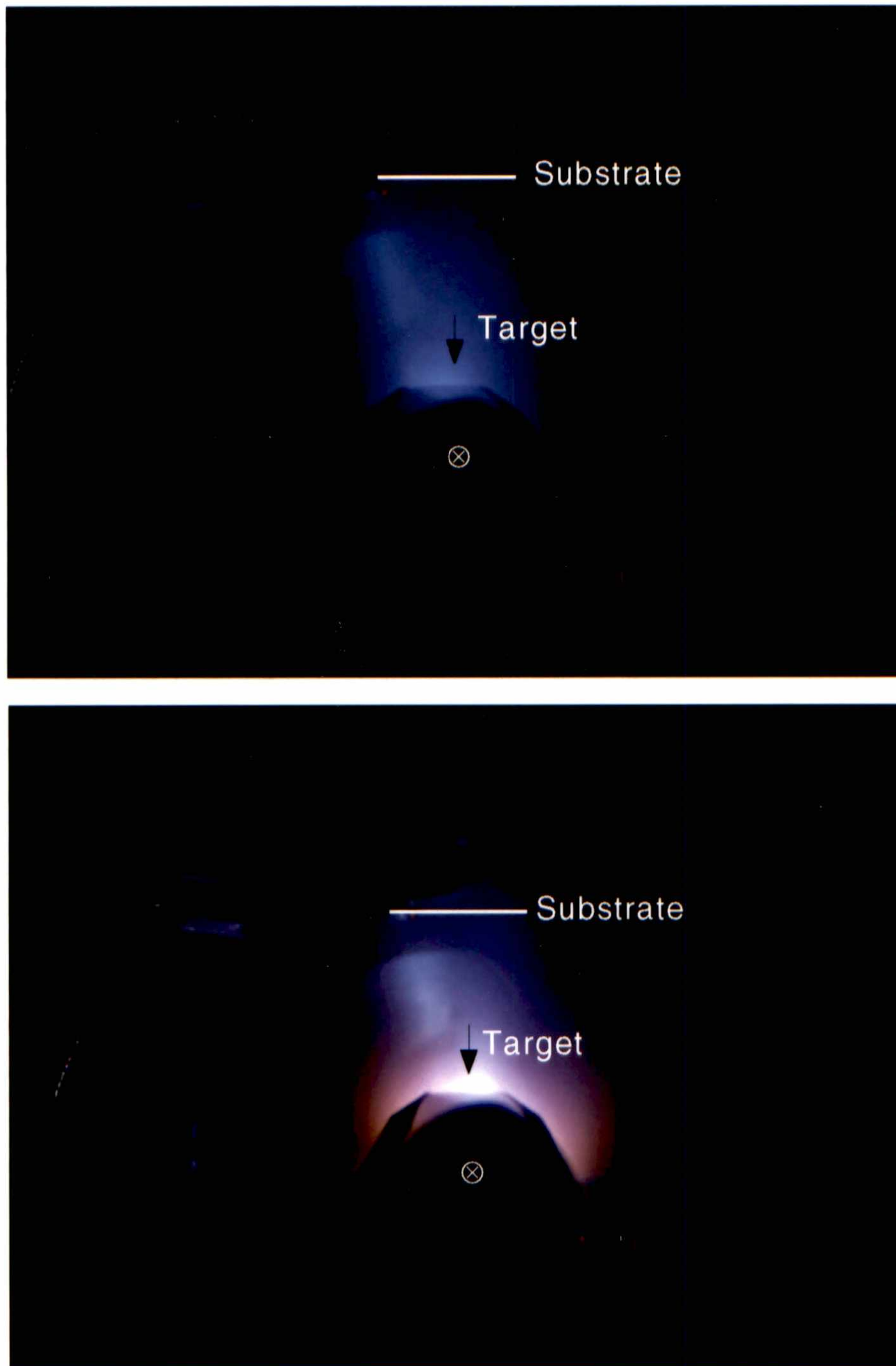

Figure 3.2. Change in visual image of a YSZ ablation plume propagating into a vacuum (above) and crossed with O_2 gas pulse (below, ⊗: O_2 gas-pulse direction).

laser delay was optimized, the brightness of the plume increased, its color changed, and it tended to take on a more rounded appearance.

To identify the ablated species in the plume and their kinetic energies, Willmott[80] employed time-of-flight quadrupole mass spectroscopy (TOFQMS). They showed that the ablation plume contains not only stable neutrals and possibly clusters, but also metastable species such as Rydberg atoms, ionic species and electrons.

In this research, however, only ion probe-based time-of-flight (TOF) measurements could be made and these were employed to identify the average kinetic energy of the plume. Fig. 3.3 illustrates the change in the ion probe signal while ablating Ti in vacuum at different laser energy densities on the target. As can be deduced from the figure, as more laser energy is coupled into the target, the average plume velocity increases and hence the species have more kinetic energy. The intensity of the signal also increases, which indicates that more material is being transported. Fig. 3.4 illustrates the effect of crossing the fastest moving plume (vacuum TOF ~2 μs) with a synchronized gas pulse. As shown in the figure, as the delay is increased from 180 μs to 430 μs, the ion probe signal broadens greatly and moves to larger times. This is a direct consequence of the increased interaction with the gas pulse, which leads to collisional slowing and increased scattering. As the delay is increased further, from 430 μs to 680 μs, the ion probe signal sharpens and moves to smaller times, which indicates reduced interaction with the gas pulse.

Collision processes can be divided into elastic and inelastic collisions according to whether the internal energies of the colliding bodies are maintained or not. Usually

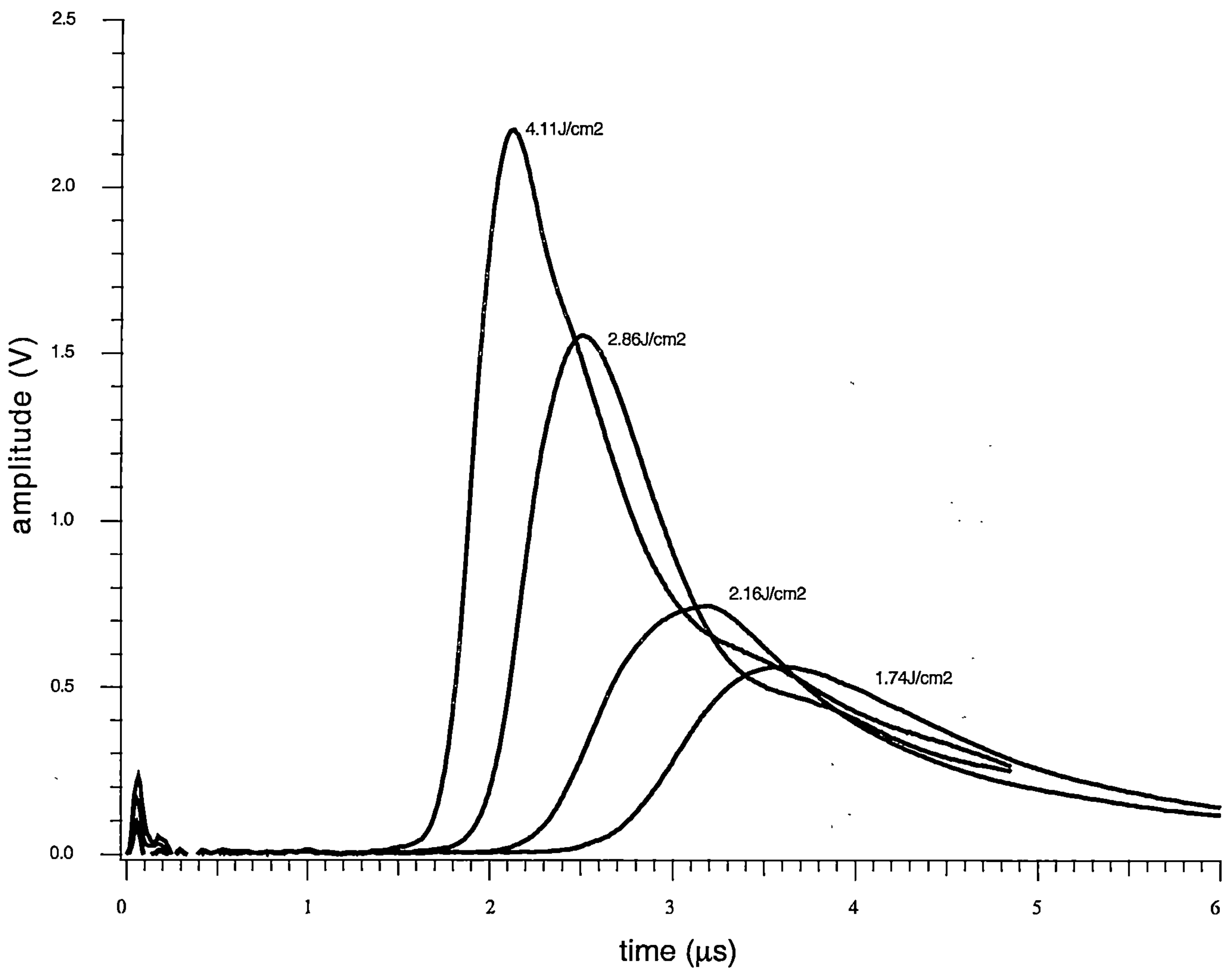

Figure 3.3. Different time-of-flight signals in vacuum as a function of laser energy density on the Ti target.

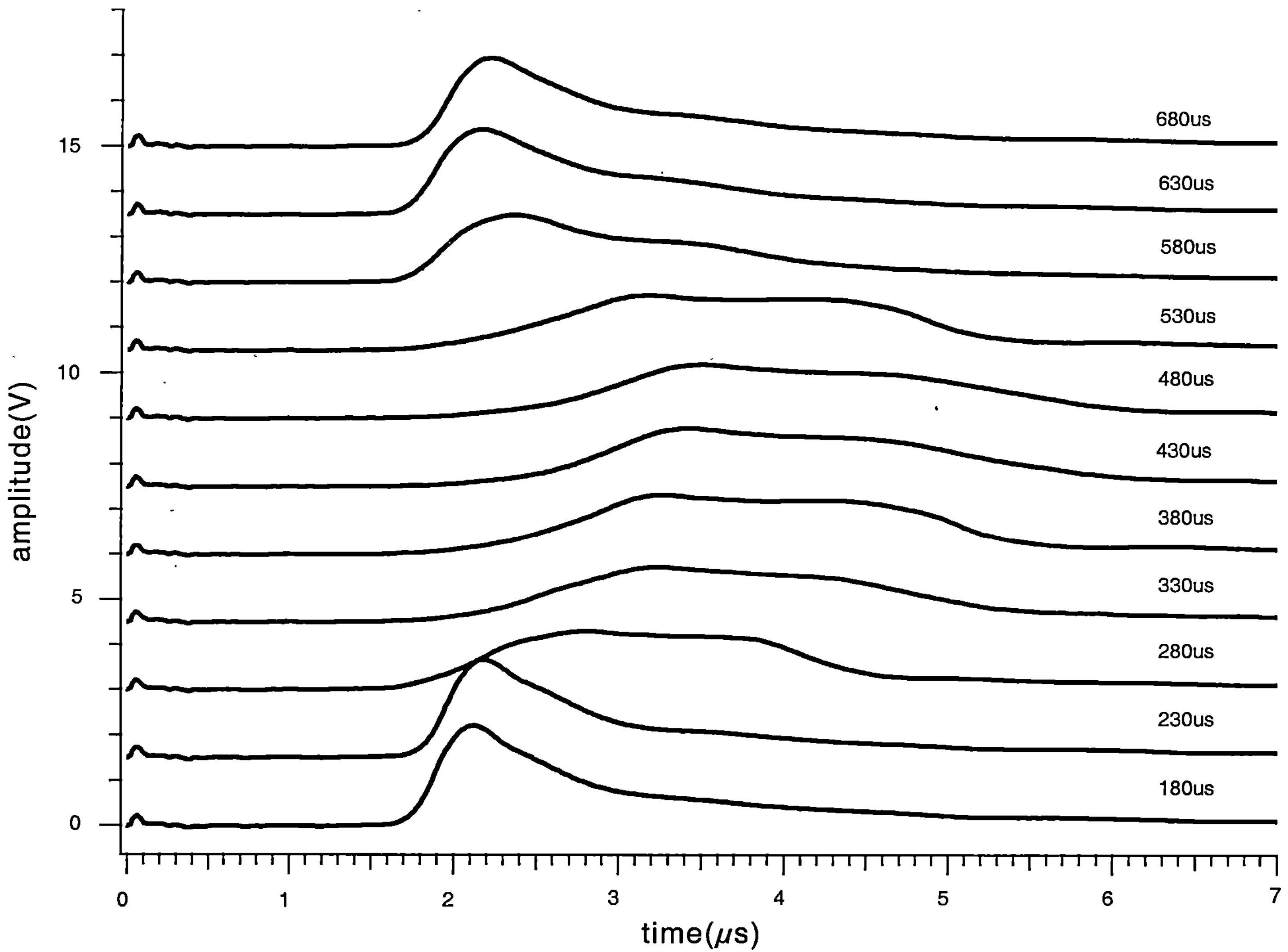

Figure 3.4. TOF signals with different laser delays at fixed 2.0 μs vacuum TOF while the gas pulse and the laser plume are crossing

particles have two kinds of energy, kinetic energy and potential or internal energy. The kinetic energy is equal to $\frac{1}{2}mv^2$ for translational motion, while the potential or internal energy may be in the form of electronic excitation and ionization. An elastic collision is one that involves the exchange of kinetic energy only, whereas an inelastic collision changes not only kinetic energy but also internal energies.

(1) Energy transfer in elastic collisions

Let's consider the collision between two particles of masses m_i and m_j. Since the plasma species are more than an order of magnitude faster than gas molecules from the pulsed valve, let's suppose that gas molecule m_j is initially stationary and that plasma species m_i collides with velocity v_i and is deflected at an angle θ after the collision (Fig. 3.5). According to the conservation of linear momentum

$$m_i \mathbf{v}_i = m_i \mathbf{v}'_i + m_j \mathbf{v}'_j \quad (3.1)$$

and by the conservation of energy

$$\frac{1}{2} m_i v_i^2 = \frac{1}{2} m_i v_i'^2 + \frac{1}{2} m_j v_j'^2 \quad (3.2)$$

From Eq. (3.1) we obtain

$$\begin{aligned} (m_i v'_i)^2 &= (m_i v_i)^2 + (m_j v'_j)^2 - 2 m_i m_j \mathbf{v}_i \cdot \mathbf{v}'_j \\ &= (m_i v_i)^2 + (m_j v'_j)^2 - 2 m_i m_j v_i v'_j \cos\theta \end{aligned} \quad (3.3)$$

where θ is an angle between incident particle m_i and deflected particle m_j after the collision.

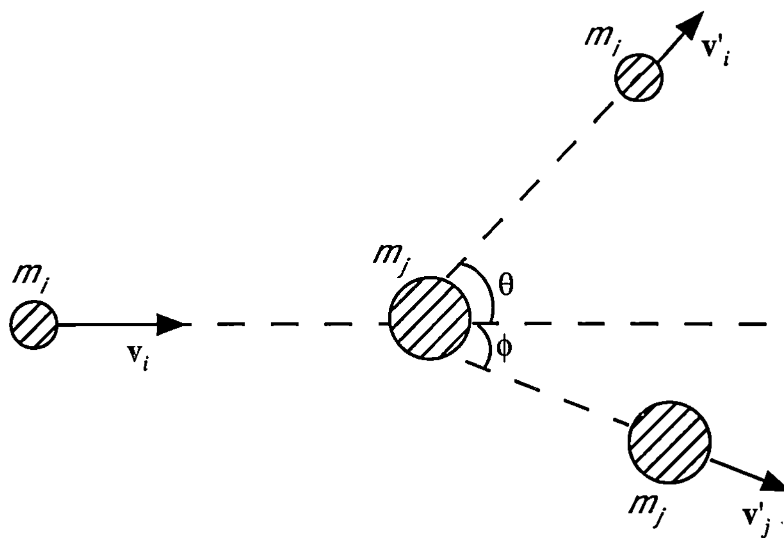

Figure 3.5. Velocity components before and after an elastic collision.

From Eqs. (3.2) and (3.3), v'_j can be expressed as

$$v'_j = \frac{2m_i v_i}{m_i + m_j} \cos\theta \tag{3.4}$$

The fractional energy transferred from mass m_i to mass m_j is given by

$$\frac{E'_j}{E_i} = \frac{\frac{1}{2} m_j v_j'^2}{\frac{1}{2} m_i v_i^2} = \frac{m_j}{m_i v_i^2} \left(\frac{2m_i v_i}{m_i + m_j} \cos\theta \right)^2 \tag{3.5}$$

$$= \frac{4m_i m_j}{\left(m_i + m_j\right)^2} \cos^2\theta \tag{3.6}$$

The term $4m_i m_j/(m_i+m_j)^2$ is known as the energy transfer function and has the value 1 when $m_i = m_j$.

(2) Inelastic collisions

When the collision is inelastic, the particle gains internal energy of ΔU. By the momentum conservation

$$m_i \mathbf{v}_i = m_i \mathbf{v}_i' + m_j \mathbf{v}_j' \tag{3.7}$$

and by the conservation of energy

$$\frac{1}{2} m_i v_i^2 = \frac{1}{2} m_i v_i'^2 + \frac{1}{2} m_j v_j'^2 + \Delta U \tag{3.8}$$

From Eq. (3.7) we obtain

$$\begin{aligned}(m_i v_i')^2 &= (m_i v_i)^2 + (m_j v_j')^2 - 2 m_i m_j \mathbf{v}_i \cdot \mathbf{v}_j' \\ &= (m_i v_i)^2 + (m_j v_j')^2 - 2 m_i m_j v_i v_j' \cos\theta \end{aligned} \tag{3.9}$$

where θ is an angle between incident particle m_i and deflected particle m_j after the collision.

Eq. (3.8) can be simplified using Eq. (3.9) as

$$\Delta U = m_j v_j' v_i \cos\theta - \frac{1}{2} \frac{m_j}{m_i} \left(m_i + m_j \right) v_j'^2 \tag{3.10}$$

This can be differentiated to maximize ΔU by writing

$$\frac{d}{dv_j'} (\Delta U) = m_j v_i \cos\theta - \frac{m_j}{m_i} (m_i + m_j) v_j' = 0 \tag{3.11}$$

$$\text{i.e. } \; v_i \cos\theta = \frac{(m_i + m_j)}{m_i} v_j' \tag{3.12}$$

Substituting Eq. (3.12) into Eq. (3.10), we have

$$\Delta U = \frac{1}{2}\left(\frac{m_i m_j}{m_i + m_j}\right) v_i^2 \cos^2\theta \tag{3.13}$$

Therefore, the fraction of the kinetic energy of the first particle that can be transferred to the internal energy of the second particle, has maximum value of

$$\frac{\Delta U}{\frac{1}{2} m_i v_i^2} = \frac{m_j}{m_i + m_j}\cos^2\theta \tag{3.14}$$

From Eq. (3.10), the fractional kinetic energy transfer is given by

$$\frac{E_j'}{E_i} = \frac{\frac{1}{2} m_j v_j'^2}{\frac{1}{2} m_i v_i^2} = \frac{m_j v_j'^2}{m_i}\left(\frac{2 m_j v_j'}{\frac{m_j}{m_i}(m_i + m_j) v_j'^2 + 2\Delta U}\right)^2 \tag{3.15}$$

This function has a maximum value when $\Delta U = 0$ (excluding the case when ΔU can be negative); then the fractional energy transfer has a value of $4m_i m_j/(m_i+m_j)^2$ as expected.

For most metals, the first ionization potential values are between 6 and 8 eV (Ti is 6.8 eV), which are well below the typical kinetic energies of the ablated species (~30 eV).[52] Therefore, even ground-state metal atoms from the ablation plasma can be easily ionized by collision with a pulsed-gas particle.

The reactive scattering processes between the pulsed gas jet and the ablation plasma allow some of the internal energy of the plume not only to be redistributed within the plasma itself but also to be coupled to pulsed gas species to form activated species.[52] Given the pulsed nature of the mixing event, the average background pressure in the chamber remains low and allows the activated species to travel under nearly collisionless

conditions to the substrate where they maintain most of their chemical reactivity and kinetic energy as they impinge on the surface of the growing film.

Crossed-beam reactive PLD is a high quality film growth technique for certain materials, especially binary compounds for which one of elemental components is provided by ablation of a high purity elemental target and the other component is supplied in the form of a high purity pulsed-gas jet. With this method, simple nitrides, oxides, Ga and N co-doped ZnO for p-type doping, and carbides can be fabricated. Table .3.1 shows a list of target materials and gases used in this technique and films grown by this method.

3.3. Preparation of a Reactive Crossed-Beam PLD Growth System

The system employed in the present work was custom-design by Dr. Douglas H. Lowndes and fabricated by Nor-Cal Inc. A detailed description of the system is shown in Fig. 3.6. The vacuum parts and pumping system were conventional and assembled on-site. The target carousel, substrate holder and heater, and pulsed-valve system were not commercially available so were custom-designed and fabricated on-site. To determine substrate quality and subsequent film quality, a Reflection High Energy Electron Diffraction (RHEED) system was incorporated. Vacuum integrity and purity were monitored with a residual gas analyzer. Fig. 3.7 shows a schematic diagram of the system.

Table 3.1. Targets used and films grown by crossed-beam reactive pulsed laser deposition. (Our case[a)], and Willmott et al.[b)])

Ablation Target	Gas	Substrate	film
Zn[a)]	O_2	Si(111), Al_2O_3(0001)	ZnO
Ga[a)]	NH_3	Si(111), Al_2O_3(0001)	GaN
Zn:Ga[a)]	N_2O	Si(111), Al_2O_3(0001)	ZnO
Ti[a)]	N_2	Si(111)	TiN
Cu[b)]	N_2O	MgO(001)	CuO
Ga-Al[b)]	N_2	Si(001)	$Al_xGa_{1-x}N$
Zr[b)]	N_2/CH_4	Si(001)	ZrC_xN_y
C[b)]	N_2/NH_3	Si(001)	a-CN_x
Si[b)]	N_2, CH_4	Si(001)	a-SiN_x, SiC

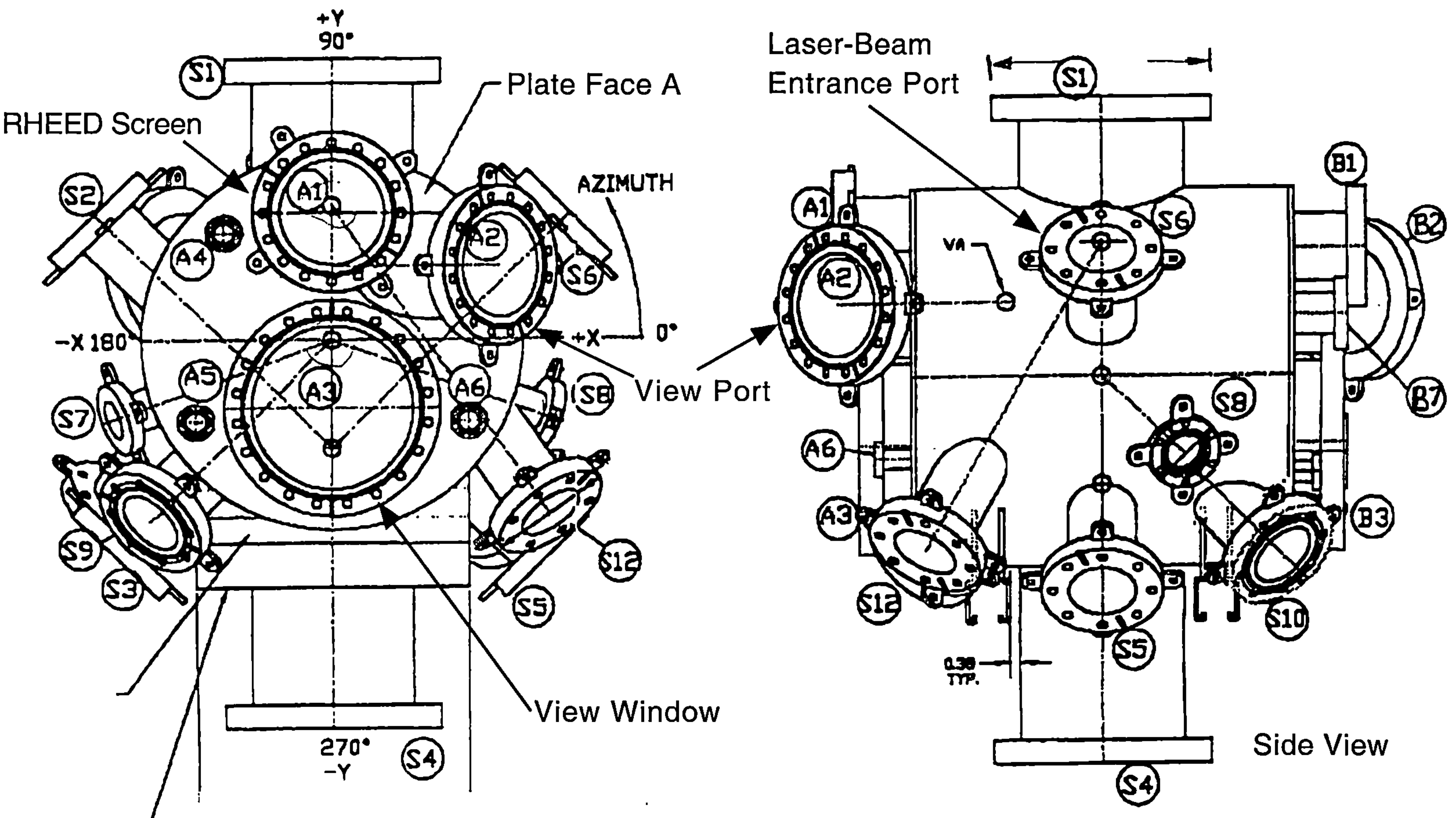

Figure 3.6. Face A and side view of PLD chamber.

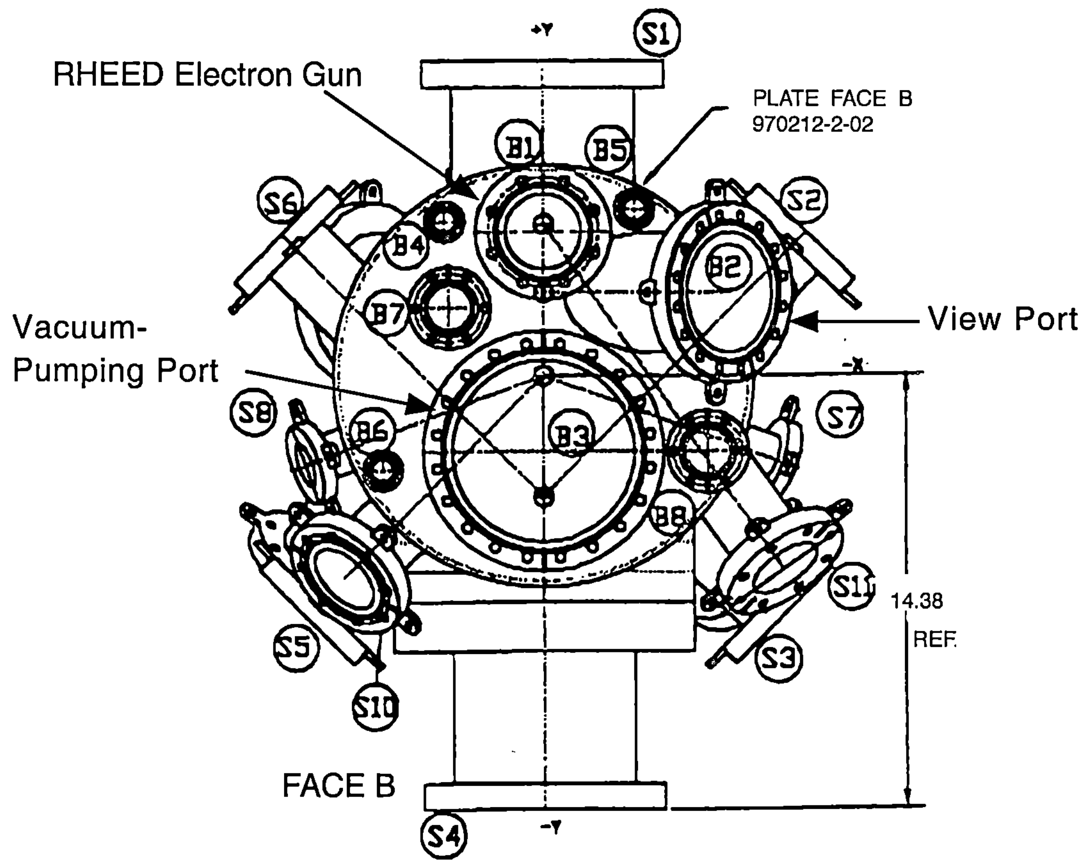

Figure 3.6. (continued) Face B of PLD chamber.

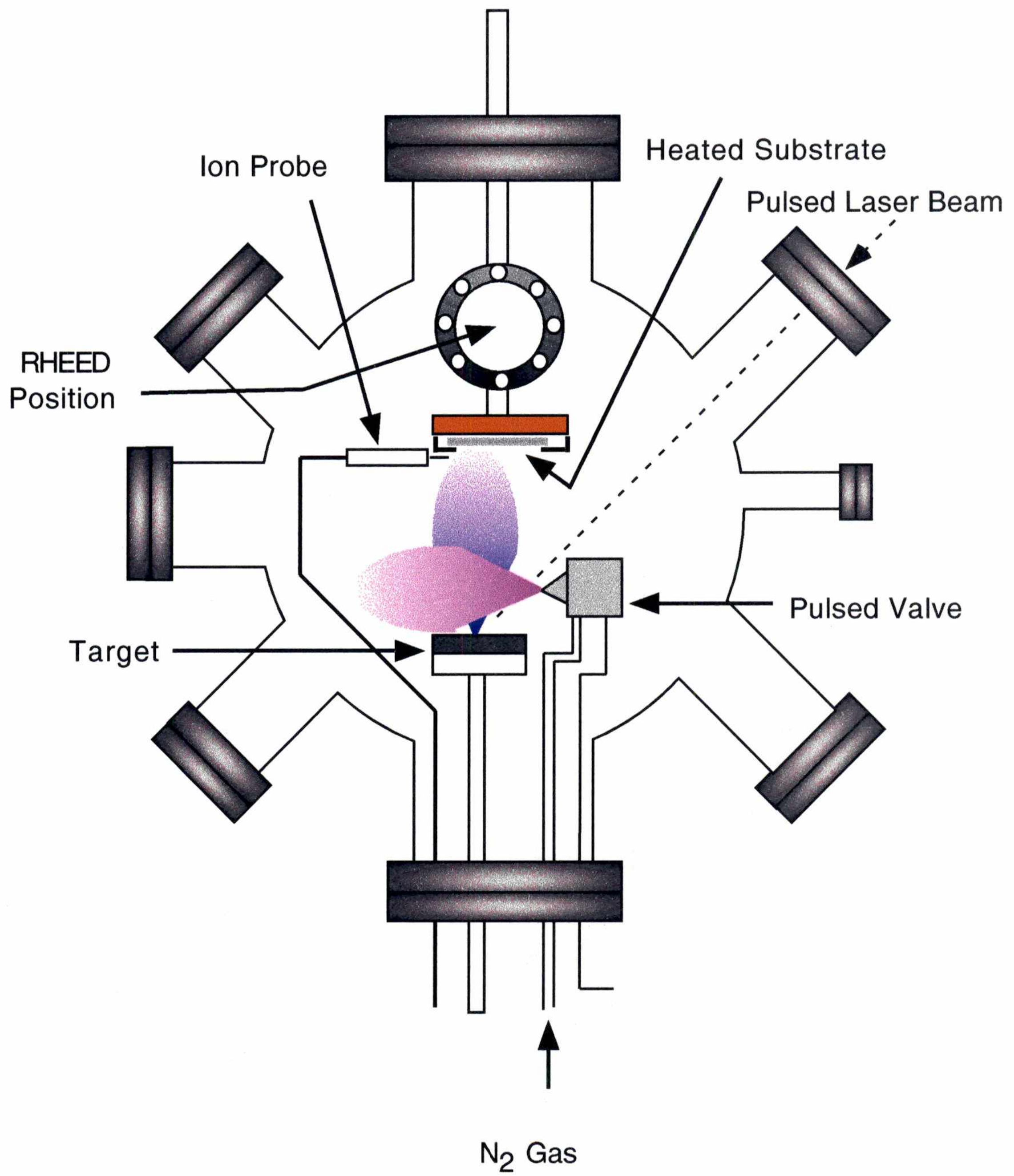

Figure 3.7. Schemaic diagram of the reactive crossed-beam PLD system.

3.3.1. Target carousel

The target carousel consisted of three target holders for solid materials and one target holder for liquid materials. The liquid target holder was for the growth of GaN thin films using a liquid Ga target. The reason for multiple targets is to provide a means of depositing multilayer structures *in-situ*. Actually, this is one of main advantages of PLD over other thin-film growth techniques. The solid targets were 1-inch diameter disk-shape pellets, 0.25 inch thick. The targets were placed in a target holder that was designed to rotate to provide uniform target erosion. Targets were exchanged *in-situ* by rotating the entire carousel. A shield was installed to expose only one target at a time and to prevent cross-contamination among the targets during deposition. Fig. 3.8 shows a schematic diagram of the target carousel.

3.3.2. Substrate holder and heater

In pulsed laser deposition of oxide ceramics, it is common practice to bond substrates to a heater plate using some sort of thermally conducting medium such as colloidal silver paint. Unfortunately, the binders and solvents outgas into the chamber during initial low-temperature heating and may compromise the purity of the growth environment if they are not pumped away. To avoid the use of such mediums, the heater plate used in this work was designed to hold a circular substrate by gravity alone – the vertical geometry of the chamber lent itself to such a configuration. Furthermore, the holder was annular in shape and allowed direct radiant heating of the substrate by a pyrolytic-boron-nitride (PBN) coated graphite heating element. Like the target holder,

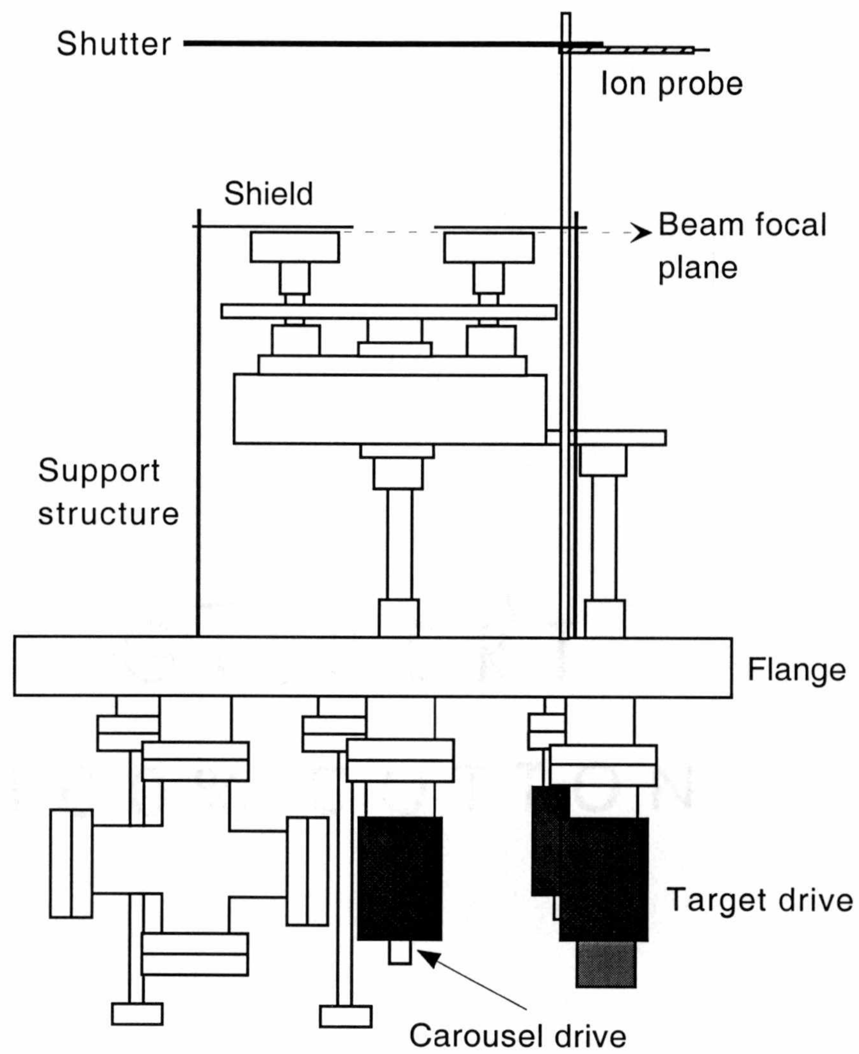

Figure 3.8. Schematic diagram of the target carousel flange assembly for *in-situ* multilayer deposition.

the substrate and heater were rotated to promote uniform deposition. Fig. 3.9 shows a schematic diagram of the substrate heater assembly used in this PLD system. The heater assembly was placed on a chamber port opposite to the target port (see also Fig. 3.1 and Fig. 3.7).

3.3.3. Pulsed valve system

A pulsed solenoid valve and valve controller (Model 60-1-900, General Valve Corp.) were used to generate a pulsed supersonic expansion in the chamber. The position of the exit nozzle of the gas source relative to the ablation point on the target was previously shown in Fig. 3.1. A gas pulse with a 140 μs pulse width at a typical backing pressure of 100 psig contains approximately 10^{17} gas molecules per pulse. The delay between the gas-pulse trigger and the laser-pulse trigger was variable and had an optimum value of 430 μs. The pulsed-valve system consisted of a commercial pulsed valve, a valve controller and a delay generator.

3.3.4. Laser and optics

In this work, a pulsed KrF excimer laser (Lambda Physik Inc., Model LPX 305i λ=248 nm and τ=25 ns) was used as a source of optical radiation. To guide the beam into the chamber, high energy KrF laser mirrors (KRF-2037 for 0° incidence, KRF-2037-45-UNP for 45° incidence, CVI Laser Co.) were used to steer the beam along a 5-meter re-imaging beamline. A single spherical plano-convex fused silica lens (PLCX-50.8-257.5-UV, CVI) was used to image a $1\times 2\ \text{cm}^2$ aperture placed at the laser end of the beamline

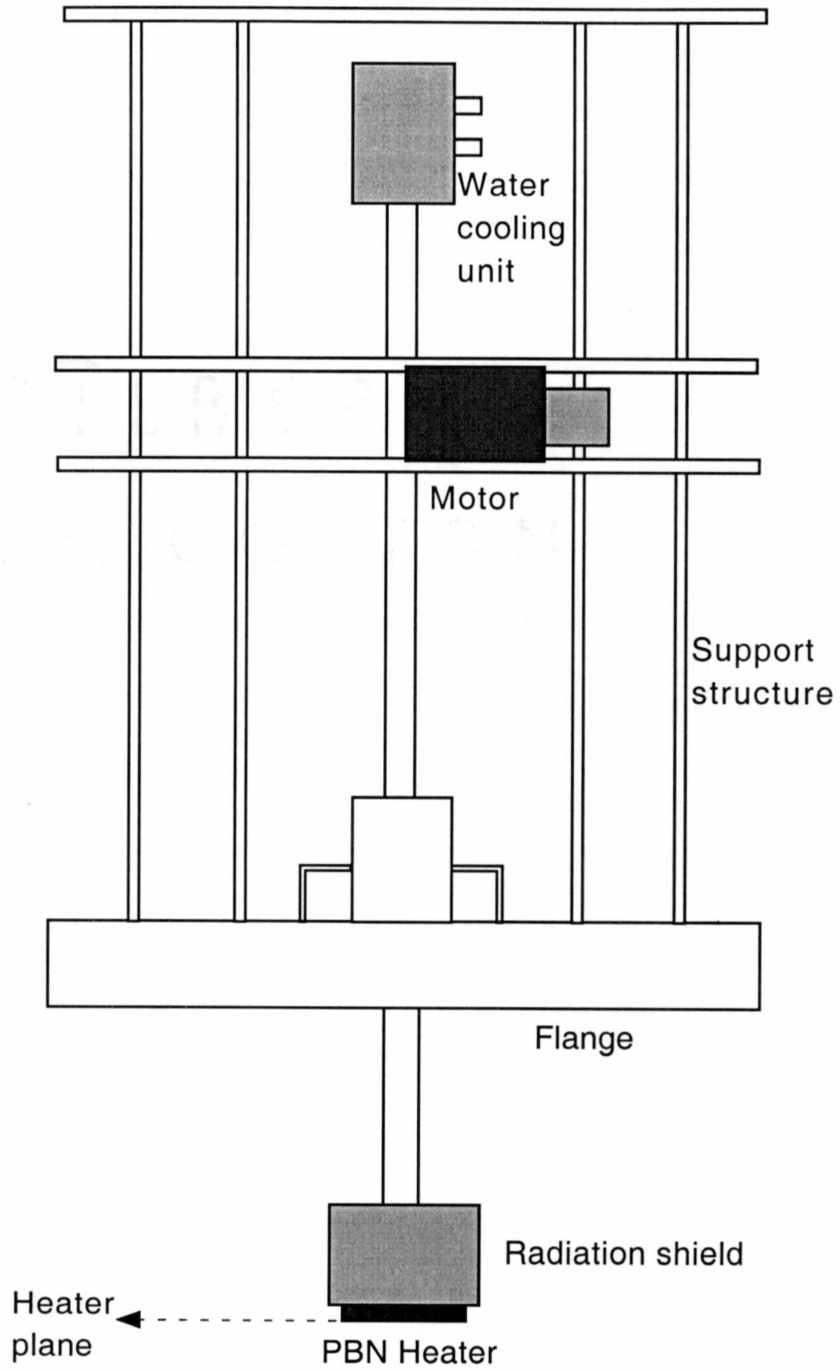

Figure 3.9. Schematic diagram of the rotating substrate heater assembly designed for the PLD process.

onto the target at the chamber end of the beamline. Fig. 3.10 shows a schematic of the optics and the re-imaging beamline (Designed by Dr. C. M. Rouleau).

3.3.5. Ion probe

An ion probe was employed to measure the average time-of-flight (TOF) of the ablation plume. Although there are several methods for ion probing such as wire probes,[81] plane disk probes, and multigrid retarding potential probes, this work employed the wire probe because of its simplicity. The *in vacuo* probe consisted of Kapton-insulated coaxial cable (50 Ω impedance) placed in the path of the plume and biased through an electrical feedthrough (BNC coaxial, 1.33 inch CF, floating shield) by an external bias supply. To provide a reference timing pulse, a high- speed photodetector (DET 110, Thorlabs Co.) was purchased and installed behind one of the laser mirrors (see Fig. 3.10). Fig. 3.11 illustrates the ion probe biasing supply. The supply works as follows: A 30-volt battery charges a 0.1 μF polypropelene capacitor though a 1 kΩ resistor. Until the probe is placed in a conducting medium, such as a laser-induced plasma, no voltage is observed across the 50 ohm load resistor. Thus, the voltage recorded across the load resistor as a function of time after the laser shot is a measure of the coulomb flux passing by the ion probe and hence a temporal signature of the laser-induced plume.

3.3.6. Pumping, vacuum-control and gas-flow systems

Oil-free and dust-free environments are needed for high quality thin-film

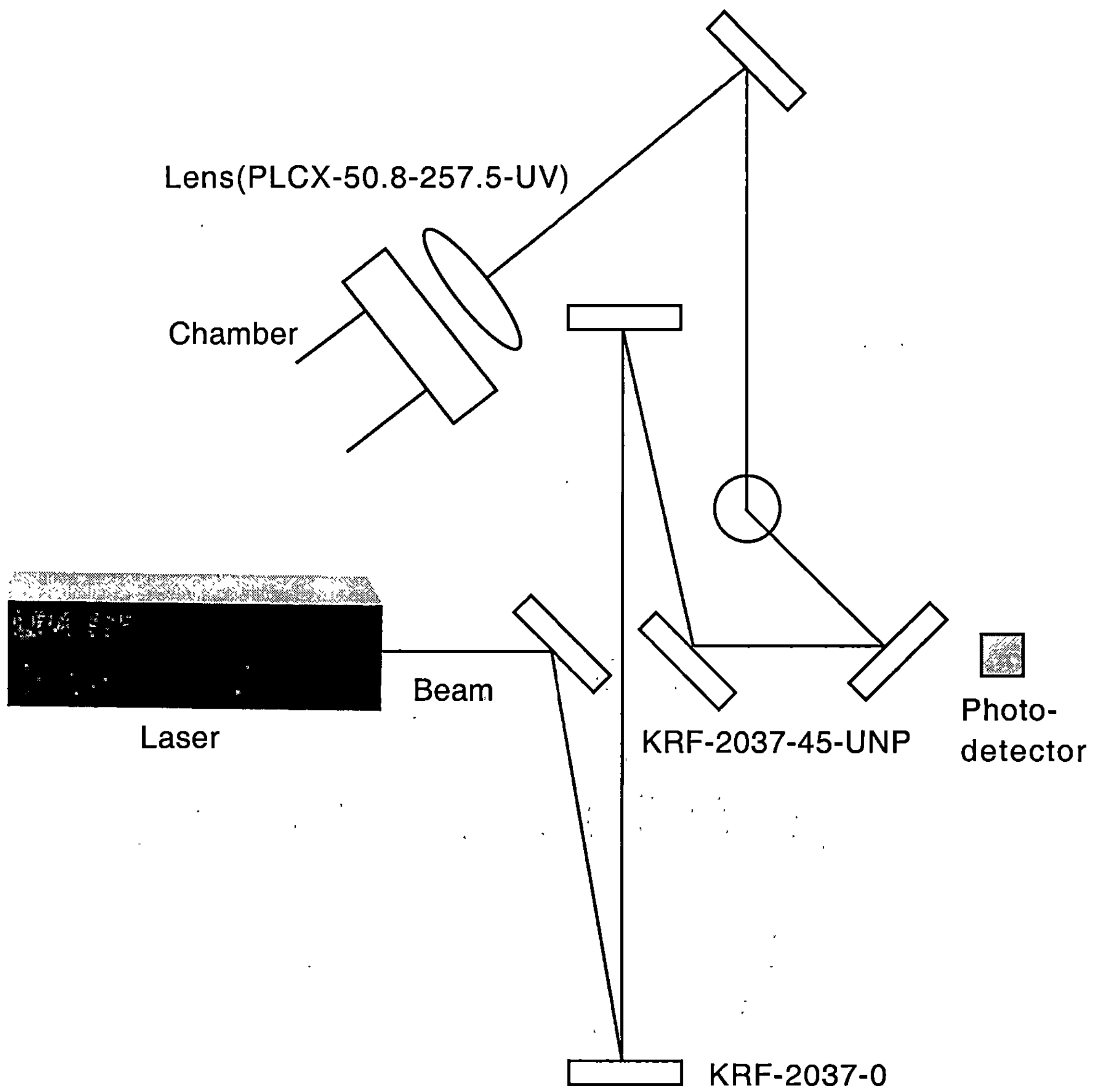

Figure 3.10. Schematic drawing of the re-imaging optics and beam lines used in the crossed-beam PLD technique.

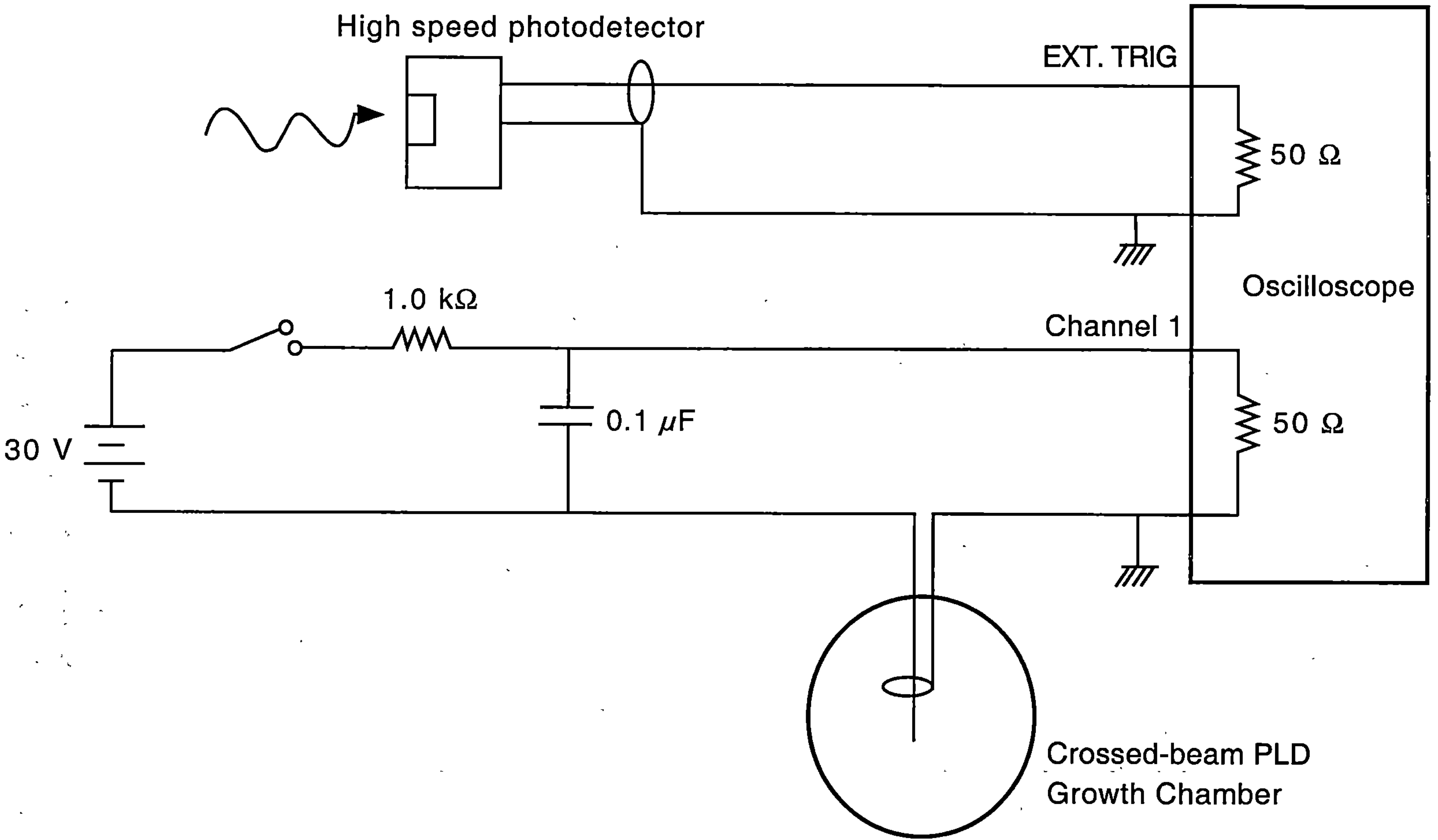

Figure 3.11. Home-made ion probe circuit for the time-of flight (TOF) measurements.

deposition. In some cases, corrosive gas such as NH_3 for the nitride growth is used and can affect the safe and long-life operation of the system. For this reason, a corrosion-resistant turbomolecular pump (Model-TCU520) and power supply (TCP 380) was purchased from Balzer-Pfeiffer Company and a corrosive-service mechanical pump (Alcatel Type 2033CP+) also was used for rough pumping. A Baratron transducer (390HA-00001SP12, MKS Co.) and controller (MKS 270B signal conditioner), butterfly valve (MKS Type 253A-1-40-2-S) and controller (Type 252A-3-VPO) were installed to control the background pressure precisely. An ion vacuum gauge (MDC P/N 432026) and readout (MKS Type 290-01) were used to measure chamber pressure and a thermocouple gauge (MKS Type 6000) and readout (Granville-Phillips 270) were used to measure foreline pressure. Two mass flow controllers (Tylan General, model UC2T-11S01, 10 sccm range, N_2) and readout (Vacuum General, model # 2400) were installed to control gas flow into the deposition system.

3.3.7. Temperature controller

A temperature-control unit was made to control the growth temperature precisely. A programmable temperature controller (CN 4800) and solid state relay were purchased from Omega Engineering Corp. Two switches, an ammeter, fuse, thermocouple wire (Type K) and coaxial cables were prepared and assembled into one control unit whose schematic is shown in Fig. 3.12.

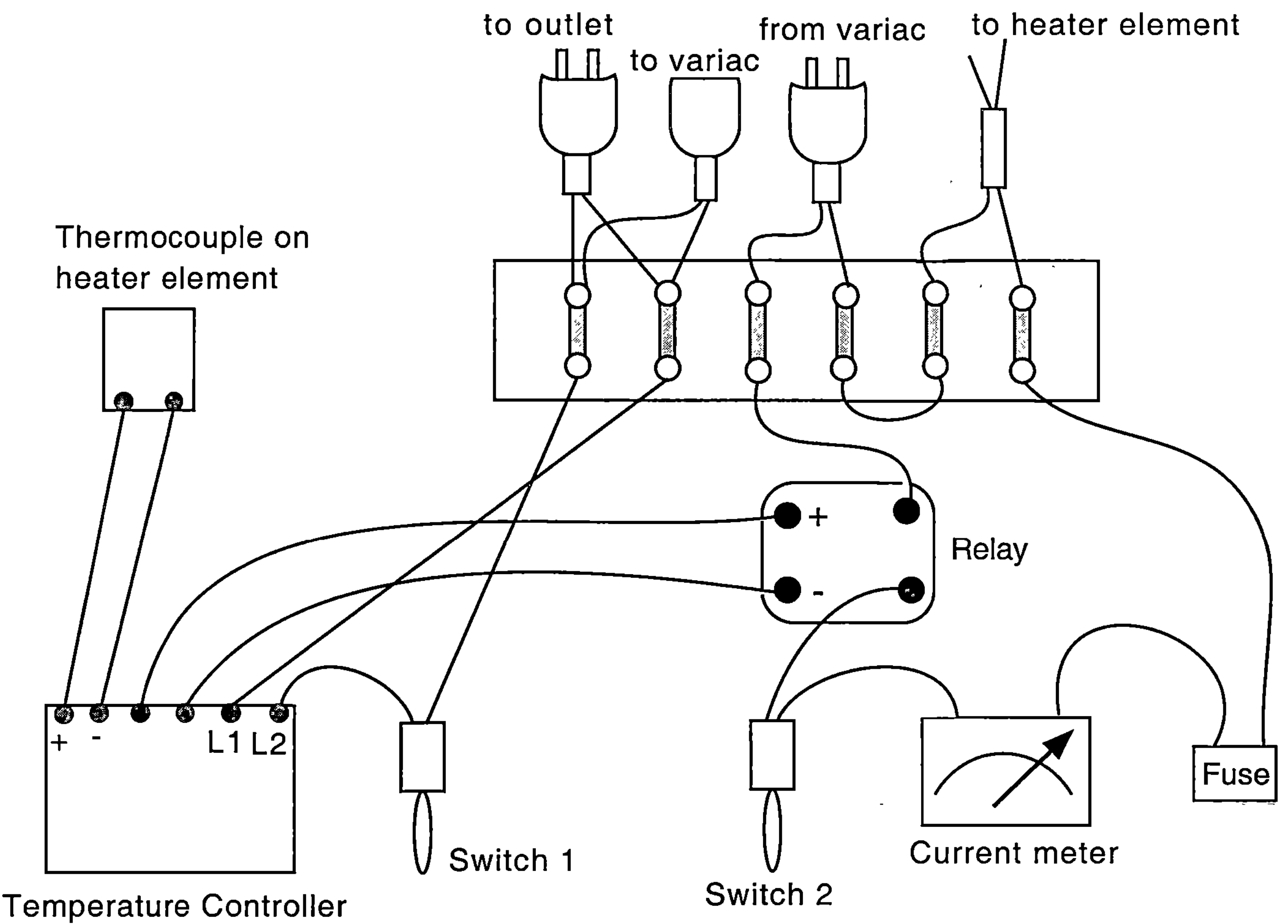

Figure 3.12. Home-made temperature controller circuit for the substrate heater.

Chapter 4

CHARACTERIZATION TECHNIQUES FOR TiN THIN FILMS

In this chapter, the methods employed to characterize TiN films are introduced. Film thickness was determined with profilometry while film morphology was explored with atomic force microscopy (AFM) and scanning electron microscopy (SEM). Transmission electron microscopy (TEM) and scanning transmission electron microscopy (STEM) were used to examine the microstructure of the films while electron energy loss spectroscopy (EELS), a special feature of the STEM, was employed to examine composition on the microscale. The crystallographic quality of the films was determined routinely with *ex-situ* X-ray diffraction (XRD) and *in-situ* reflection high-energy electron diffraction (RHEED). The electrical properties of the films were quantified using temperature-dependent Hall-effect measurements.

4.1. Thickness Determination

The thicknesses of the TiN films were measured using a stylus-based surface profiler (model DEKTAK IIA) from Veeco Instruments Inc. The DEKTAK IIA surface profilometer measures a surface's height profile by moving the specimen beneath a diamond-tipped stylus and then accurately recording the vertical motion of the stylus to within 5 Å over a lateral length scale of 50 μm to 30 mm. To measure the thickness of a film, a mask is usually used during deposition to create an abrupt step between the

substrate and the film. Film thickness measurements were conducted at different locations along such a step to minimize errors.

4.2. Atomic Force Microscopy (AFM)

AFM is a standard instrument for obtaining images of a specimen's surface with slightly less than atomic resolution in the direction perpendicular to the surface. This technique is based on the principle that when a tip, which is attached to the end of a cantilever, is brought within close proximity to the surface of a specimen, interatomic forces will develop between the atoms of the surface and the atoms of the tip and will force the cantilever to deflect. As the tip is scanned across the surface of the sample, the interatomic forces will cause the cantilever to deflect in proportion to the contours of the surface. To obtain topographic information about the specimen, however, one does not measure the deflection of the cantilever. Instead, the cantilever deflection is maintained at a constant value by moving the sample up or down via a piezoelectric actuator - it is the motion of the actuator that translates into topographic information. Cantilever deflection is monitored by reflecting a laser beam off the cantilever and allowing the reflected beam to strike a segmented photodiode array. Any motion of the laser spot as a result of cantilever motion is immediately sensed by the array and then fed to control circuitry that drives the piezoelectric actuator in a direction that brings the cantilever back to its prescribed setpoint. Fig. 4.1 illustrates schematically the principle of AFM.

A three-dimensional image can be obtained by recording the piezoelectric actuator's motion in the Z direction as a function of the sample's X and Y position, also

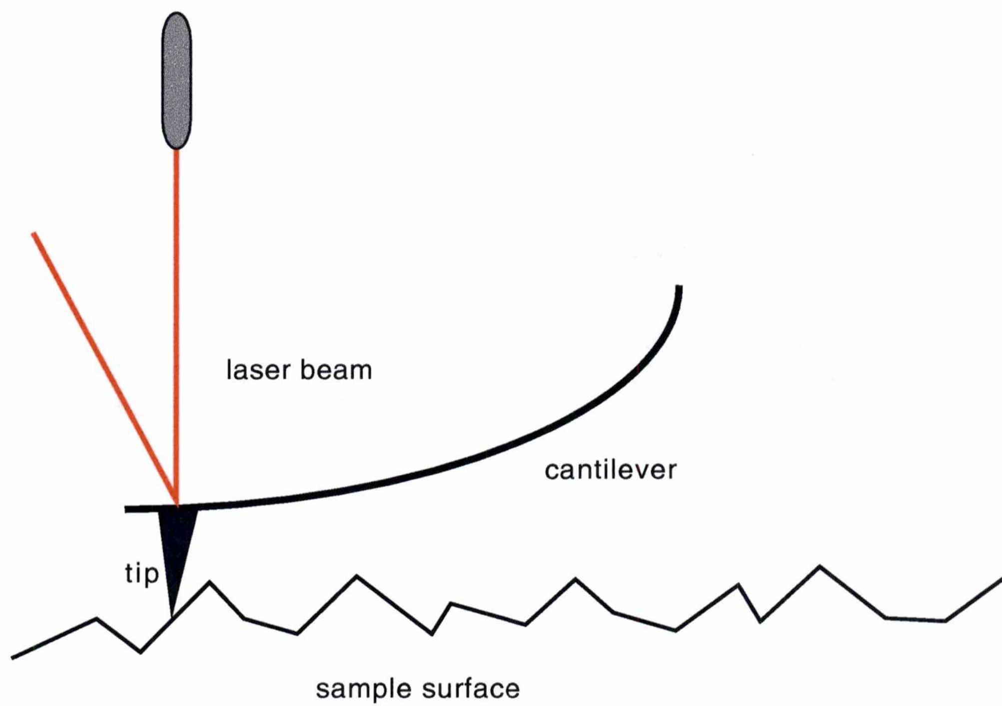

Figure 4.1. AFM principle.

controlled by piezoelectric actuators. A schematic diagram of the process is shown in Fig. 4.2. For the present work, a Nanoscope III Scanning Probe Microscope from Digital Instruments was employed to measure the surface roughness of grown films. The contact mode tips were silicon nitride (Si_3N_4) and resulted in a depth resolution of ~ 0.1 nm and lateral resolution of a few nanometers. A Type "J" (Model AS-130) piezoelectric scanner (125 μm × 125 μm scan size with vertical range of 5 μm) was used.

4.3. Scanning Electron Microscopy (SEM)

In addition to using an AFM to examine surface morphology, a SEM (JOEL model JSM 840) also was used when the film was conducting. The SEM is the most popular and widely used thin-film characterization instrument and relies on a beam of electrons raster-scanned over the surface of the specimen to build an image of the sample's surface. The SEM image is complementary to the AFM in that it has good lateral but poor vertical resolution.

At the heart of an SEM is an electron beam column which consists of a source of electrons, extraction and accelerating potentials, electrostatic and electromagnetic beam-shaping devices, and beam-rastering coils. When the electron beam hits the sample, the interaction of the primary electrons and the sample atoms generates a variety of signals such as secondary electrons, backscattered electrons, transmitted electrons, X-rays, light, heat and specimen current. As these primary electrons move through the sample, they lose their energy and transfer it inelastically to other atomic electrons and to the lattice. This interaction volume is teardrop-shaped and is shown schematically in Fig. 4.3.

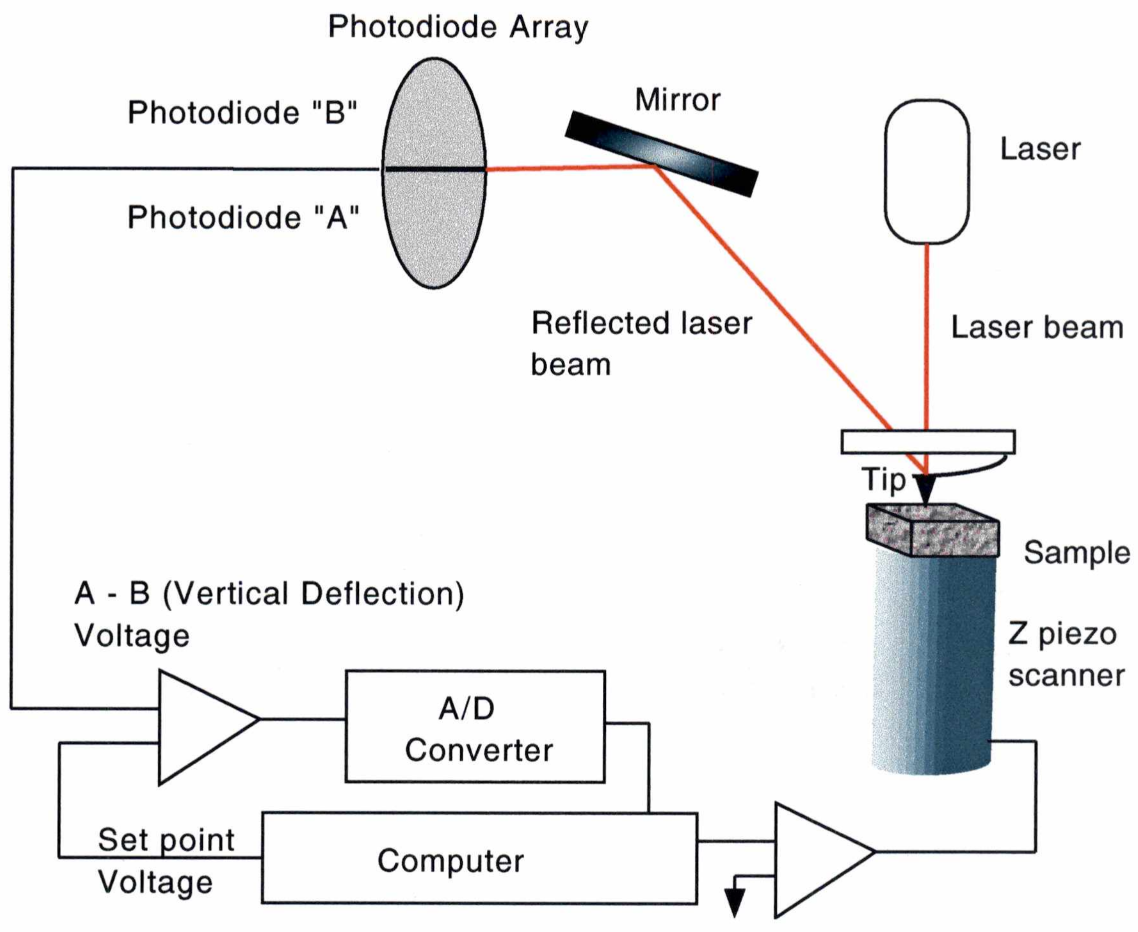

Figure 4.2. Schematic drawing of AFM feedback loop.

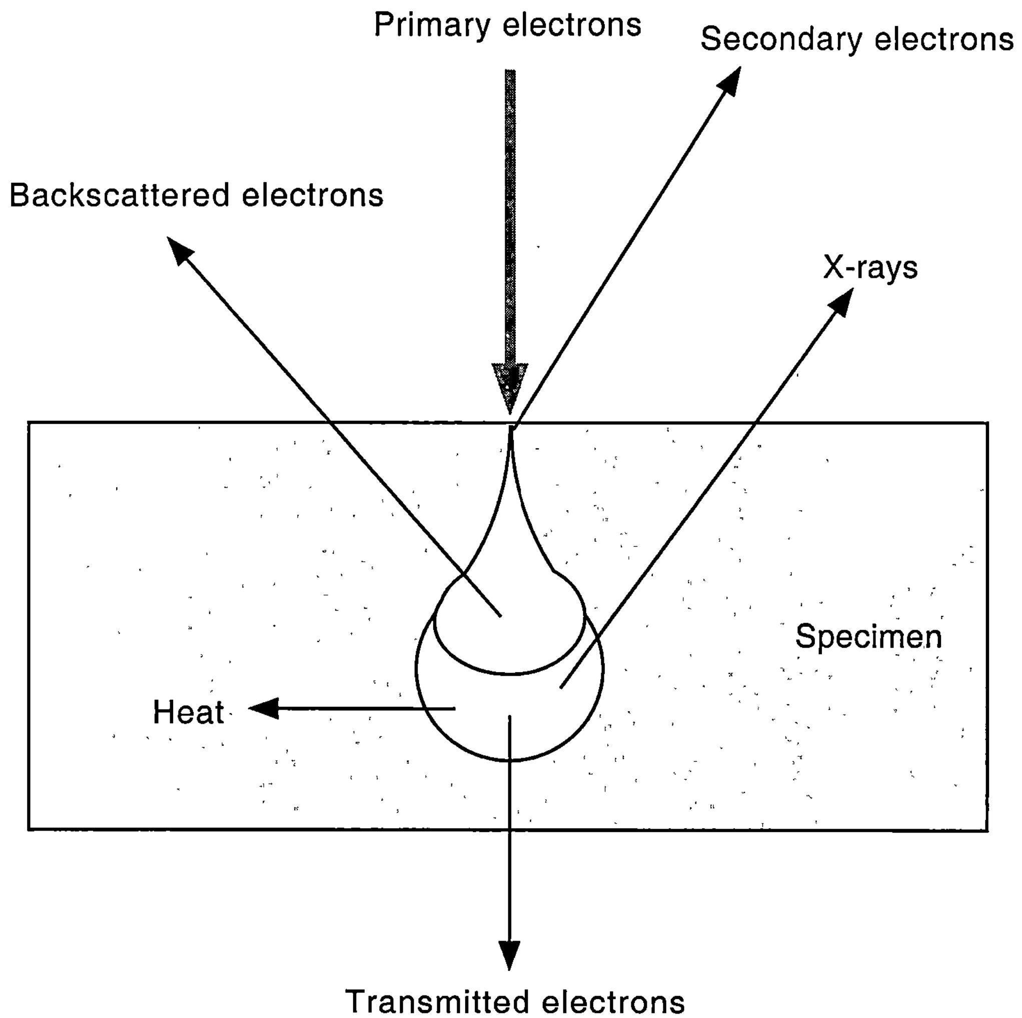

Figure 4.3. Electron and photon signals during electron-beam impingement on the specimen surface.

4.4. Transmission Electron Microscopy (TEM)

Transmission electron microscopy (TEM, Philips model 400) and high-resolution transmission electron microscopy (HRTEM) (Philips-Fetecnai F30-UT) were used for micro-structural analysis of the TiN films. TEM is similar to optical microscopy in principle since the photons are replaced by high-energy electrons and glass lenses are replaced by electromagnetic lenses. The principle of TEM is well-illustrated by Ohring.[82] Again, an electron-beam column forms a nearly monoenergetic beam of electrons (200keV) which is steered through an electron-transparent sample by a condenser lens. Because of the periodic nature of the specimen lattice and the wavelength of the impinging electrons, a fraction of the primary beam forms diffracted beams. The primary and diffracted beams pass through a series of post-specimen lenses. There are two basic operating modes in TEM characterization as shown in Fig. 4.4. The TEM can be operated to form images with bright field, dark field, or lattice image phase contrast and to form diffraction patterns using apertures to select a specific area of the sample and then using an intermediate lens to reimage the diffraction patterns formed in the back focal plane of the objective lens. A bright field image is formed by eliminating intentionally all diffracted beams and only allowing the primary transmitted beam through. Diffracted beams are eliminated by placing suitably sized apertures in the back focal plane of the objective lens and then allowing intermediate and projection lenses to magnify the transmitted beam. A dark field image is formed when an aperture is used to block the primary transmitted beam and all other diffracted beams except for a single diffracted beam.

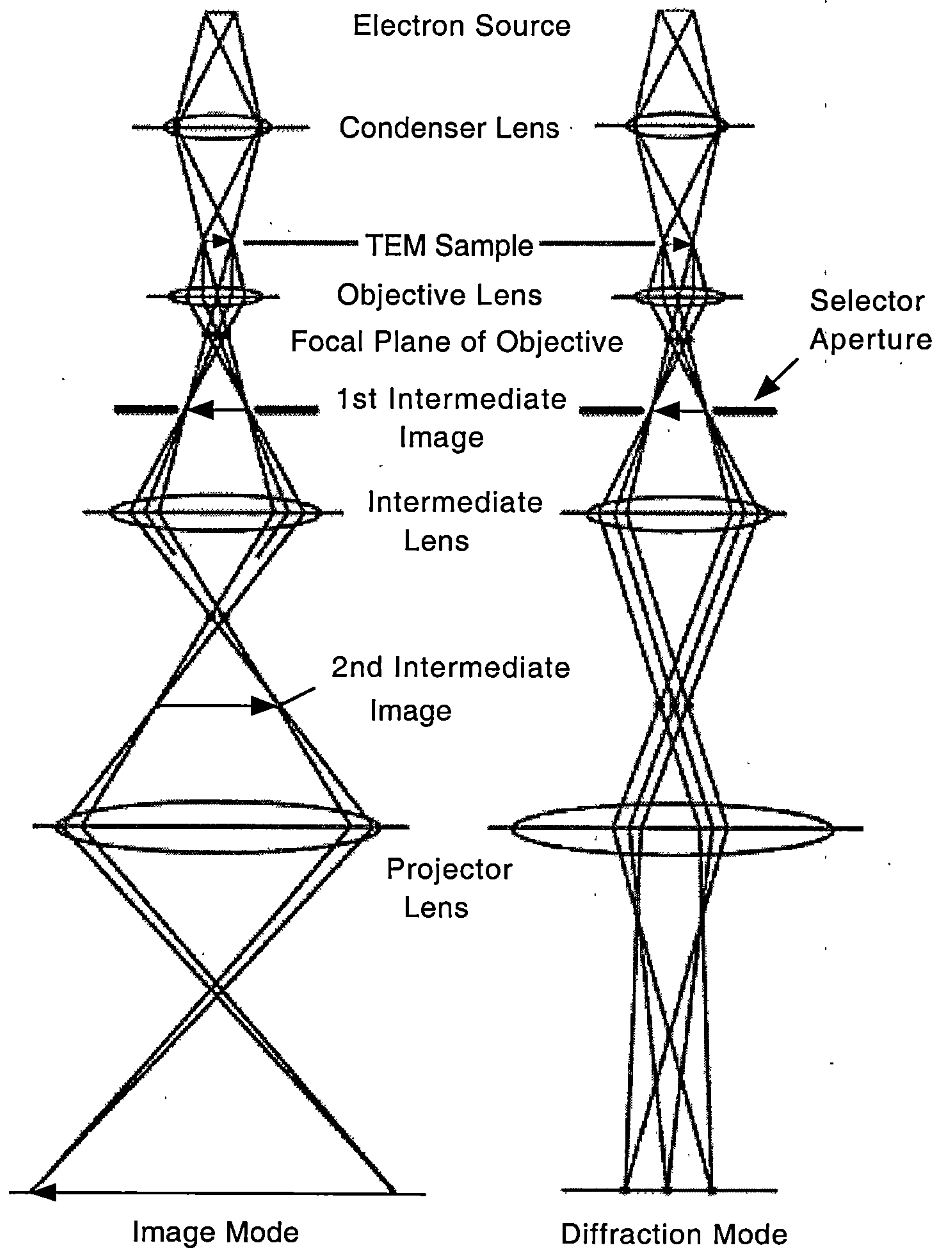

Figure 4.4. Schematic ray diagram in the TEM under imaging and diffraction conditions.

4.5. High-Resolution Scanning Transmission Electron Microscopy (STEM)

Atomic-resolution imaging was performed in a VG Microscopes model HB501 STEM operating at 100 kV with an ultimate resolution of 2.2 Å. The high resolution STEM offers a unique capability for the characterization of thin film interfaces, allowing both atomic structure and impurity sites to be determined directly with atomic resolution. Images in the STEM are produced by scanning the electron beam over the sample. As shown in Fig. 4.5, the objective lens focuses the electron beam onto the specimen and all elastically and inelastically scattered electrons then can be collected by a variety of detectors located behind the sample.

These scattered electrons give information that can be used to produce spectroscopic pictures revealing the specimen's chemistry on a nanometer scale and its structure on an atomic scale. A STEM image can be considered as a collection of individual scattering experiments since the image is produced simply by moving the focused electron beam step-by-step over the sample. Electrons transmitted through the sample can be detected on a bright field detector (BF) on the axis of the microscope or on an annular dark field detector (ADF) which senses electrons scattered within a specific angular range (typically tens of milliradians). In addition, secondary signals (backscattered electrons, secondary electrons, X-rays, etc) can be used for imaging if suitable detectors are attached. Imaging with a resolution equivalent to the minimum probe size is possible using electrons scattered through large angles onto the ADF detector. The intensity of this signal is proportional to square of the average atomic

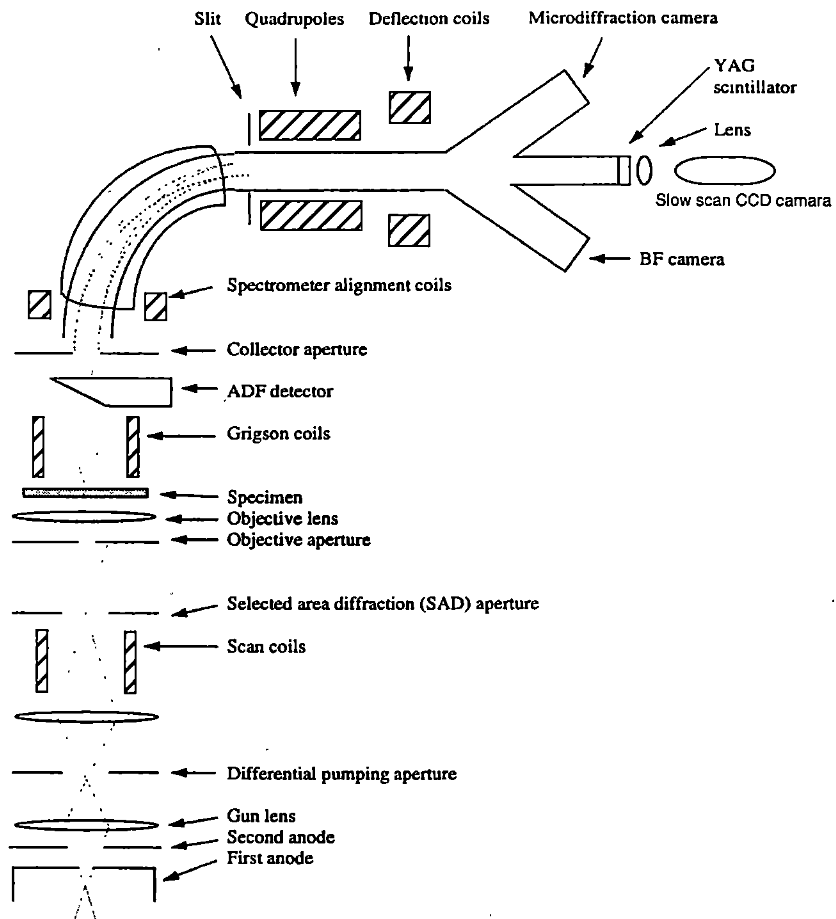

Figure 4.5. Schematic drawing of STEM.

number of the scattering center and thus one is able to get Z-contrast images at atomic resolution. Electrons that are scattered into small angles pass through the ADF detector and are used to form bright field images as well as provide for EELS analysis, which gives chemical and electronic information about the specimen.

4.6. Electron Energy Loss Spectroscopy (EELS)

EELS analysis was performed in a VG Microscopes model HB501 STEM operating at 100 kV with a resolution of 2.2 Å. When the electron beam is incident on the sample, a part of the beam is inelastically scattered and experiences energy loss by exciting electronic transitions characteristic of the atoms in the sample. The distribution of electrons as a function of energy loss is called an energy loss spectrum. Analysis of the energy loss spectrum reveals which elements are present in the sample, as well as information on atomic bonding states. The principle inelastic scatterings are phonon excitations, plasmon excitations, inter/intra band transitions and inner-shell ionizations. Phonon excitations (~ meV) are usually indistinguishable from the zero-loss peak because of instrument resolution. A high-energy electron interacting with outer-shell electrons causes plasmon energy loss peaks below ~100eV; plasmons are a frequent cause of electron energy loss. Also, there are sharp increases in intensity, known as an inner shell edge, when the energy loss due to the excitation of an inner-shell electron is equal to the binding energy of the inner-shell electron.

4.7. X-Ray Diffraction (XRD)

The four-circle x-ray diffraction (XRD) technique was employed to analyze the structural quality of the TiN films. A Picker 4-circle diffractometer (DiffTech 145) was used for this analysis. The acceleration voltage and current were 40 kV and 40 mA, respectively. A nearly monochromatic x-ray beam with low divergence was produced using CuKα radiation. Fig. 4.6 illustrates the X-ray diffractometer and the principle angles involved. Diffraction peaks are measured by orienting the detector angle (2θ) and sample angle (ω,ϕ, and χ) with respect to the incident beam so that an incident maximum is intercepted by the detector.

In principle, XRD measurements come down to measuring distances between crystal planes with planewaves in the x-ray regime. One set of planes is defined by a Miller index of (*hkl*) and each plane in this set produces a reflectance of the incident beam when the Bragg condition $2d(hkl)\sin\theta = n\lambda$ is satisfied.

TiN has the NaCl structure for which the space lattice is face-centered cubic (FCC). One sublattice is occupied by Ti atoms, the other by N atoms. Each atom has 6 nearest neighbors of the opposite kind. Combining both Bragg condition and plane spacing equation,[83]

$$\frac{1}{d^2} = \frac{(h^2 + k^2 + l^2)}{a^2} \qquad (4.1)$$

we obtain

$$\sin^2\theta = \frac{\lambda^2}{4a^2}(h^2 + k^2 + l^2) \qquad (4.2)$$

where λ = 1.5406 Å, a = 4.242 Å for TiN, a = 5.431 Å for Si, and *h*, *k*, and *l* are Miller

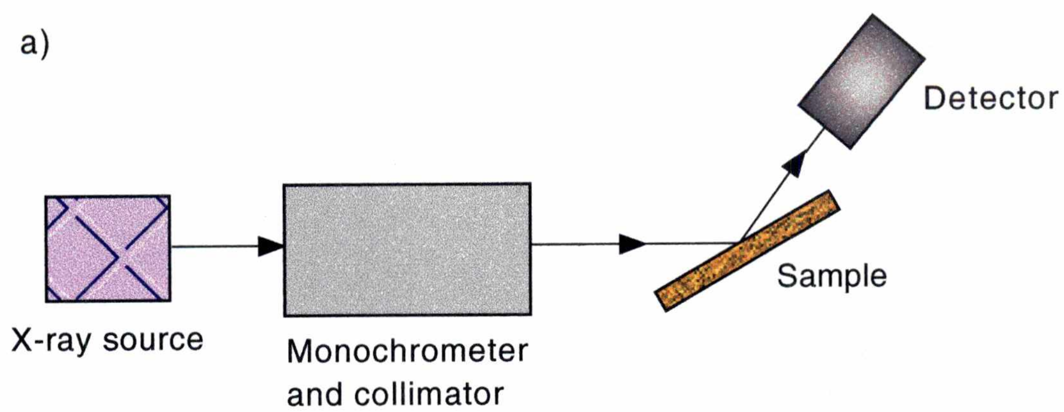

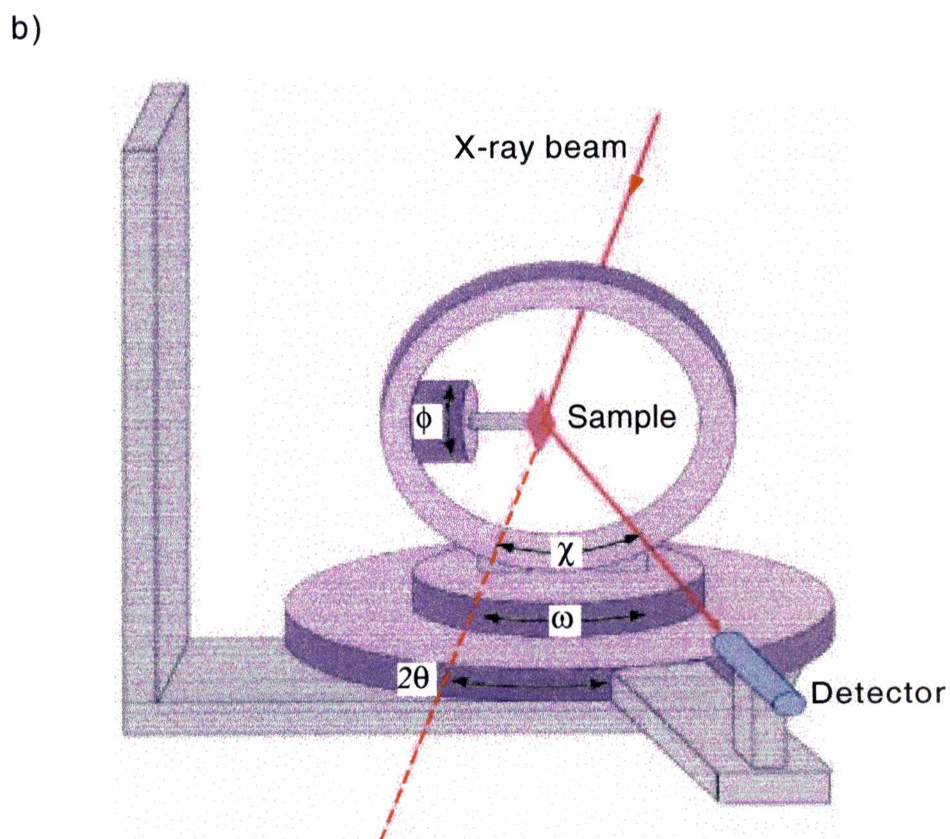

Figure 4.6. A X-ray diffractometer. a) block diagram and b) schematic drawing of the Picker 4-circle diffractometer geometry and relevant angles.[84]

indices. From Eq. (4.2), the expected XRD peaks can be calculated for a TiN(111) film on Si(111) substrate. Expected XRD peaks are $2\theta = 36.663^\circ$ for TiN(111), $2\theta = 77.964^\circ$ for TiN(222) and $2\theta = 28.444$ for Si(111), $2\theta = 58.857^\circ$ for Si(222), respectively.

In addition to precise lattice parameter determination, XRD provides residual stress measurement, the degree of preferred orientation, and qualitative and quantitative phase analysis.

4.8. Energy Dispersive X-ray (EDX) Analysis

EDX was employed to characterize the composition of the TiN films. EDX systems normally reside on a SEM where the electron beam serves to excite characteristic X-rays from the area of the sample being probed. A liquid nitrogen-cooled detector is positioned on the electron microscope as close to the sample as possible in order to intercept the emitted X-rays. Under optimal operating conditions it is possible for EDX to detect all elements from beryllium to uranium in concentrations of ≥ 0.1 atomic percent. However, it can ordinarily detect elements above Na in the periodic table and it has lateral spatial resolution of around $1\,\mu m$. Also, the energy resolution of the peaks is poor (> 100 eV) for EDX. As a variant of X-ray spectroscopy, *wavelength* dispersive analysis (WDX) can be used, with a factor of 20 better resolution in X-ray linewidth (~ 5 eV) than EDX.

The detected X-rays give information about which elements are present (qualitative analysis), and how much of each element is present (quantitative analysis). The EDX detection process starts when photoelectrons are generated by incoming

characteristic X-rays from the sample and then dissipate their energy in a solid state detector by creating electron-hole pairs. The number of pairs produced is proportional to the incident photon energy, producing current pulses of varying height. A low-noise high-gain transimpedance amplifier converts the current pulses into voltage pulses and a multichannel analyzer sorts the voltage pulses according to height and bins them along a voltage (energy) scale.[82] The result is the characteristic X-ray spectrum in EDX analysis. Since the difference in energy between the energy levels involved in the electron transition determines the energy of the emitted X-ray, then each atom in the periodic table exhibits a unique set of K, L, M shell, etc. x-ray spectral lines that serve to clearly identify it.

4.9. Reflection High Energy Electron Diffraction (RHEED)

An electron gun (30kV, Model VE-052S, Veetech Japan Co.) and a phosphor screen (Thermionics) were combined to form a RHEED system. The system was installed to characterize the quality of the substrates before growth and the surface structure of the films after growth.

During RHEED analysis, an energetic electron beam strikes a thin-film surface at a grazing incident angle to produce a quasi-two-dimensional diffraction pattern on a phosphor screen. In this work, the nearly monoenergetic electron beam (30 keV) was focused into the film surface with an incident angle of ~ 1 degree, so that the diameter of the beam spot on the sample was around 90 μm. Electrons are scattered by the periodic potential of the film surface and a characteristic diffraction pattern appears on the

phosphor screen. Both spotted and streaked patterns (as well as mixtures of these) can be observed on the phosphor screen during film growth. Spotty patterns appear as a result of three-dimensional diffraction at islands or surface asperities, while streaky patterns characterize clean and smooth layered two-dimensional film growth. Fig. 4.7 shows the experimental arrangement of the RHEED system. A high-vacuum environment (below 10^{-7} torr) is needed because the electron beam will be scattering by gas molecules and the sensitivity of diffraction will suffer due to adsorbed impurities.

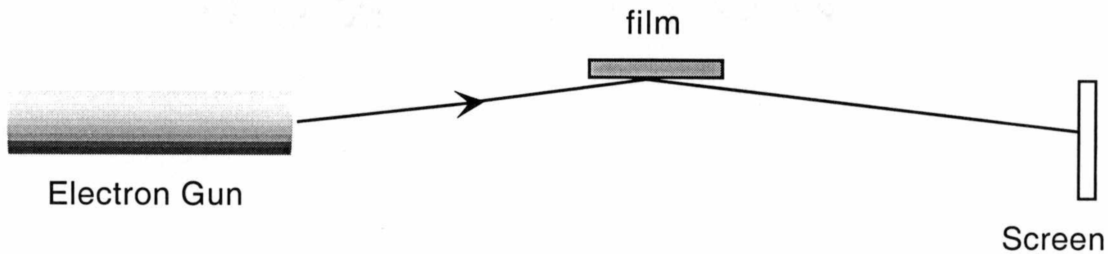

Figure 4.7. A schematic drawing of a RHEED system, with a beam of electrons coming from an electron gun, impinging at grazing incidence onto the surface of a film, and forming a diffraction pattern on a phosphor screen.

4.10. Electrical Resistivity

A custom Hall effect measurement system, constructed by Dr. Chris M. Rouleau and shown in Fig. 4.8, was used to determine the electrical properties of TiN films. To characterize the films at temperatures as low as 10K, a CTI-Cryogenic 8200 compressor and cryostat were employed. The remainder of the system consisted of a programmable current source (Keithley 220), a sensitive digital voltmeter (Keithley 182), and an autotuning temperature controller (LakeShore 330). An electromagnet (20 kG) and field-regulated magnet power supply (Varian Fieldial™ Mark I) were used to provide a very stable magnetic field during the measurements. By performing Hall effect and resistivity measurements, one can determine the type of majority carriers, their concentration, and the Hall mobility. The Hall carrier concentration and mobility differ from the true values by a numerical factor, r_H, the Hall factor. In this study, the Hall factor was assumed to be unity.

The Van der Pauw method,[85] which is shown in Fig. 4.9, was used to measure electrical resistivity of the films for temperature ranging from 10K to 300K. Ohmic contacts were made by Indium (99.995% purity) dots simply pressed onto the four corners of the samples. A magnetic field strength of 8kG was used since it gave the smallest error in the Hall coefficient and resistivity values. The resistivity value, ρ, can be derived from the formula[82]

$$\exp(-\frac{\pi d}{\rho}\frac{V_{CD}}{I_{AB}}) + \exp(-\frac{\pi d}{\rho}\frac{V_{DA}}{I_{BC}}) = 1 \qquad (4.3)$$

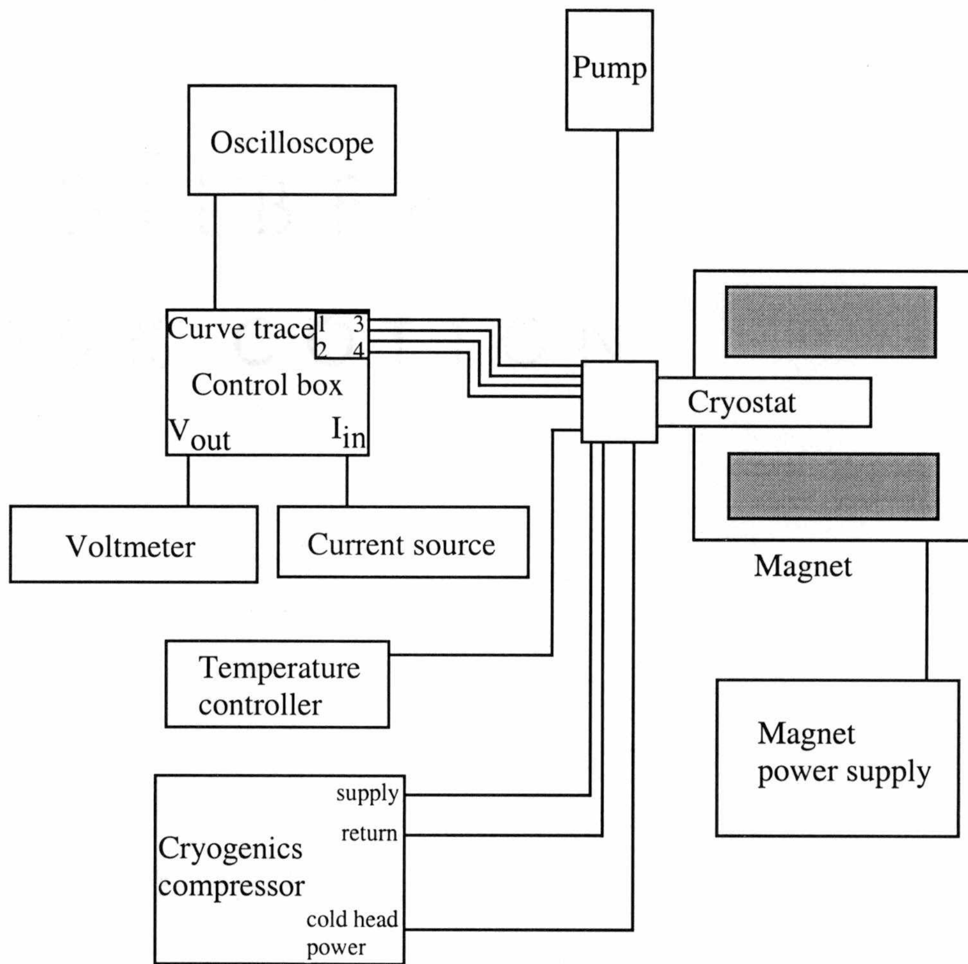

Figure 4.8. Schematic drawing of home-made Hall effect measurement system.

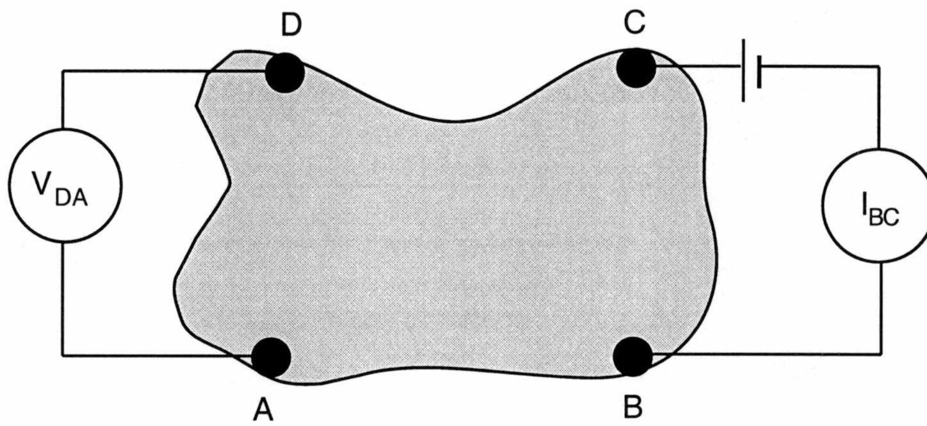

Figure 4.9. Van der Pauw method for measuring electrical resistivity.

Chapter 5

TiN THIN-FILM GROWTH BY CROSSED-BEAM REACTIVE PLD AND ITS CHARACTERIZATION

A reactive, orthogonally crossed-beam pulsed laser deposition (PLD) technique has been employed to grow TiN thin films on Si substrates with a view toward development of thin-film devices.

5.1. Substrate Preparation

5.1.1. Substrate temperature calibration

The substrate heater assembly used in this work was equipped with a Chromel-Alumel thermocouple, which was positioned to mechanically contact the backside of the pyrolytic boron nitride (PBN) heater element. Since the substrate was heated radiantly and a 4-mm gap existed between the substrate and the heater element, the temperature as read by the thermocouple was expected to be quite different from the actual surface temperature of the substrate. In order to obtain a relationship between the actual substrate temperature and the thermocouple reading, optical pyrometry was employed. The substrate temperature calibrated by optical pyrometry is shown in Fig. 5.1.

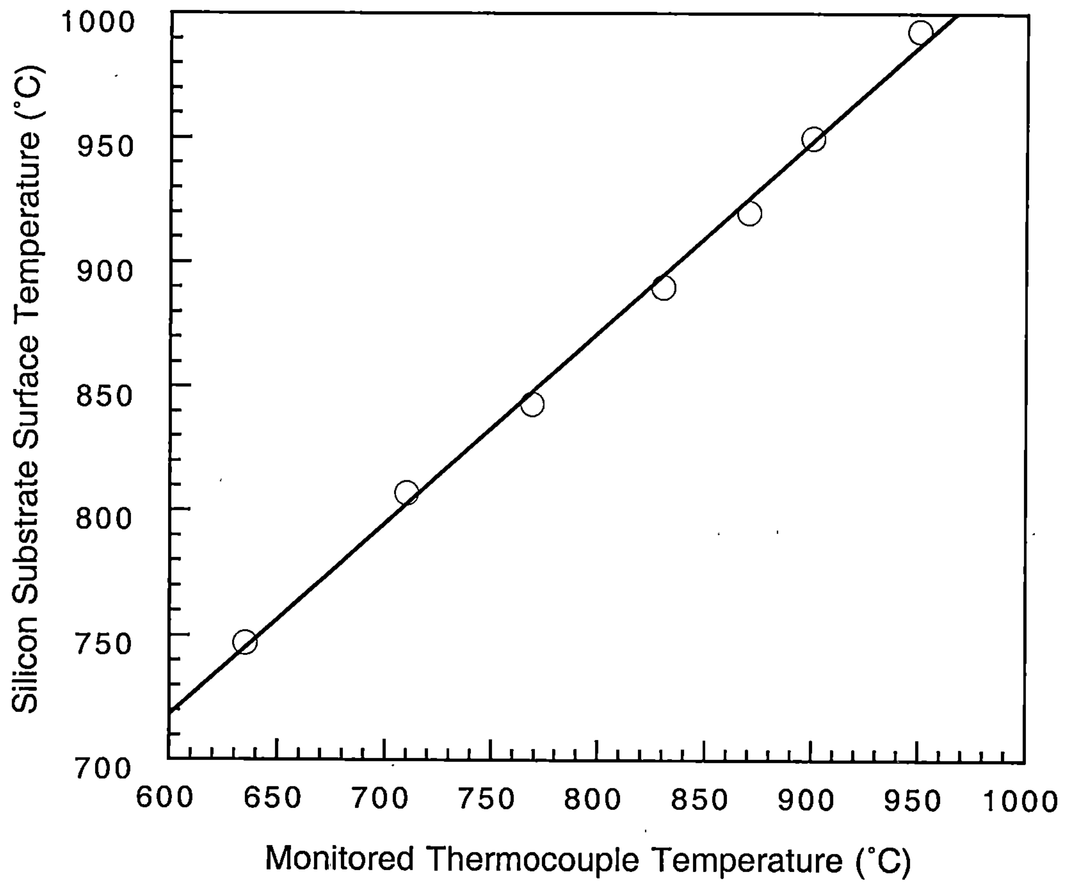

Figure 5.1. Plot of silicon substrate surface temperatures obtained using optical pyrometry vs. monitored temperatures

5.1.2. Substrate cleaning

The silicon substrates were (111)-oriented and purchased from SEH (Shin Estu Handotai). They were cleaved into equilateral triangular segments with a diamond scribe to facilitate mounting in a 1-inch diameter substrate holder. The substrate specifications are listed in Table 5.1. For epitaxial growth the substrate surface condition plays a critical role, since the structure of the epitaxial layer initially follows the surface arrangement of the substrate. The substrate surface needs to be free of contamination and damage.

Instead of using wet-chemical processes to strip the native oxide off the as-received Si wafer, a standard high temperature thermal oxide desorption step was employed *in-situ*. After loading the sample and holder into the chamber, the chamber was pumped down to 10^{-3} torr by a mechanical pump and then to 2×10^{-7} torr by a turbomolecular pump. The temperature was then slowly ramped to 900 °C to thermally desorb the native oxide. The oxide desorption process was monitored *in-situ* by reflection high energy electron diffraction (RHEED), which also was used to inspect the quality of the subsequent TiN layers. A characteristic RHEED pattern of the Si(111) surface was routinely observed along the <110> azimuth of Si immediately after thermal cleaning at 900 °C. Fairly diffuse patterns were recorded from the Si surface prior to the thermal cleaning, indicating a poorly ordered surface structure. A series of RHEED pattern recorded during this process is shown in Fig. 5.2. As shown in the figure, from room temperature to 600 °C diffuse patterns were observed. It should be noted that during the temperature ramp and including 880 °C, the Si pattern remained

Table 5.1. Specifications of Si substrates used to grow TiN thin films.

Crystal Size	Cleaved 1cm x 1cm x 1cm from 3" wafer
Crystal thickness	0.38 mm
Crystal Orientation	(111)
Carrier type and Concentration	n-type
Crystal symmetry	Cubic (diamond)
Surface finish	One side polished
Resistivity	0.3 Ω-cm
FWHM of X-ray rocking curve	0.4°
Lattice parameter	a = 5.4301 Å
Thermal expansion coefficient	3.59×10^{-6}/K

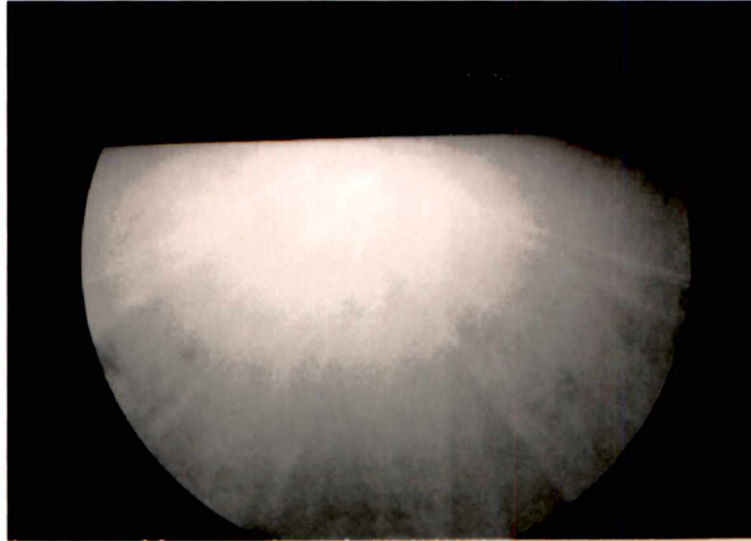

(a) Room temperature

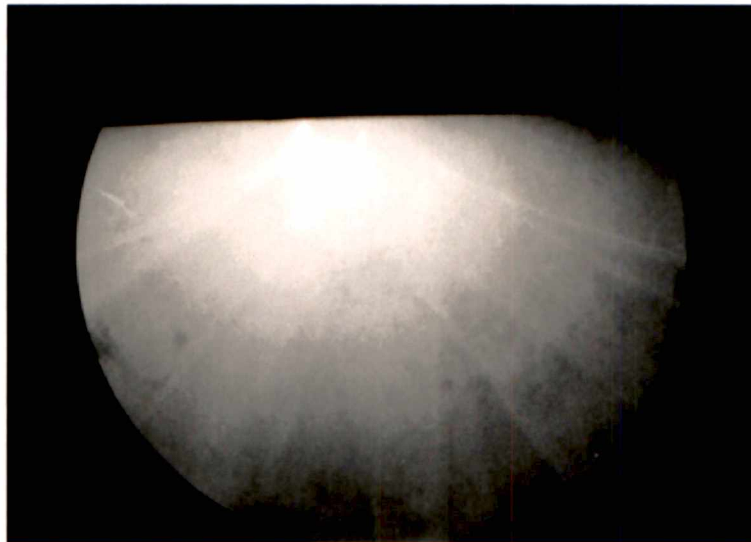

(b) At 300 °C

Figure 5.2. RHEED patterns recorded at various temperatures along the <110> azimuth of Si.

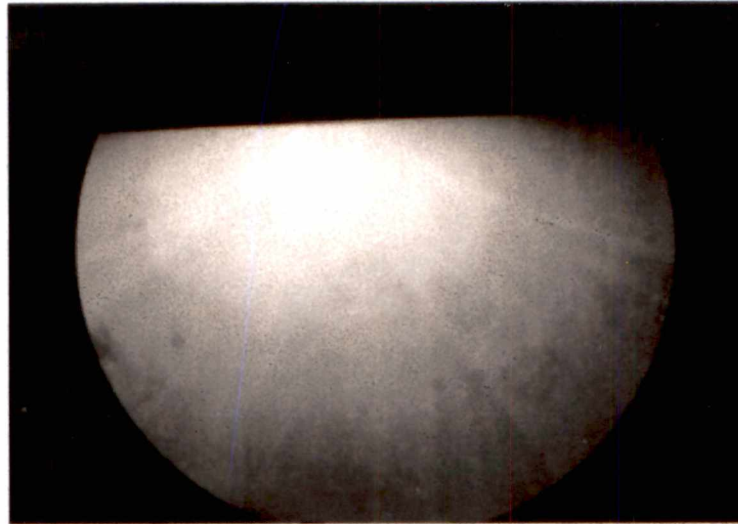

(c) At 600 °C

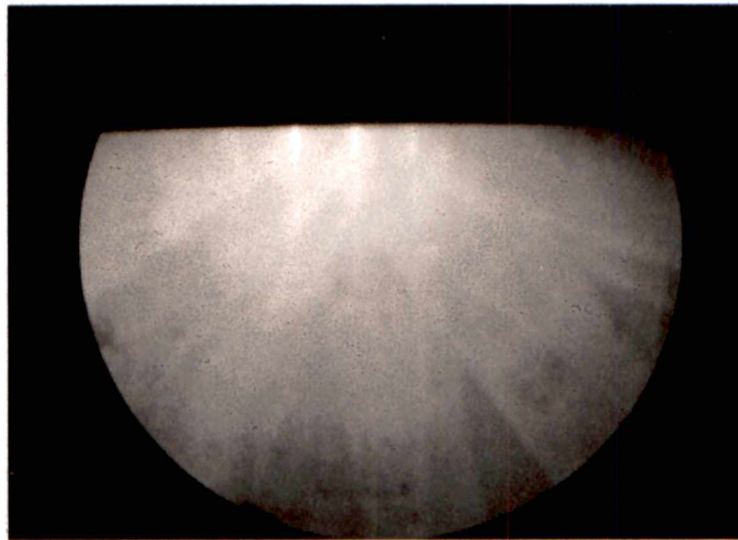

(d) At 900 °C

Figure 5.2. (continued).

diffuse. Specifically at 900 °C, however, a sharp streaky diffraction pattern with Kikuchi lines developed and indicated oxide desorption, the formation of a smooth and clean surface, and a well ordered (1×1) Si (111).[86]

5.2. TiN Film Growth

Immediately after the *in-situ* thermal cleaning process, the substrate temperature was changed quickly to the deposition temperature for the TiN film growth. Thin films of TiN were deposited on triangularly-cleaved Si(111) substrates by pulsed KrF laser (LPX 305i, λ=248 nm and τ=25 ns) ablation of a high purity Ti metallic target (99.999 % purity, 1 inch diameter) through a supersonic N_2 jet (99.9999 % purity) formed by a pulsed solenoid valve (General Valve Corp.). The distance between the laser spot on the Ti target and the pulsed-valve nozzle was 1.3 cm and the Ti plume and pulsed N_2 jet crossed orthogonally. The target-substrate separation, D_{ts}, was 5 cm. The target was ablated using a reimaging beamline (i.e., single spherical lens imaging an aperture onto the target with demagnification) with the laser beam incident on the target at an angle of 45°.

Prior to every deposition, the target was preablated for 1,000 shots to remove any oxide skin that might have formed on it during sample transfer into the chamber. The chamber was pumped to 1×10^{-7} torr prior to deposition and the time-averaged N_2 background pressure during deposition was ~2×10^{-4} torr for all of the film-growth runs.

Substrates were mounted freely (held in place by gravity) and were heated radiantly using a pyrolytic-boron-nitride (PBN) heater. Depositions were carried out at a

substrate temperature of 750 °C. Both the target and substrate were rotated with constant speed to obtain more uniform ablation and deposition, and a total of 20,000 laser shots at 5 Hz repetition rate were used for each film. Vacuum TOFs ranging from 2.0~3.7 μs were used for the deposition.

5.3. Time-of-Flight (TOF) Measurements

Measurements of the TOF of the ablated species were performed using an ion probe. To maximize the overlap between the Ti plume and the N_2 gas pulse, the delay between the laser trigger and the pulsed valve driver trigger was adjusted until a maximum TOF was observed during ion probing. These results are shown in Fig. 5.3. As shown in the figure, the optimum delay was also independent of the initial mean kinetic energy imparted to the plume (i.e., vacuum TOF). This is consistent with the fact that nearly all of the required delay resulted from instrument delay and not the transit time for either the plume or the gas pulse. It should be further noted that a pulsed valve driver gate width of 140 μs was chosen to limit the time averaged pressure in the chamber to $\sim 2\times10^{-4}$ torr at 5 Hz. At this pressure, N_2 had a mean-free-path nearly five times the separation between the substrate and the target, so that this condition tended to provide a region after the mixing regime that was sufficiently rarified to allow for collisionless expansion toward the substrate. Additional TOF measurements as a function of lateral separation between the plume plane and the gas pulse plane revealed that maximum overlap was far more sensitive to lateral alignment between the valve

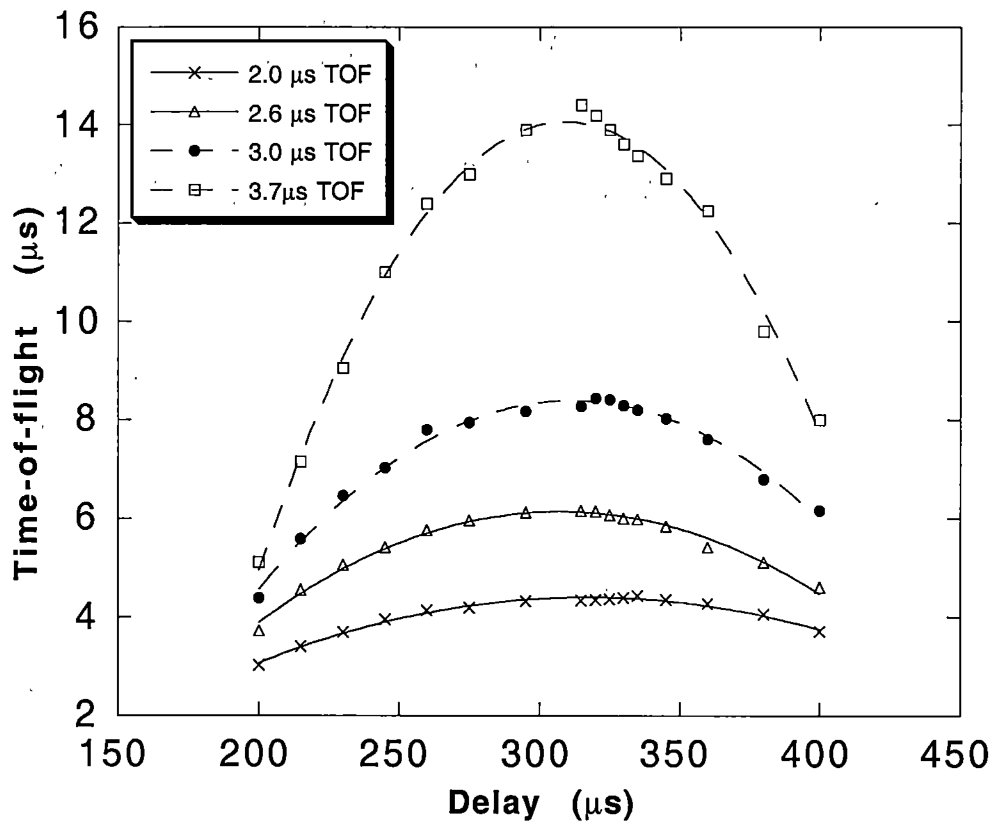

Figure 5.3. Ablated species time-of-flight versus delay between the pulsed valve driver trigger and the laser trigger.

and laser spot than to the delay timing. Although the TOF was halved for lateral deviation of +/- 6 mm from the optimum, we found that visual sighting (aligning the laser spot with respect to the valve nozzle) easily maintained the required spatial overlap from run-to-run. Vacuum TOFs for Ti ranging from 2.0-3.7 μs (corresponding to kinetic energies of 155 to 45 eV) were used for the depositions. Each TOF was set by either adjusting the laser reservoir voltage (15-23 kV) and/or using a series of fused-silica plates placed in the beam as laser beam attenuators, i.e. by controlling the laser energy density focused onto the target.

5.4. Epitaxial Growth of TiN Thin Films

5.4.1. Thin film growth modes

It is very important to understand film growth mechanisms because they strongly influence the film microstructure, properties and orientation.

When atoms impinge on a solid surface, there is finite probability that the atoms diffuse along the surface by hopping from one potential well minimum to the next, but there is also a probability of atoms leaving from the well to the vacuum level. Atoms deposited on the surface tend to "look" for atomic sites that minimize the total energy of the system. The atoms incident on a substrate may desorb from the surface immediately or after undergoing some surface diffusion. The frequency of desorption (or desorption rate) is defined as[87]

$$\nu_d = \nu_s \exp\left(-\frac{\Delta E_d}{kT}\right) \tag{5.1}$$

where ΔE_d is the change in free energy associated with desorbing one atom and ν_s is a surface vibration frequency ($\nu_s \cong 10^{13}$/s). The residence time of an atom on the surface, τ_s, is given by[87]

$$\tau_s = \nu_d^{-1} = \nu_s^{-1} \exp\left(\frac{\Delta E_d}{kT}\right) \tag{5.2}$$

Within the time interval τ_s, an atom moves from one surface site to a neighboring surface site with a diffusion frequency, ν_D,

$$\nu_D = \nu_s \exp\left(-\frac{\Delta E_s}{kT}\right) \tag{5.3}$$

where ΔE_s is the activation energy for surface migration. The surface diffusion coefficient is defined by[87]

$$D = D_0 \exp\left(-\frac{\Delta E_s}{kT}\right) \tag{5.4}$$

where $D_0 = a^2 \nu_s$, and a is the jump distance between two neighboring surface sites.

We may consider the behavior of an atom on a stepped surface where the mean distance between steps is R_0. For growth to proceed, it is required that the atom diffuse to a step before desorption occurs. For arrival at the step to occur before desorption then the surface diffusion length

$$\sqrt{4D\tau_s} > \frac{R_0}{2}, \tag{5.5}$$

where $R_0/2$ is the largest distance to the step. The diffusion time t_D for an atom to reach the step is given by[87]

$$t_D = \frac{R_0^2}{16D} \tag{5.6}$$

If we define the ratio r to be

$$r = \frac{\tau_s}{\tau_D} = \frac{\text{residence time}}{\text{diffusion time}}, \tag{5.7}$$

then by taking τ_D to be a characteristic diffusion time of R_0^2/D, we find that $\tau_D = 16\ t_D$. Clearly when $r \geq 1$, an atom will have enough time to diffuse to the step and will become bound on the surface. When $r < 1$, desorption becomes increasingly likely to occur. From Eq. (5.7),

$$r = \frac{a^2}{R_0^2} \exp\left(\frac{\Delta E_d - \Delta E_s}{kT} \right) \tag{5.8}$$

When diffusing atoms impinge on and join other atoms or clusters, they contribute to nucleation, and then thin-film growth begins. Deposited atoms can react with the surface to form new chemical compounds, or they can react with each other to form larger two-dimensional clusters called islands. There are three conventional growth modes: Frank-van der Merwe (FM), Volmer-Weber (VW), and Stranski-Krastanov (SK), which are shown schematically in Fig. 5.4. In FM growth mode, a film grows two-dimensionally, monolayer-by-monolayer, resulting in the formation of planar sheets. The VW growth mode occurs when the smallest stable clusters nucleate on the substrate and grow in three dimensions to form islands. In SK growth mode, initial layer-by-layer growth (FM) converts to VW growth after forming a few monolayers. This growth mode is common in metal-semiconductor systems but the transition from two-dimensional to three-dimensional growth is still not completely understood.

Equations representing constraints relating the growth modes can be obtained by considering a nucleus on a substrate to be cap-shaped, having a contact angle θ, as shown

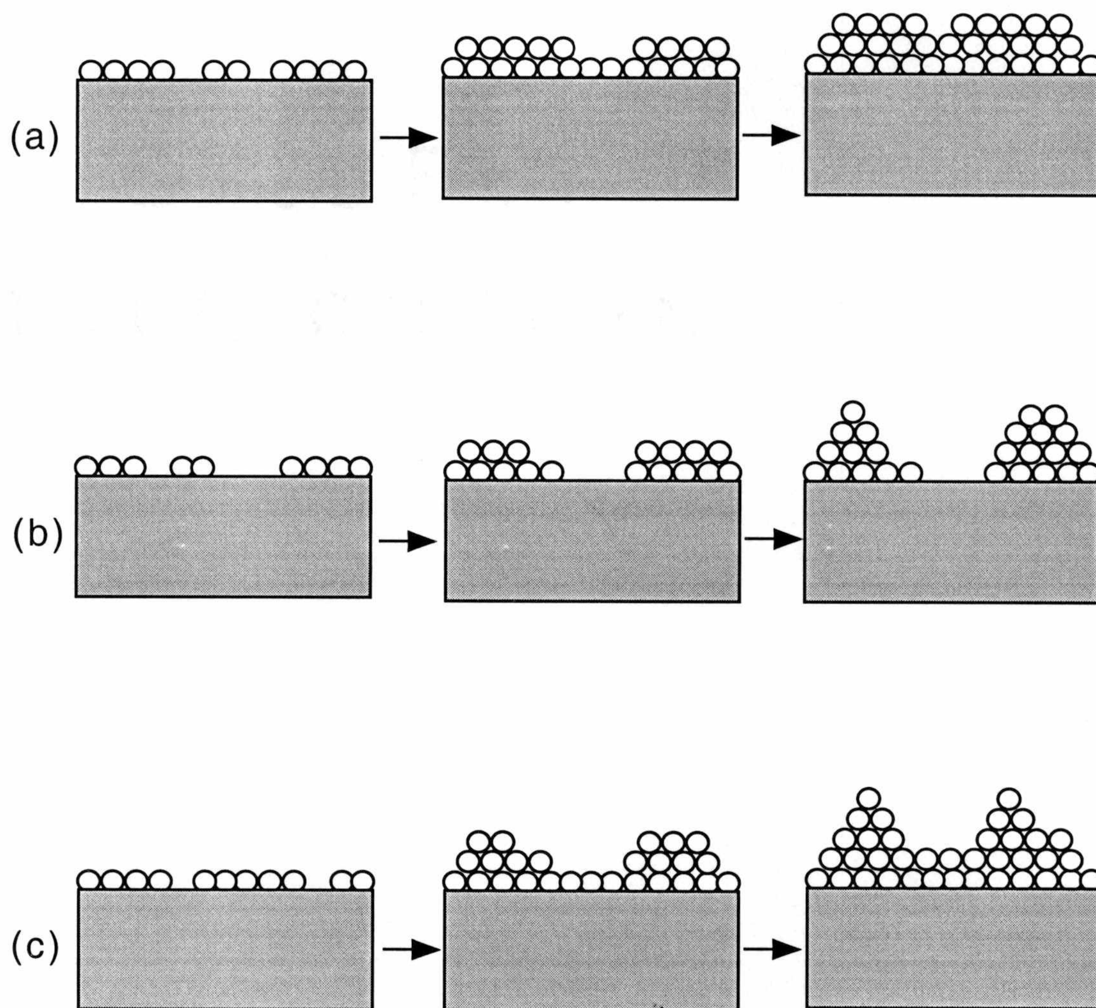

Figure 5.4. Three basic growth modes. (a) layer by layer (Frank-Van der Merwe) (b) island (Volmer-Weber), and (c) Stranski-Krastanov.[82]

in Fig. 5.5. Consideration of the mechanical equilibrium among the interfacial tensions or forces yields Young's equation[88],

$$\sigma_{sv} = \sigma_{fs} + \sigma_{vf} \cos\theta \tag{5.9}$$

where the subscripts f, s, and v refer to the film, substrate, and vapor, respectively. By thermodynamic definition, interfacial energy, σ, is the excess Gibbs free energy of the entire system per unit area of the interface, which is given by

$$\sigma = \left(\frac{\partial G}{\partial A} \right)_{T,P} \tag{5.10}$$

Interfacial energy between two phases is an important parameter to control the structure and physical properties of a growing film near the interface. A variety of methods such as the capillary rise, contact angle measurements, zero creep, and Johnson-Kendall-Robert

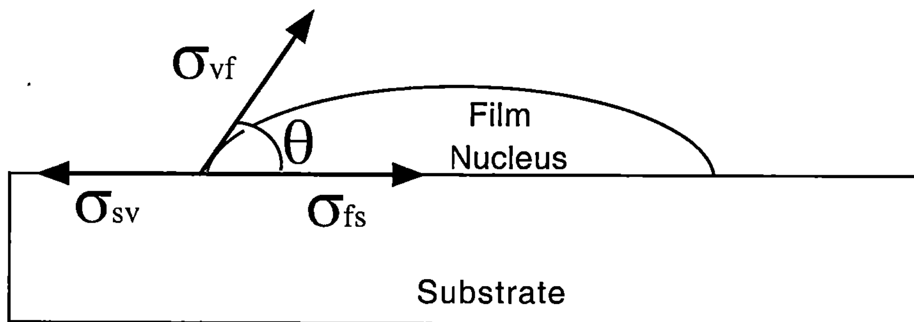

Figure 5.5. Schematic of a cap-shaped nucleus on a substrate surface.

(JKR) are employed mostly for measuring interfacial energy.

The three basic modes of film growth can be distinguished on the basis of Young's equation. For $\theta = 0$, the nucleus wets the substrate completely, and therefore

$$\sigma_{sv} = \sigma_{fs} + \sigma_{vf} \tag{5.11}$$

When the interface energy σ_{fs} is smaller than σ_{vf}, this leads to FM growth mode because an additional atom will preferentially attach along the interface layer to keep the system in a state with the lowest free energy. When the interfacial energy between the film and substrate vanishes, i.e. $\sigma_{fs} = 0$, this is called ideal homoepitaxy as a special case of this condition.

However, the case of

$$\sigma_{sv} > \sigma_{fs} + \sigma_{vf} \tag{5.12}$$

results in SK growth. When σ_{fs} is larger than σ_{vf}, the atom can lower its energy by attaching at the overlayer. For $\theta > 0$,

$$\sigma_{sv} < \sigma_{fs} + \sigma_{vf}, \tag{5.13}$$

and this results in VW growth, island growth for which the nucleus only partially wets or does not wet the substrate.[82]

5.5. RHEED Analysis

RHEED patterns of the TiN films were all sharp and streaky but diffraction spots

also were present. Fig. 5.6 shows the RHEED patterns of TiN films grown at 750 °C with different times-of-flight (different kinetic energies). As the deposition started, the RHEED pattern of the Si substrate disappeared and a new diffraction pattern developed. It should be noted that during *in-situ* monitoring no bright diffuse background was observed in the initial growth stage, which suggests that an amorphous layer was not present between the film and substrate. This was confirmed by subsequent high-resolution TEM, STEM and EELS analysis. A reconstructed (2×2) surface structure was observed after 20,000 shots for all the cases. Reconstructed (2×2) surface structures during the film growth were generally believed to arise from the unintentional presence of foreign atom species on the surface. For example, one group reported that a (2×2) reconstructed TiN surface was due to O_2 contamination.[89] However, EDS and EELS analysis showed that there were no foreign atomic species present in the films resulting from the present work. Additional TiN film growth was performed using the same experimental conditions but a conventional TiN target was used and the crossed-beam technique was not employed. The surface structure of the films grown using this conventional technique did not show any reconstructed surface.

Diffraction patterns for the films grown at TOFs of 2.0 μs and 2.6 μs were more sharp and streaky than those grown at longer TOFs (3.3 μs and 3.7 μs), indicating more smooth films. Intense diffraction spots with streaks were observed in the initial growth stage of films grown at 3.3 μs and 3.7 μs TOFs, indicating more three-dimensional growth (Volmer-Weber or Stranski-Krastanov growth mode). These patterns may be

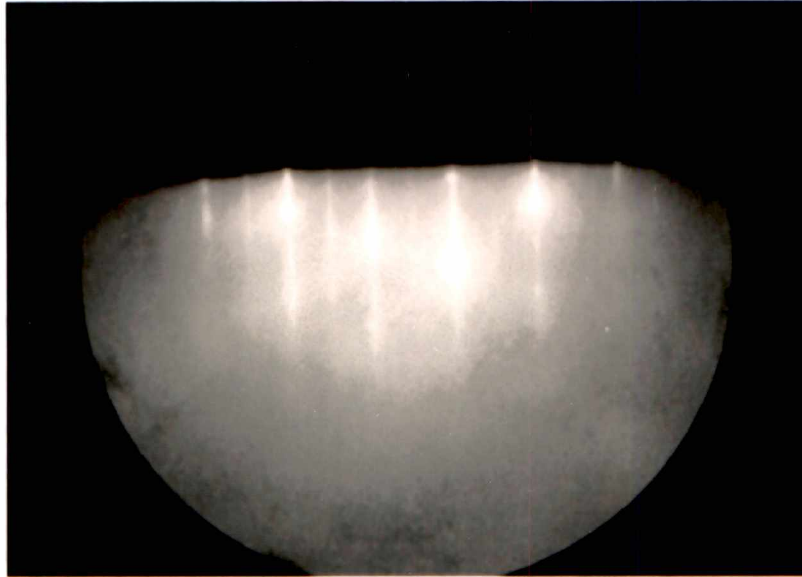

(a) With 2.0 μs TOF

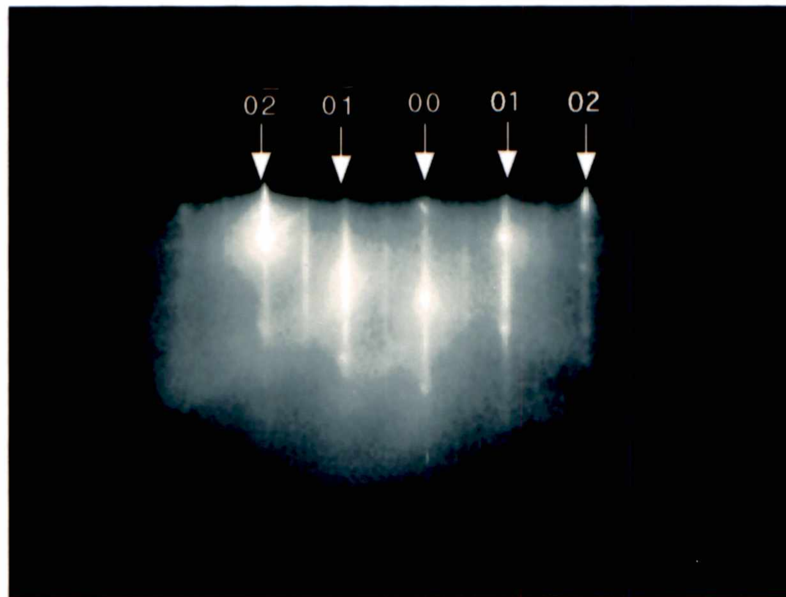

(b) With 2.6 μs TOF

Figure 5.6. RHEED patterns with different TOFs. (2×2) structures were observed. The azimuth of the electron beam is parallel to the [110] direction.

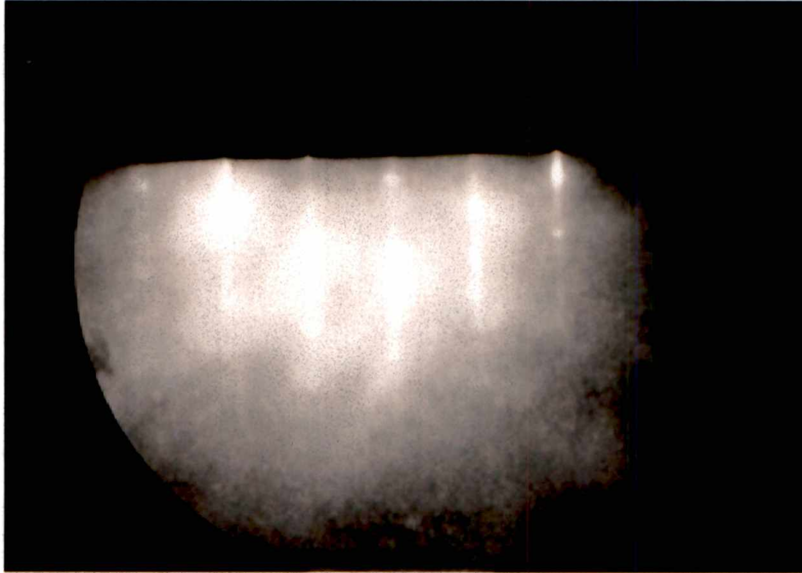

(c) With 3.3 μs TOF

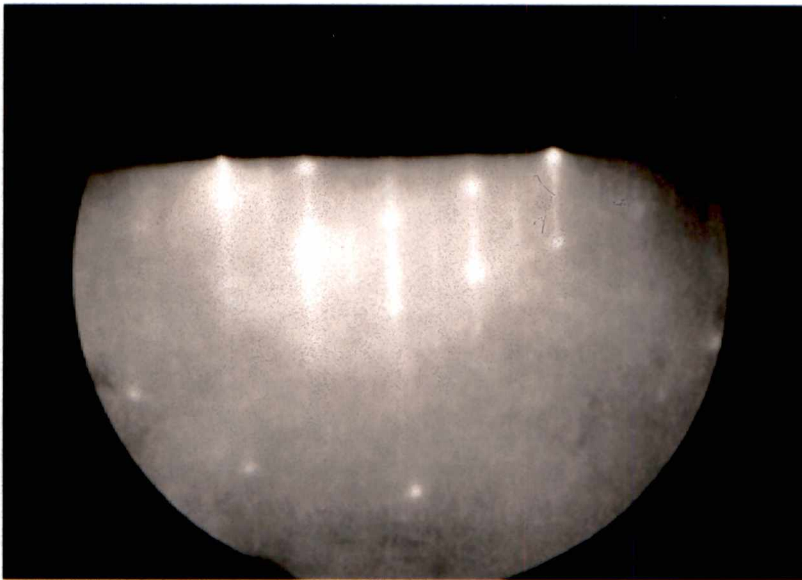

(d) With 3.7 μs TOF

Figure 5.6. (continued).

caused by a high density of atomic steps formed by low surface mobility atoms. These results were in agreement with SEM and AFM results. Under optimal conditions (TOF = 2.6 μs), the diffraction pattern was sharp and streaky and AFM showed a more smooth surface morphology. After 500 shots (≈1.8 monolayers), the RHEED pattern was sharp and streaky and indicated a two-dimensional growth mode but diffraction spots began to appear after 1,000 shots, indicating TiN film-growth was becoming more three-dimensional.

According to these RHEED results, TiN grown with fast TOFs (2.0 μs and 2.6 μs) followed the Stranski-Krastinov growth mode, whereas films grown with slow TOFs (3.3 μs and 3.7 μs) followed the Volmer-Weber growth mode. This experimental data supports the idea that higher kinetic energy ablated species impinging on the growing film surface enhances surface mobility so that it improves surface morphology and crystalline quality.[90]

5.6. X-Ray Diffraction Analysis

5.6.1. Structure of lattice-mismatched systems

In a lattice-matched heterostructure, the epitaxial layer is called either strained or unstrained. Both strained and unstrained systems are illustrated in Fig. 5.7. Because of the constraint on the in-plane lattice constant, the unit cell of the epilayer on the substrate will distort according to Poisson's ratio. If the bulk lattice constant of the epilayer is smaller than that of the substrate, the unit cell will be stretched in the in-plane direction

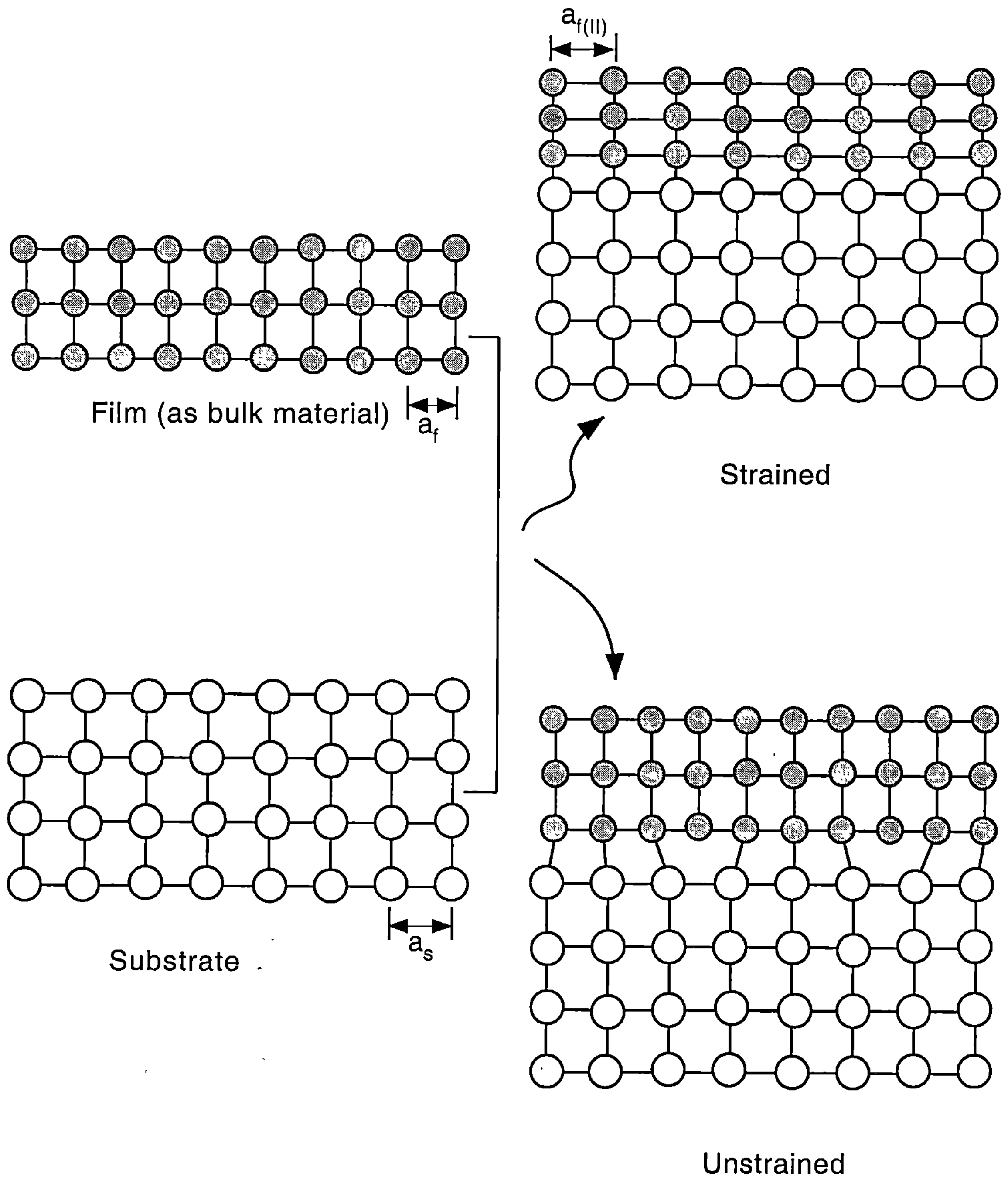

Figure 5.7. Illustration of a lattice-mismatched heterostructure that is either strained or unstrained (relaxed to the bulk lattice constant).

and its height will shrink. The in-plane strain $\varepsilon(||)$, which is also called coherency strain, is defined by[87]

$$\varepsilon(||) = \frac{a_{f(||)} - a_f}{a_f} \tag{5.14}$$

where $a_{f(||)}$ is the in-plane lattice constant of the grown film, and a_f is the lattice constant of the film in the bulk. The out-of-plane strain $\varepsilon(\perp)$, which is in the perpendicular direction to the interface, also can be defined as[87]

$$\varepsilon(\perp) = \frac{a_{f(\perp)} - a_f}{a_f} \tag{5.15}$$

where $a_{f(\perp)}$ is the film's lattice constant perpendicular to the surface.

If a metal or semiconductor film has a cubic structure in the bulk state, then strained-layer epitaxy will convert it to a noncubic structure with a tetragonal unit cell. The tetragonal distortion is given by[87]

$$\varepsilon_T = \frac{|a_{f(\perp)} - a_{f(||)}|}{a_f} \tag{5.16}$$

High-resolution x-ray diffraction was used to analyze the crystalline quality of the TiN films. Because the lattice constant of bulk TiN is $a_0 = 4.242$ Å the epilayer unit cell is smaller than that of the Si substrate ($a_0 = 5.4301$ Å). Thus, the film's unit cell was stretched in the in-plane direction and its height was decreased. Therefore, all the TiN thin films were under out-of-plane compression with tetragonal distortion. This is a common phenomenon in lattice-mismatched systems in heteroepitaxial film growth.

The lattice parameters were measured by XRD using the so-called $\sin^2\psi$

technique[83] which is usually used to measure biaxial stress of the films. The relation between the angle ψ and the measured sample is illustrated in Fig. 5.8.

Using this technique, the lattice parameters of TiN films grown at different TOFs were obtained and are shown in Fig. 5.9. As shown in the figure (and as expected), the lattice constants in the in-plane direction were increased whereas the lattice constants out-of-plane were reduced. The in-plane and out-of-plane strain and tetragonal distortion of the grown TiN films at different TOFs are calculated and listed in Table 5.2.

The dependence of tetragonal distortion on TOF is shown in Fig. 5.10. The tetragonal distortion is larger at both fast and slow TOF but has its minimum value for the optimal TOF of 2.6 μs, which means that less strained films can be grown epitaxially in this regime.

Fig. 5.11 shows a θ-2θ x-ray diffraction pattern of a TiN thin film deposited on Si(111) at 750 °C with a 2.6 μs TOF, our optimal conditions. The diffraction pattern contained only the Si(111) and TiN(111) families and indicated that the TiN film was highly oriented along the (111) direction and essentially phase-pure. Similar patterns were noted for films grown at different TOFs. The lattice constants were found to be $a_0(\perp)$=4.236 Å and $a_0(||)$=4.243 Å (bulk TiN a_0 = 4.242 Å) and indicated that the film was under out-of-plane compression with a tetragonal distortion of 0.00039.

Figures 5.12 (a)-(d) show x-ray rocking curves and phi-scans of TiN films grown with different TOFs. As shown in the figure, the FWHM of the TiN(111) reflection ranged from 0.3° ~ 0.67°, which indicates excellent out-of-plane texture. This value

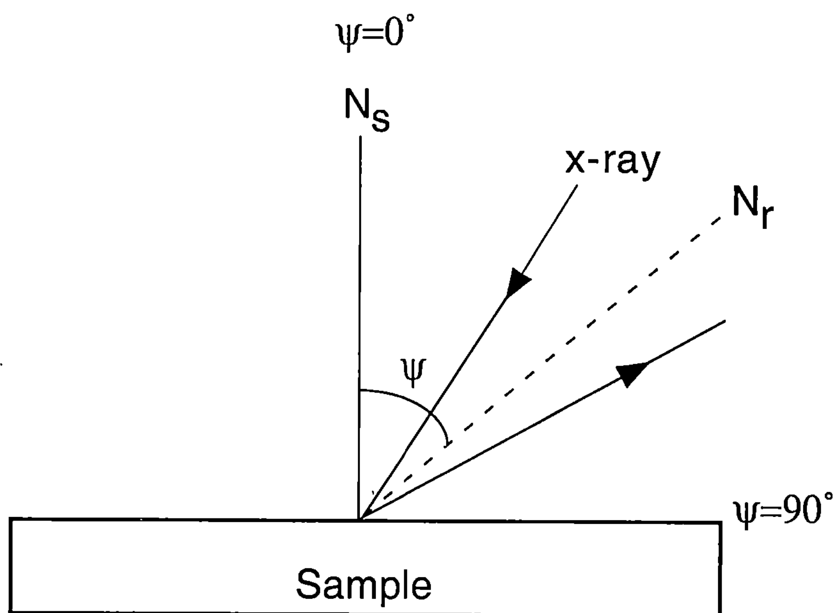

Figure 5.8. Illustration of the angle ψ relative to the sample surface for measuring lattice parameters (N_s = normal to the sample surface, N_r = normal to planes reflecting the x-ray beams).

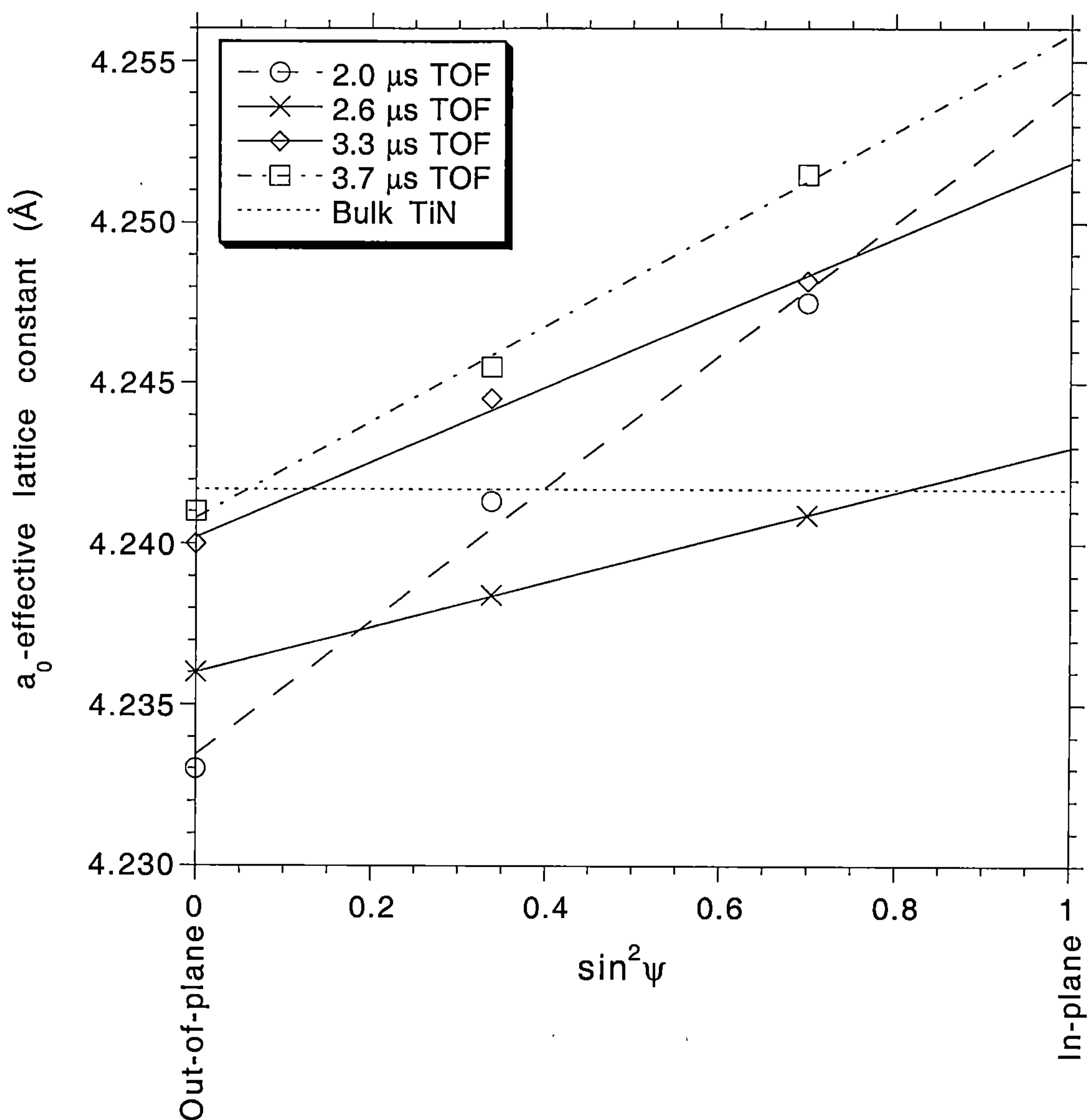

Figure 5.9. Lattice parameters as a function of the angle ψ for different times-of-flight (TOF). Lattice constants were measured while varying the angle ψ. Out-of-plane lattice constants, a(⊥), were obtained at ψ=0° and in-plane lattice constants, a(||), were obtained at ψ=90°, as listed in Table 5.2.

Table 5.2. Lattice parameters, strains and distortions of the TiN films with different times-of-flight.

TOF	$a(\perp)$ (Å)	$a(\|\|)$ (Å)	In-plane strain $\varepsilon(\|\|)$	Out-of-plane strain $\varepsilon(\perp)$	Tetragonal distortion (ε_T)
2.0 μs	4.233	4.254	2.83×10^{-3}	-2.12×10^{-3}	1.17×10^{-3}
2.6μs	4.236	4.243	2.36×10^{-4}	-1.41×10^{-3}	0.39×10^{-3}
3.3 μs	4.240	4.252	2.36×10^{-3}	-4.71×10^{-4}	0.67×10^{-3}
3.7 μs	4.241	4.256	3.30×10^{-3}	-2.36×10^{-4}	0.83×10^{-3}

is much lower than previously reported for TiN(111)/Si(111)[91] and is even better than the rocking curve width reported for TiN(111) grown on 6H-SiC(0001).[92] To this author's knowledge, the lowest value is the best that has ever been reported. A ϕ-scan through the {200} reflection of the TiN film is also shown in the figure. Although peaks occur every 60°, the film can be considered to be essentially a single crystallographic domain since there is such a large difference between successive peak intensities. The largest peaks occur every 120° and overlap those of the Si substrate which indicates excellent in-plane registry. The mosaic spread in the ϕ-scan for films grown with a 2.6 μs TOF was around 0.43°, 1.0° for a 2.0 μs TOF, and 0.62° for 3.3 μs and 3.7μs TOFs. The in-plane orientation relationships between all the TiN films and the underlying Si substrates were TiN[200] || Si[200] and TiN[111] || Si[111].

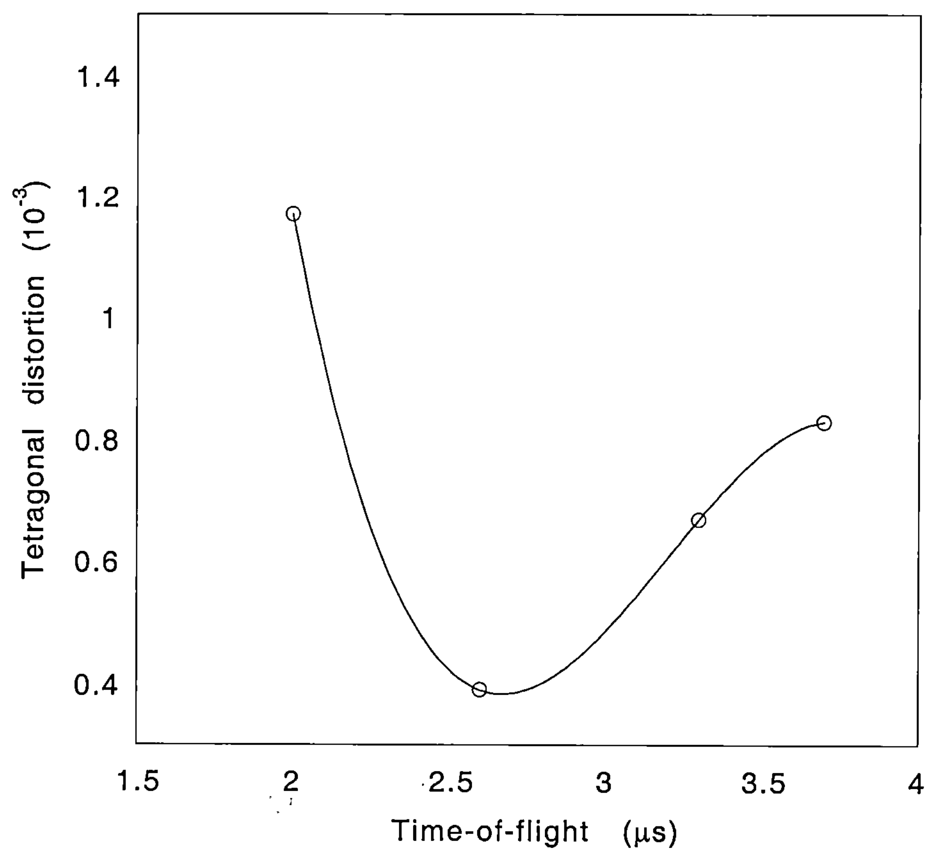

Figure 5.10. Dependence of tetragonal distortion on different times-of-flight (TOFs).

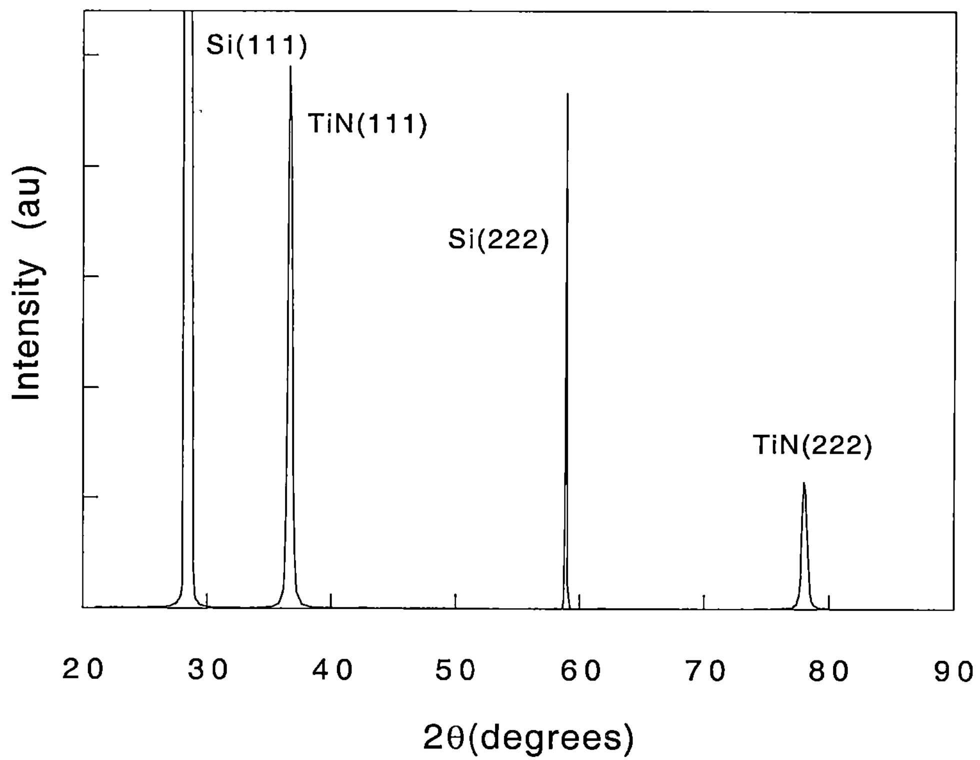

Figure 5.11. X-ray θ-2θ diffraction pattern for TiN grown with a 2.6 μs TOF.

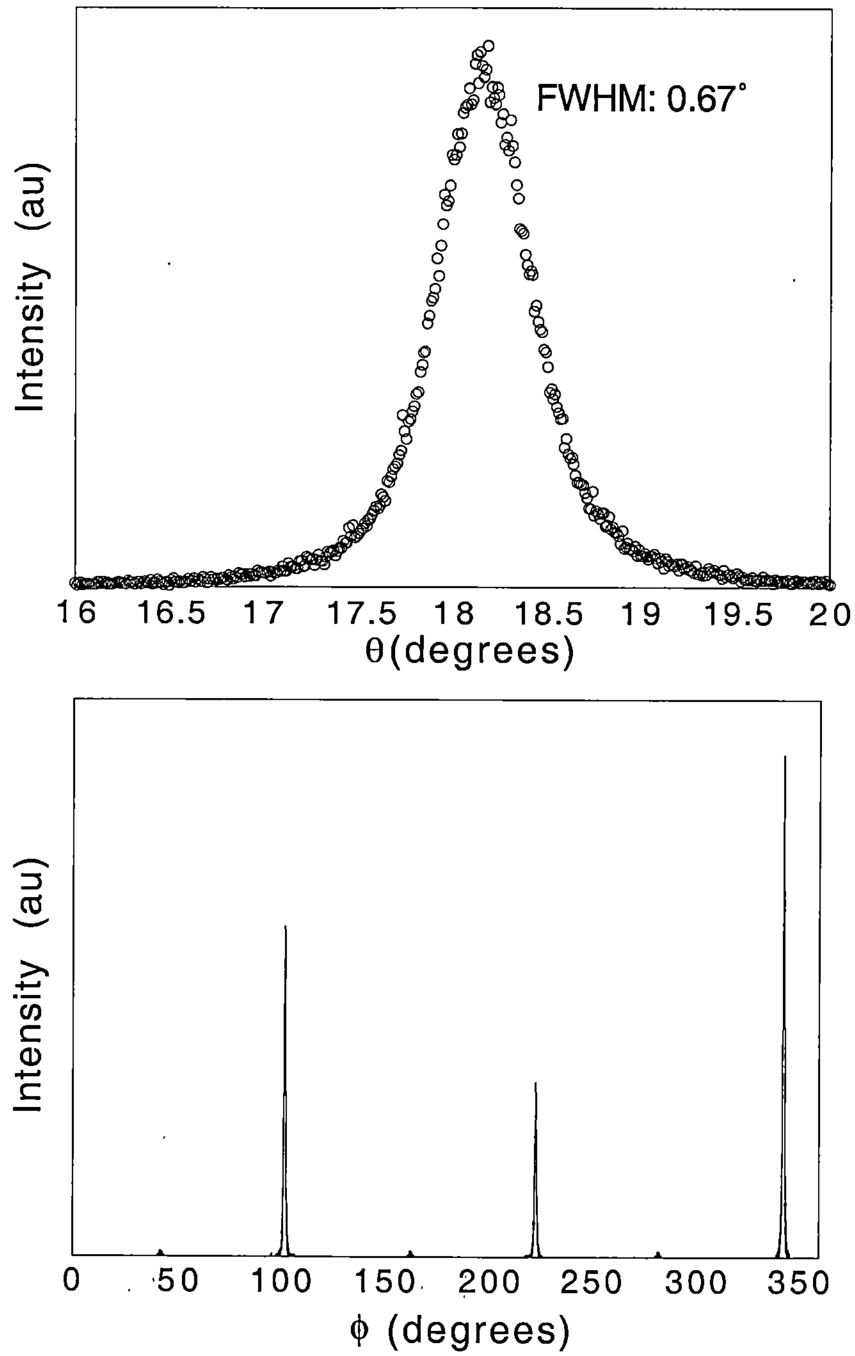

Figure 5.12. X-ray rocking curve and phi-scan of TiN film grown with (a) a 2.0 μs TOF.

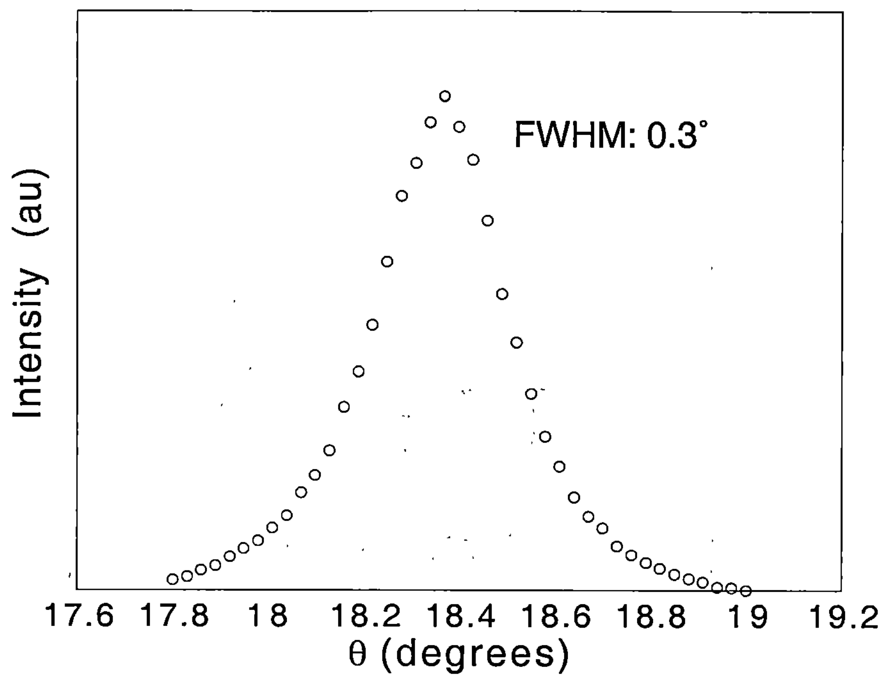

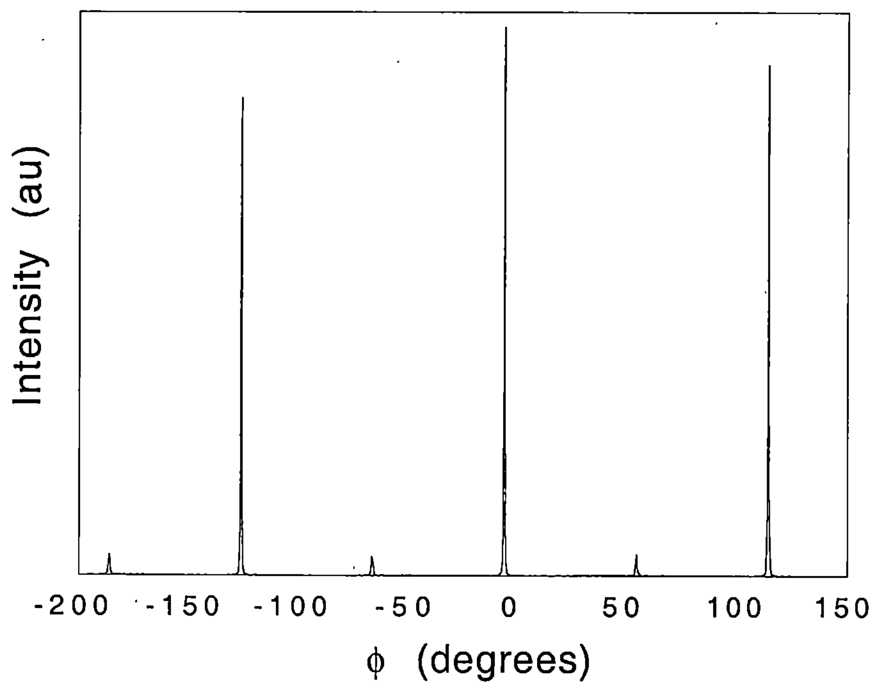

Figure 5.12. (continued) (b) a 2.6 μs TOF.

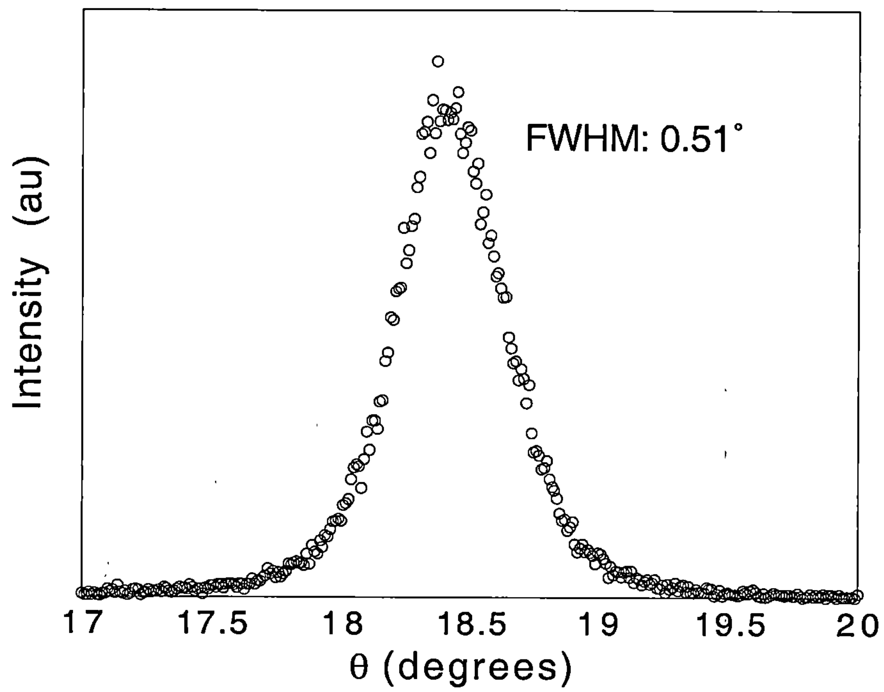

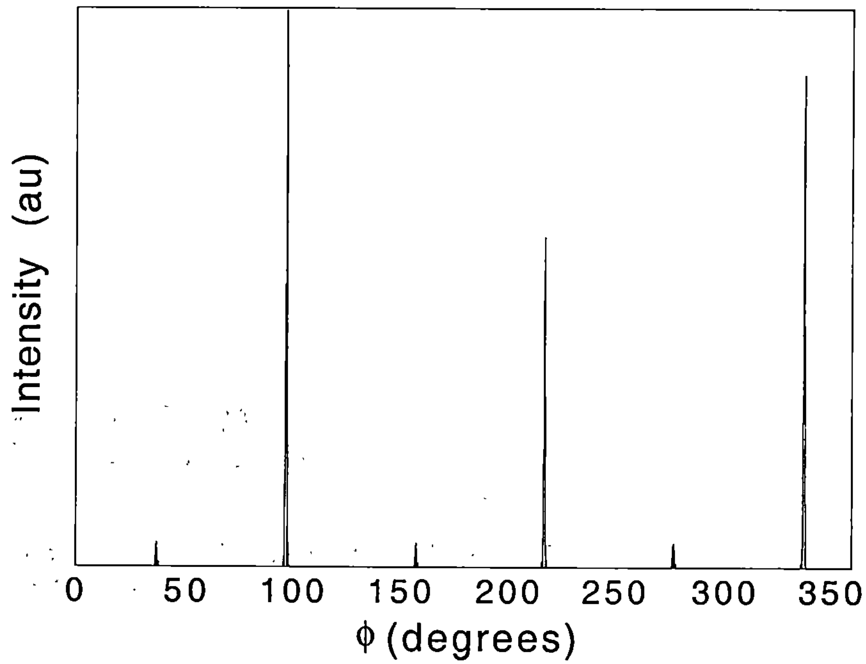

Figure 5.12. (continued) (c) a 3.3 μs TOF.

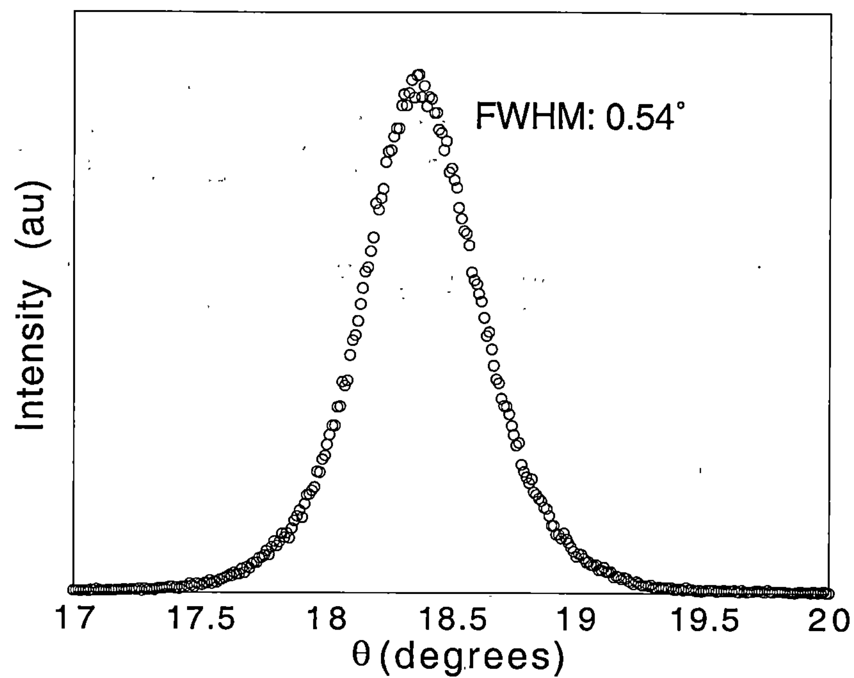

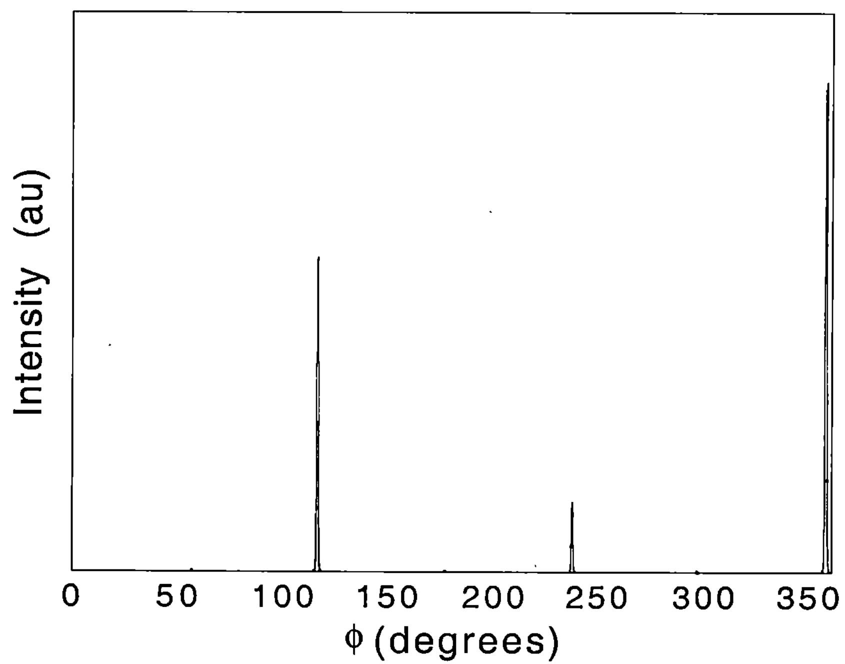

Figure 5.12. (continued) (d) a 3.7 μs TOF.

5.6.2. Dependence of film quality on kinetic energy of the ablated plume

The dependence of the FWHM of the X-ray rocking curve and phi-scan on ablation plume kinetic energy (i.e., the Ti vacuum TOF) was investigated and is shown in Fig. 5.13. It was found that the FWHM of the rocking curve and of the phi-scan decreased as the TOF increased from 2.0 μs to 2.6 μs, and then both increased again as the TOF increased from 2.6 μs to 3.7 μs. However, this trend did not result from the plume "missing" the gas pulse as the vacuum TOF was varied. As shown and discussed previously, maximum overlap conditions were largely independent of the energy imparted to the plume (i.e., vacuum TOF), mainly because the TOF is so much shorter than the laser pulse delay. However, the *effect* of the gas pulse on the plume varied strongly with vacuum TOF, as shown by the increasing curvature as vacuum TOF increases (see figure 5.3).

5.7. Surface Morphology Analysis

Atomic force microscopy (AFM) and scanning electron microscopy (SEM) were employed to study the surface morphologies of the TiN films. The root mean square (RMS) surface roughnesses over a 10 μm × 10 μm area were 38 Å, 30 Å, 45 Å, and 35 Å for films grown at 750 °C with 2.0 μs, 2.6 μs, 3.3 μs, and 3.7 μs TOF, respectively. The overall surface morphologies are shown in Figs. 5.14 (a)-(d). Films grown with an optimum TOF (2.6 μs) showed the smoothest surface morphology as compared to films grown with other TOFs.

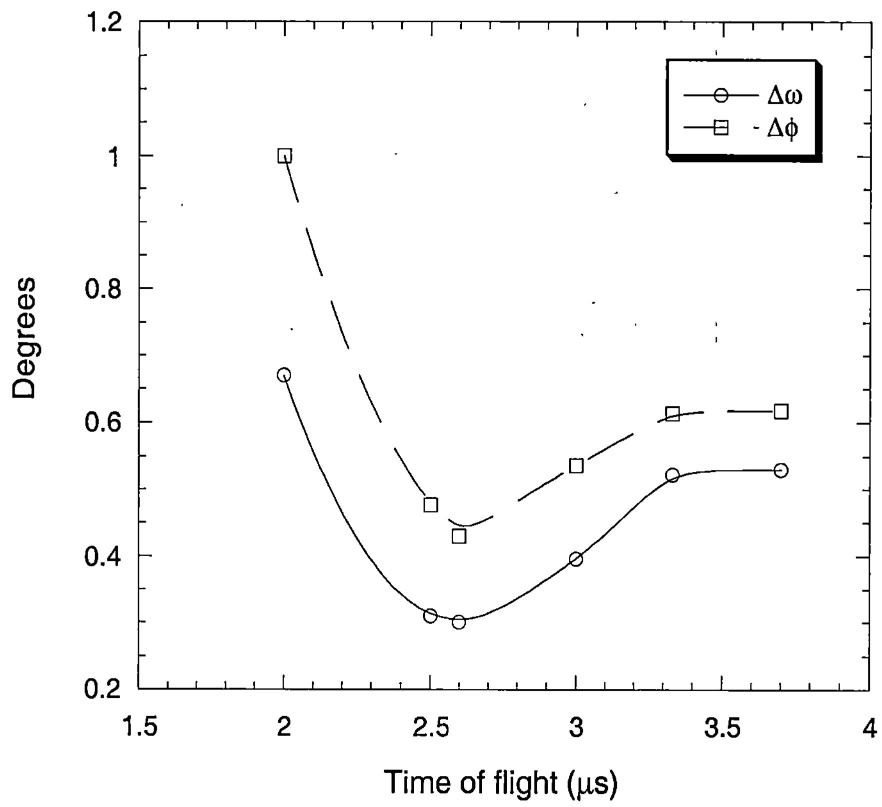

Figure 5.13. TOF-dependence of rocking curve and mosaic spread.

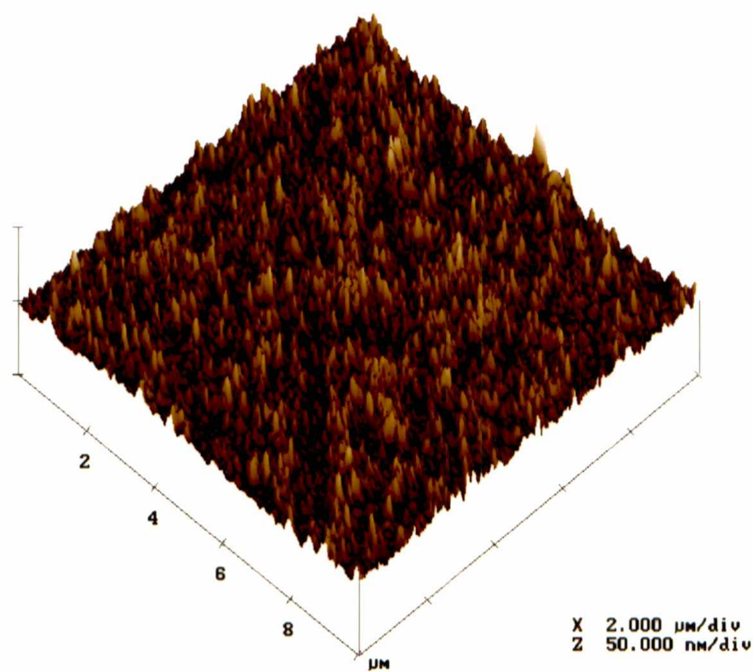

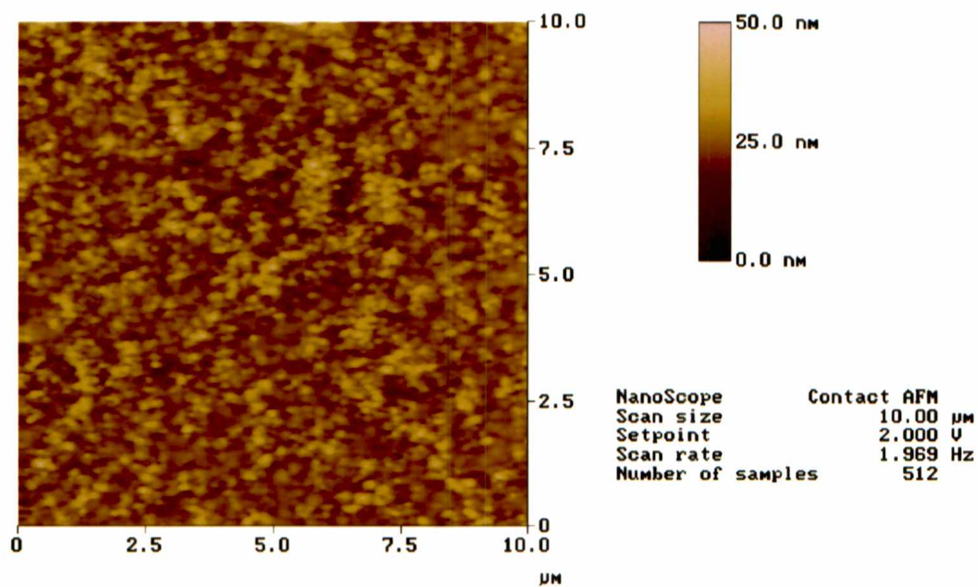

Figure 5.14. AFM images of a TiN film grown at T=750 °C. (a) with a 2.0 μs TOF.

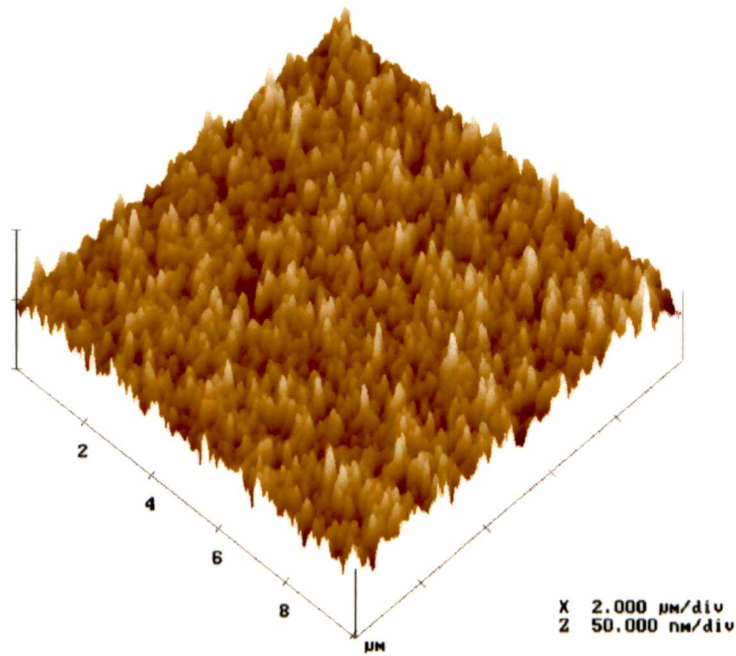

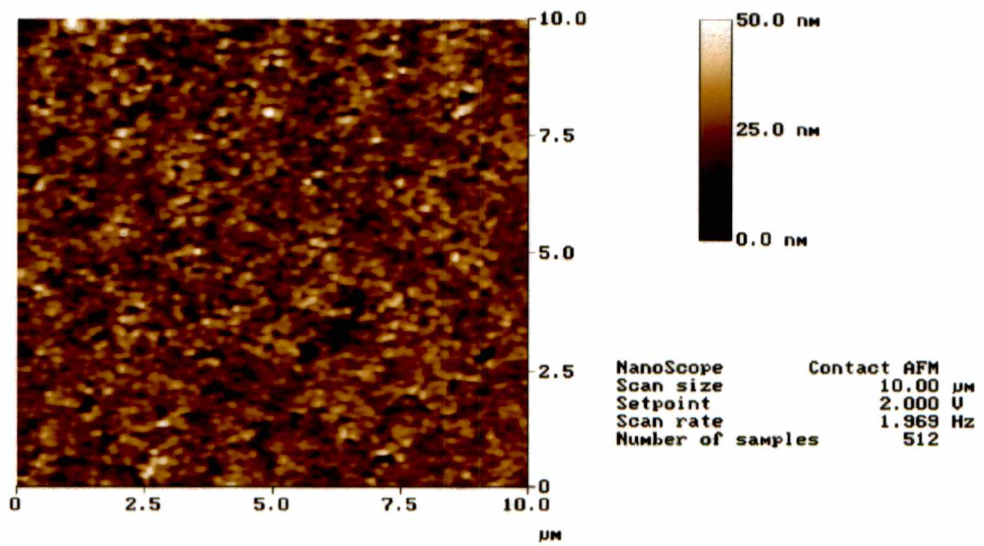

Figure 5.14. (continued) (b) with a 2.6 μs TOF.

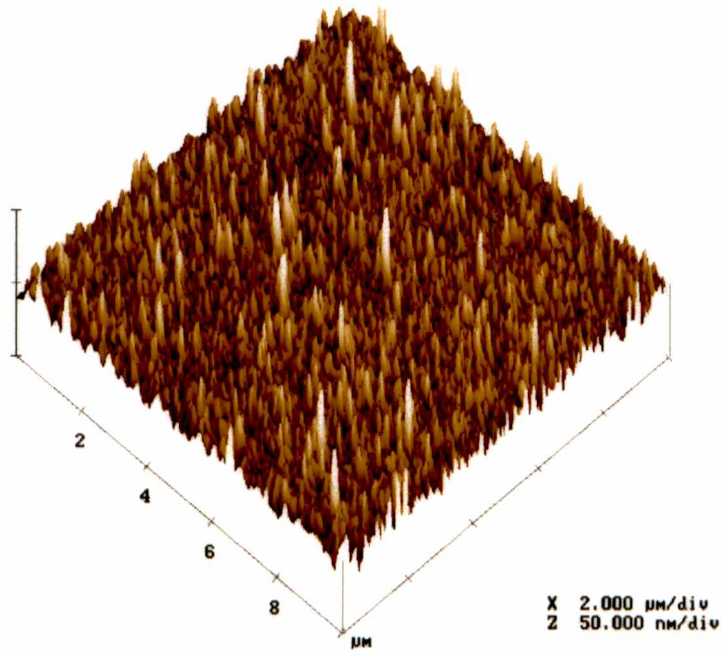

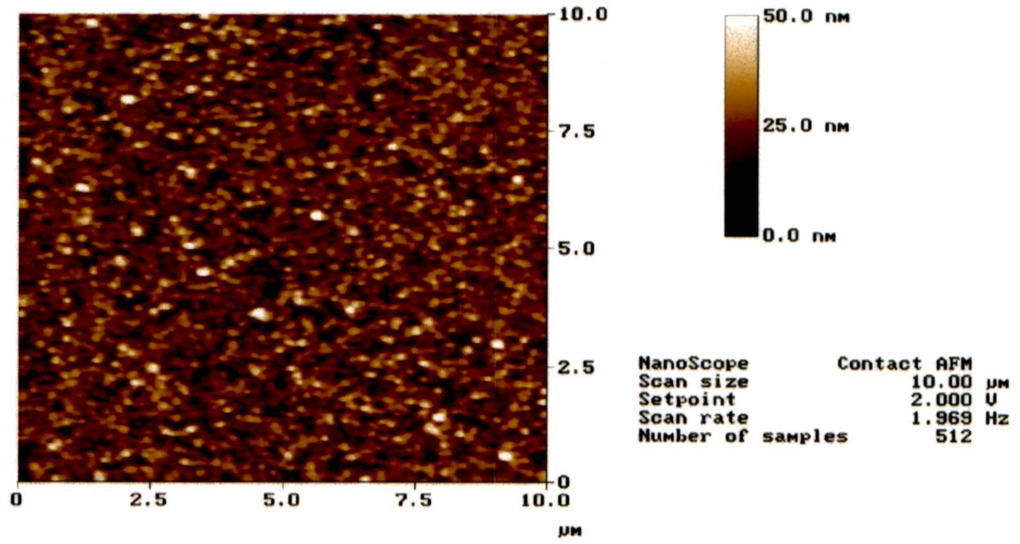

Figure 5.14. (continued) (c) with a 3.3 μs TOF.

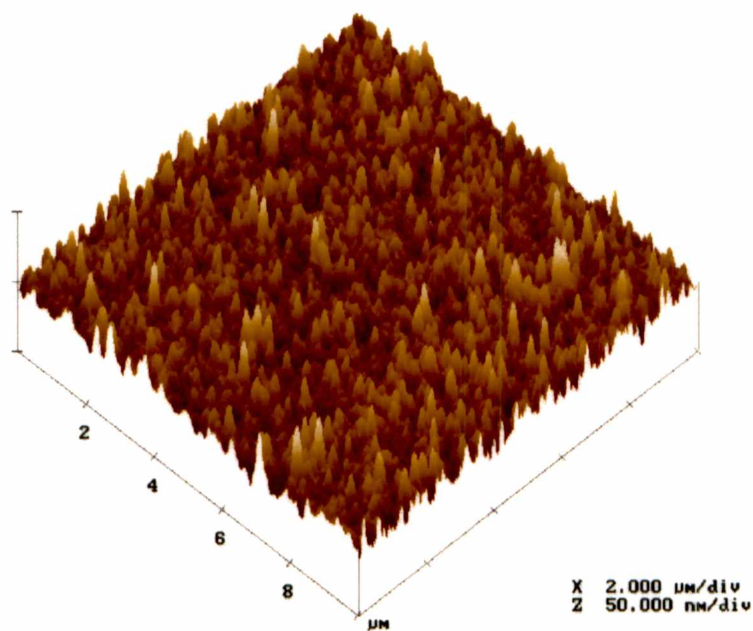

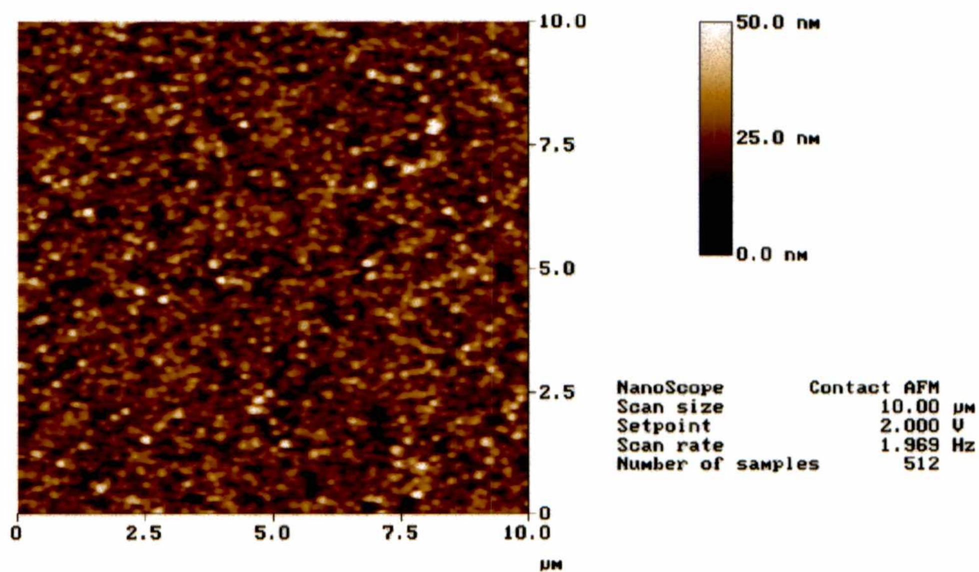

Figure 5.14. (continued) (d) with a 3.7 μs TOF.

The TiN thin films grown on Si(111) with TOFs ranging from 2.0 to 2.5 μs exhibit smooth surfaces except for the presence of some cracks and small round particles. Fig. 5.15 is a SEM micrograph of a TiN film grown at 750 °C with a 2.0 μs TOF showing the cracks and small particles. The cracks and particulates most likely resulted from the high energy density (short TOF) employed for this film – cracks possibly resulting from the high residual stress caused by the energetic species impinging on the growing film, and particulates possibly resulting from hot molten droplets ejected from the target. Cracks also are favored due to the small difference in thermal expansion coefficients between TiN and Si (α[TiN]=4.7×10^{-6} K^{-1}, α[Si]=3.6×10^{-6} K^{-1}). *Ex situ* examination of the Ti target surface showed deep cone-shaped craters after only 5,000 laser shots which supports the idea that massive amounts of material are ejected for this TOF. Van de Riet et al.[93] suggested that droplet production arises primarily from the periphery of the ablation crater. Even with target rotation, target surface roughening was accelerated by long-term exposure to laser irradiation. Therefore, frequent target refreshment by mechanical machining and polishing is required to minimize macroscopic droplet ejection. Target morphologies for each TOF (i.e. for each of the different laser energy densities focused on the target) after 5,000 ablation pulses are shown in Fig. 5.16 (a)-(e). It is well known that the formation of a "race track" with microstructural cone-shaped features is a nearly universal response of the target to repetitive laser exposure in a specific fluence range.[82] However, at lower TOFs (3.7 μs) these tracks exhibited ripples and smoothing which also are commensurate with low-fluence laser irradiation

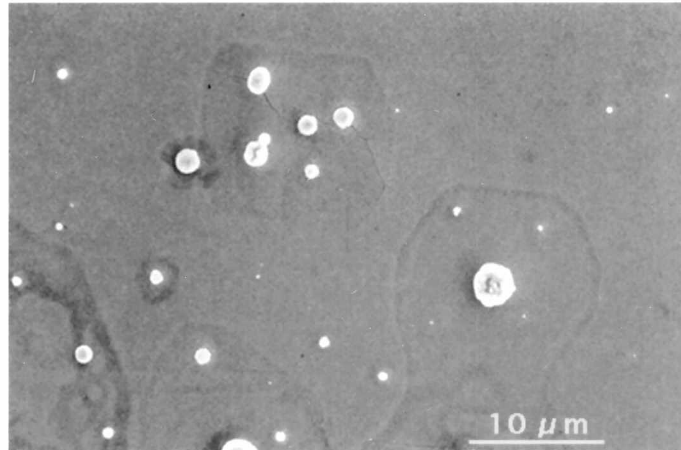

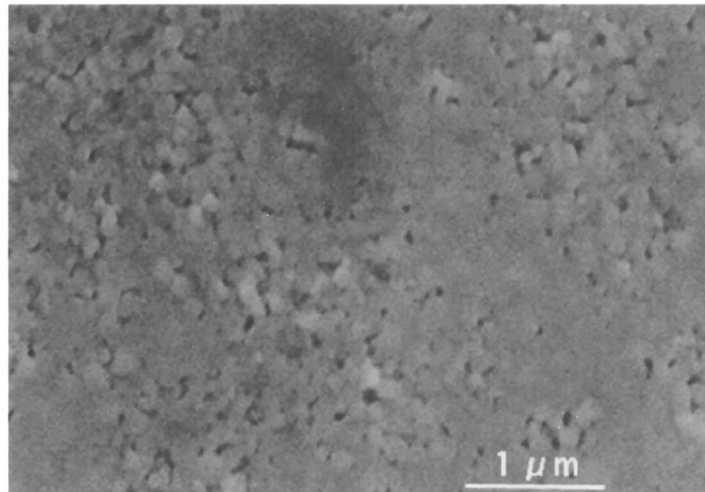

Figure 5.15. SEM micrograph of a TiN film grown at 750 °C with a 2.0 μs TOF.

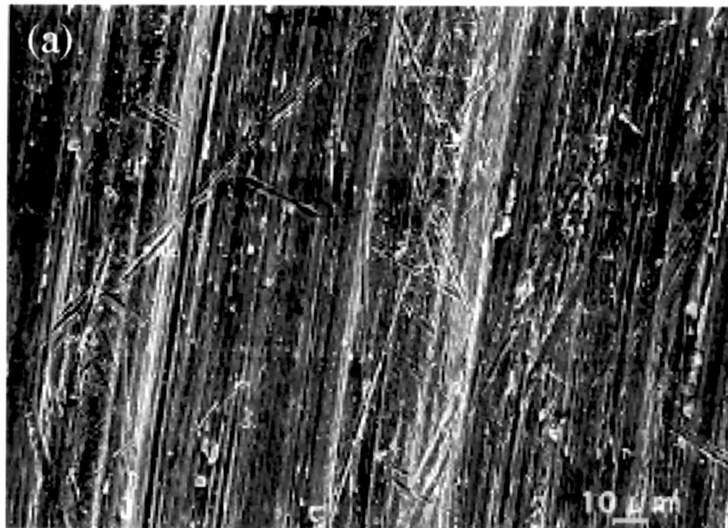

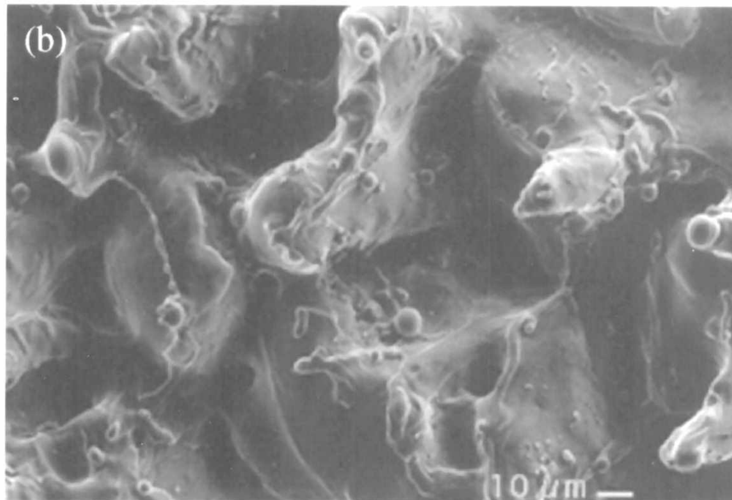

Figure 5.16. Target morphology for (a) bare target and (b) 2.0 μs TOF (the corresponding laser energy density on the target was 4.11 J/cm^2).

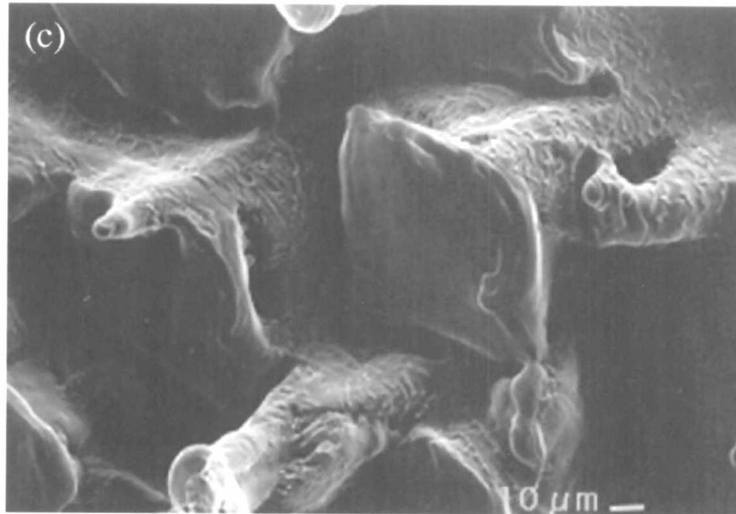

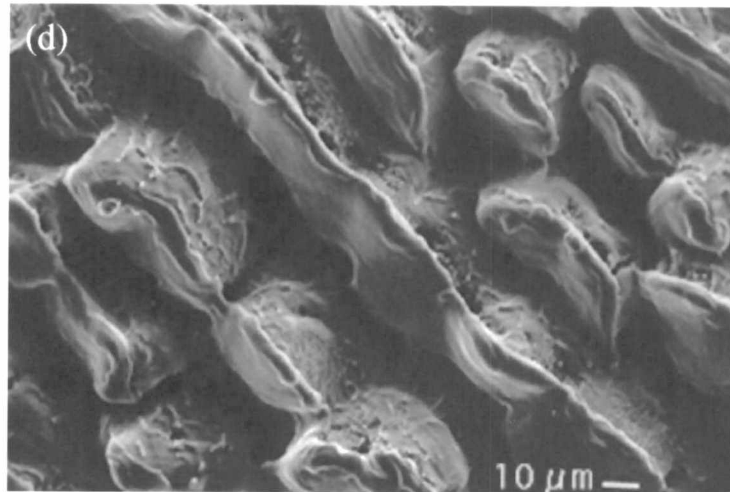

Figure 5.16 (continued) (c) with a 2.6 μs TOF (2.86 J/cm^2),

(d) with a 3.3 μs TOF (2.16 J/cm^2).

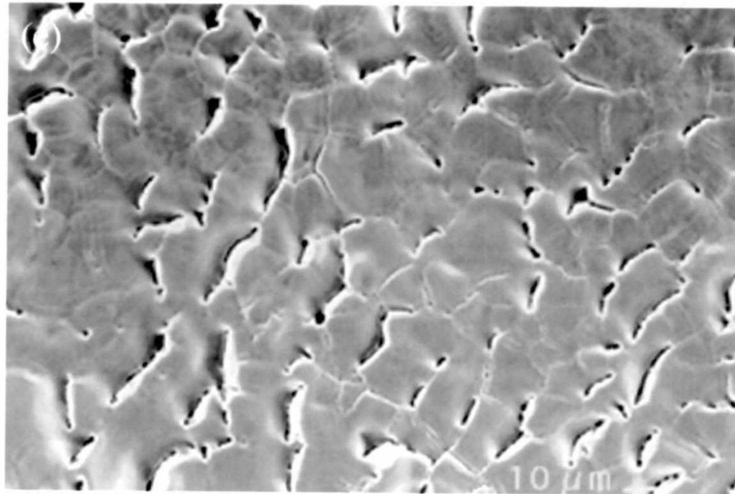

Figure 5.16. (continued) (e) with a 3.7 μs TOF (1.74 J/cm^2).

closer to the threshold for near-surface melting.

Young et al.[94] have shown in detail the role of laser fluence in producing different types of surface morphologies using a Ge target. However, there still is no comprehensive model to describe the complex interaction leading to laser-induced cone formation, though quite extensive studies have been done for Si.[95]

In contrast to the smooth, cracked and decorated TiN film surfaces obtained at short TOFs (Fig. 5.15), Fig. 5.17 shows a SEM micrograph of a TiN film grown at 750 °C with a 2.6 μs vacuum TOF (E_K=91.7 eV), the value considered to be optimal. When also contrasted with a film grown at a larger vacuum TOF, Figs. 5.18 and 5.19, the optimal film's morphology clearly shows a mixed nature that might result from the following: For some fixed temperature and at short vacuum TOFs, the energy-dependent gas pulse collision cross-section is too small and the impinging growth-species are left too energetic to allow complete long- range order to develop and highly stressed, somewhat disordered films result. Conversely, at sufficiently long vacuum TOFs the energy-dependent gas pulse collision cross-section is much larger and extreme collisional-slowing and/or condensation of the plume might occur leading to a granular, faceted microstructure that is essentially uniform as shown in Fig. 5.18, because too few energetic species are present to erode the grains or to provide sufficient mobility to planarize the surface at this temperature. Thus, at some intermediate TOF and temperature the energetics are favorable to balance the forces favoring film damage and erosion against those favoring highly three-dimensional growth. However, we note that

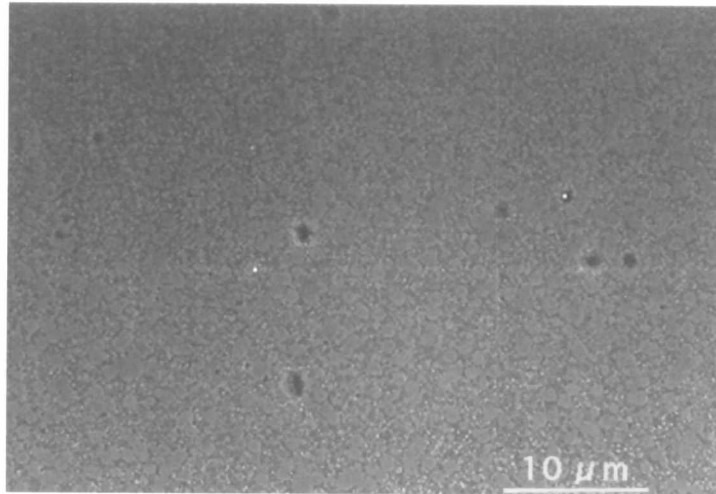

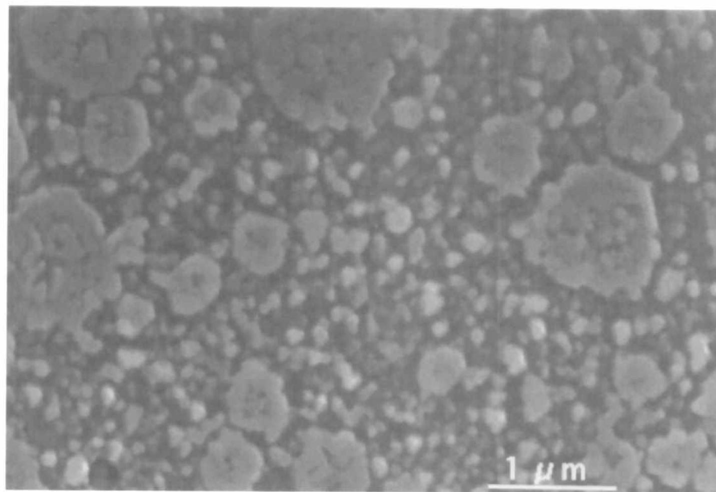

Figure 5.17. SEM micrograph of a TiN film grown at 750 °C with a 2.6 μs TOF.

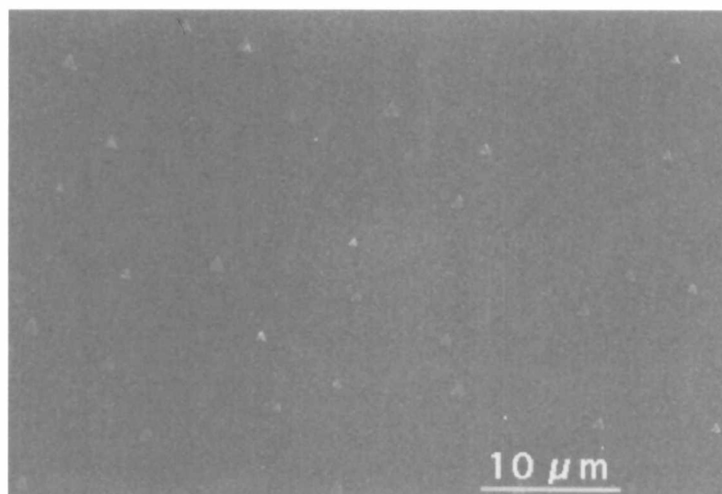

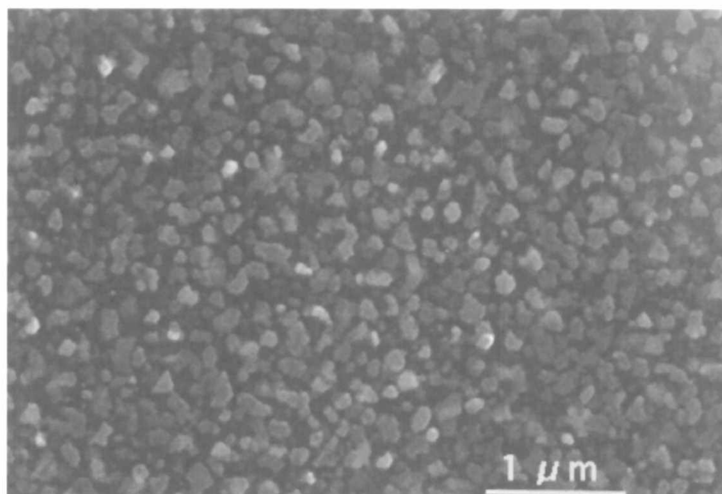

Figure 5.18. SEM micrograph of a TiN film grown at 750 °C with a 3.3 μs TOF.

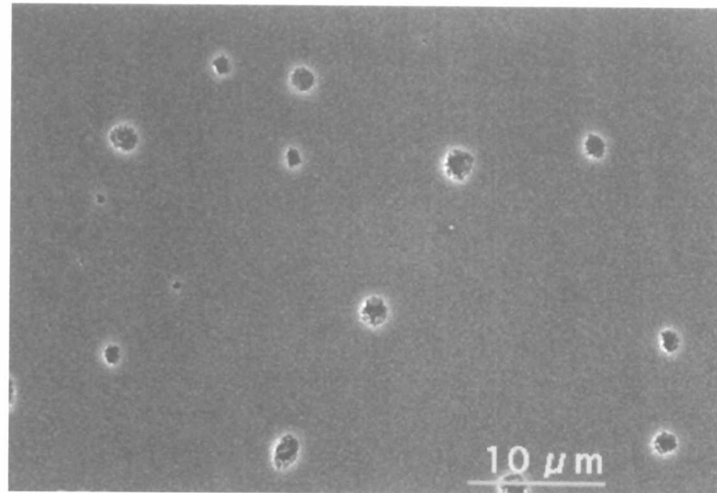

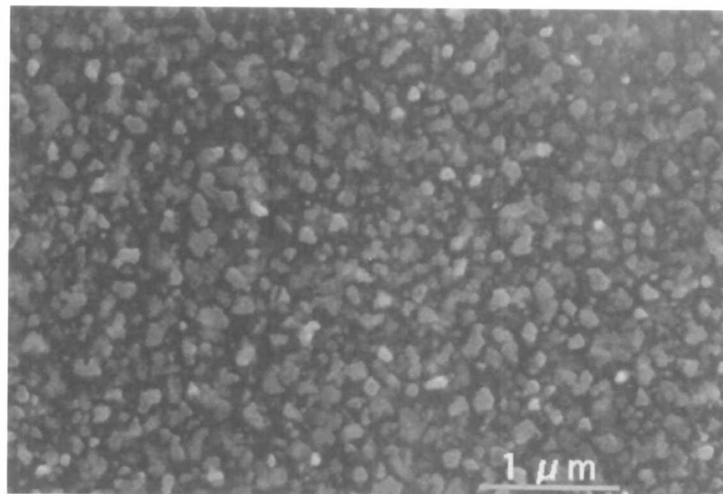

Figure 5.19. SEM micrograph of a TiN film grown at 750 °C with a 3.7 μs TOF.

the ablation plume's kinetic energy distribution is broad and even when the most probable kinetic energy is tuned to the optimal value (~92 eV), the incident flux contains Ti atoms/ions with both higher and lower kinetic energies, rendering the optimal films still imperfect.

5.8. Epitaxial Growth in a Large-Lattice-Mismatch System

In addition to X-ray diffraction, conventional cross-section transmission electron microscopy (TEM), high-resolution transmission electron diffraction (HR-TEM), and high-resolution scanning transmission electron microscopy (STEM) were employed to study the TiN/Si interface and its effect on the subsequent microstructure and epitaxial relationships of the TiN films.

Even in a large-lattice mismatch system (TiN/Si: 22.3 %), epitaxial growth can be observed. This can be described in terms of domain-matching epitaxy.[96] In each domain, m lattice parameters in the epilayer match with n in the substrate. The dimensions of domains are repeated so that domain matching is maintained. A schematic illustration of domain matching epitaxial growth in a large-lattice mismatch system is shown in Fig. 5.20.

In general, a domain of length ma of the epilayer does not match perfectly with the domain length nb of the substrate so that a residual domain mismatch strain is present in the x and y directions. However, the resulting domain-mismatch strain is much smaller than the lattice-mismatch strain, and the implications of this will be discussed later for

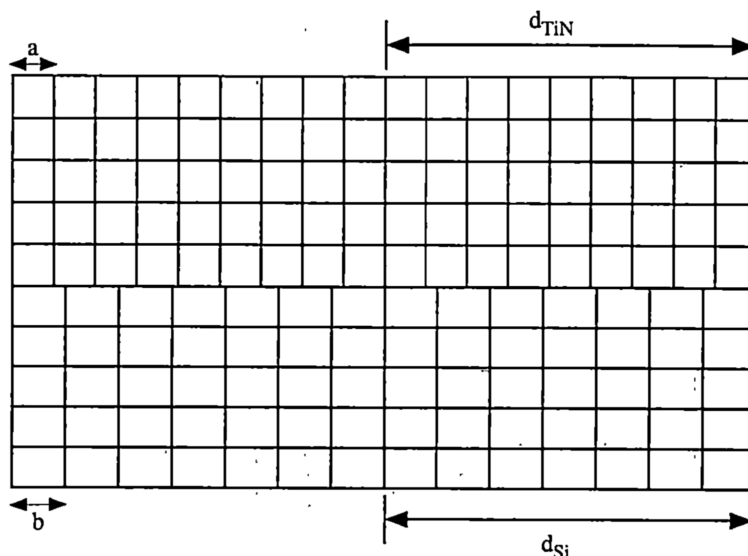

Figure 5.20. Schematic illustration of domain-matching epitaxial growth in a large-lattice mismatch system.

TiN/Si. This decrease in strain is primarily responsible for domain-matching epitaxial growth being energetically favored.

A TEM sample for cross-sectional viewing was prepared by ion milling at liquid nitrogen temperature after mechanical dimpling and polishing. The sample was ion milled at 18° until a hole developed in the sample and then the angle was reduced to 12° to lengthen the wedge-shaped region. An angle of 18° was used once again for a few minutes to finish the milling procedure. A VG Microscope HB501 Dedicated STEM/EELS was used for high resolution imaging while a Phillips 400 was used for electron diffraction patterns. Cross-sectional viewing was performed on a high-resolution TEM (HR-TEM, Philips-Fetecnai F30-UT). The selected area electron diffraction

(SAED) pattern and indexed pattern from the interface area are shown in Fig. 5.21 (a) and (b), respectively. TiN and Si diffraction spots were aligned with respect to each other. From the SAED pattern taken along [110], it is found that [002]TiN is parallel to [002]Si , $[2\underline{2}0]$TiN is parallel to $[2\underline{2}0]$Si, and $[1\underline{1}1]$TiN is parallel to $[1\underline{1}1]$ Si. Alignment of diffraction spots indicates cube-on-cube epitaxial orientation between the TiN layer and the Si substrate, i.e. <001>TiN || <001>Si and <111>TiN || <111>Si and these relationships are maintained during the growth.

The cross-sectional high-resolution TEM image from the interface area is shown in Fig. 5.22. Columnar structures have been commonly observed in compounds of high binding energy such as TiN, TiC, PbS, and CaF_2.[97] A columnar microstructure consists of a network of low density material surrounding an array of parallel rod-shaped columns of high density.[82] A columnar microstructure is not desirable for electrical transport in semiconductor technology because this type of microstructure strongly modulates the optical, mechanical, magnetic, and surface properties of grown films. However, as shown in the present TEM figures, a columnar microstructure was not observed on the very short length scale accessible to HR-TEM. The interface is very sharp, complying with device fabrication requirements, and there is no perceptible interdiffusion between the TiN film and the Si substrate. A HR-TEM micrograph showed both the {111} planes in the TiN and in the Si substrate with clarity and therefore indicated epitaxial growth. Furthermore, there are no voids between the film and the substrate, indicating good adhesion at the atomic level. It is interesting to note that TiN films grown by a variety of

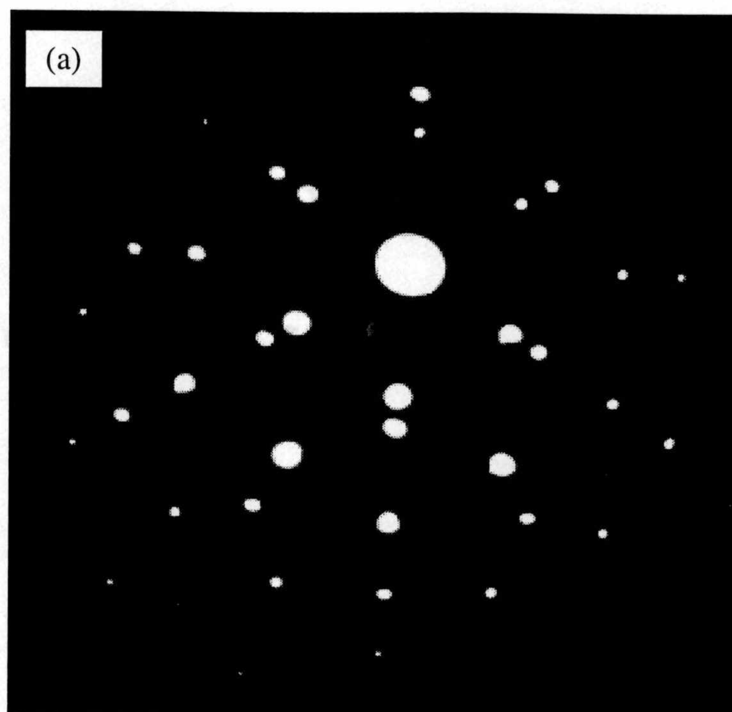

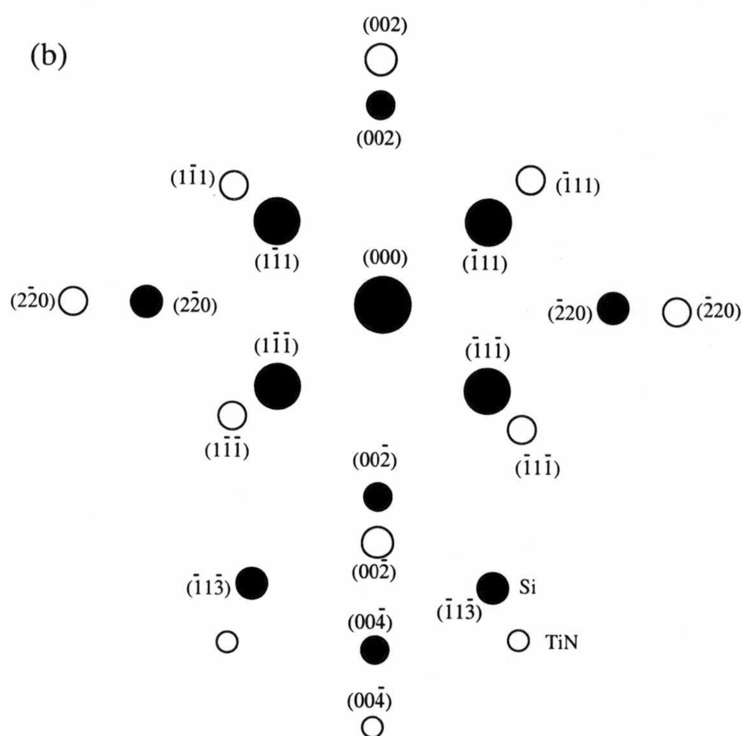

Figure 5.21. Electron diffraction pattern from TiN/Si interface. (a) SAED pattern and (b) corresponding indexed pattern (TiN: open circles, Si: solid circles).

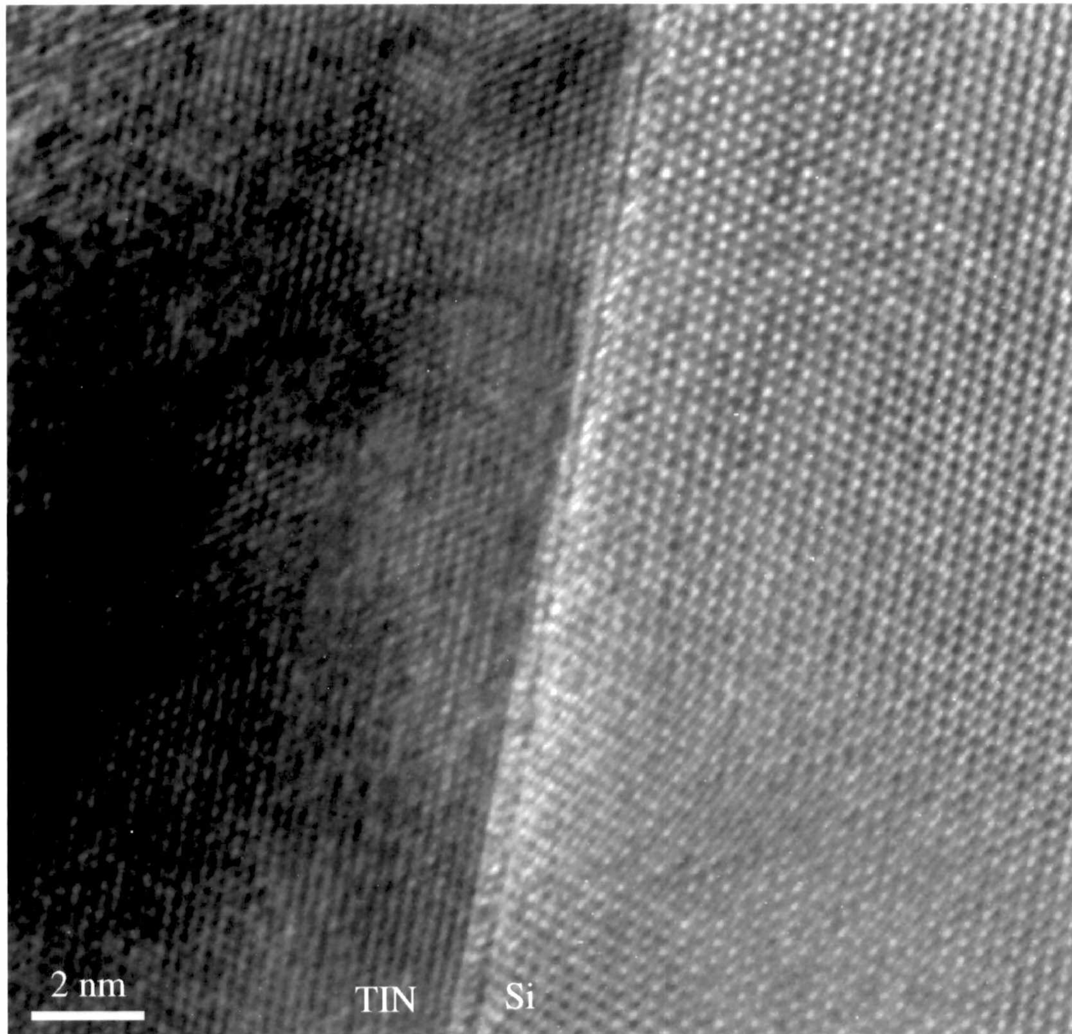

Figure 5.22. High-resolution cross-sectional TEM lattice image from TiN/Si, viewed along [110].

other methods typically show oxide layers at the interface.[25, 98] In this study no oxide layer was noted between the TiN film and the Si substrate. This observation was confirmed by RHEED, Z-contrast STEM, and EELS. From the diffraction pattern and HR-TEM image, it was determined that 9 unit cells of TiN were coincident on 7 units cells of Si. This fact was confirmed by Z-contrast imaging.

In two-dimensional epitaxial growth, the *lattice*-mismatch strain is defined by [96]

$$\varepsilon_x = \frac{2(a_x - b_x)}{(a_x + b_x)} \qquad (5.17)$$

$$\varepsilon_y = \frac{2(a_y - b_y)}{(a_y + b_y)} \qquad (5.18)$$

where a_x and a_y are the lattice parameters of the epilayer and b_x and b_y those of the substrate along the x and y direction, respectively. Also, the *domain*-mismatch strain in a domain-matching growth system is given by[96]

$$\varepsilon_{dx} = \frac{2(ma_x - nb_x)}{(ma_x + nb_x)} \qquad (5.19)$$

$$\varepsilon_{dy} = \frac{2(ua_y - vb_y)}{(ua_y + vb_y)} \qquad (5.20)$$

where m, n, u, and v are integers.

Using the equations above and x-ray data, the calculated lattice-mismatch strains ε_x and ε_y for a film grown at 2.6 μs TOF were found to both equal 0.245. However, this value is much too large so that lattice-matched epitaxial growth is not expected to actually occur. On the other hand, domain-matched epitaxial growth with m=9 interplanar spacings of

TiN matching n=7 of Si is favorable because the resulting domain-mismatch strain is only $\varepsilon_{dx} = \varepsilon_{dy} = 0.00463$.

Unlike conventional TEM images whose contrast depends on specimen thickness and focus, the interpretation of Z-contrast images is intuitive.[99,100] The images can be often considered as a convolution of objective function and probe intensity profile, and the intensity of each atomic column is proportional to the square of atomic number, Z, when the inner angle of the annular dark field detector is sufficiently large.[101]

Fig. 5.23(a) and (b) show a high-resolution bright-field STEM image and a Z-contrast dark-field image. Nitrogen atoms are not seen in the Z-contrast image because of their small scattering cross section, and the nearest Ti-Ti distance in the [110] zone axis is 2.998 Å, which is resolved in the image. Silicon dumb-bells are not resolved due to the instrument resolution. As shown in the schematics in Fig. 5.24, there are two possible TiN terminations, one a Ti row, the other a N row. The Z-contrast image shows that the interface was made by joining Si and N atoms, not Ti, judging from the bond lengths of the atomic arrangements, and the fact that Si_3N_4 exists.

Fig. 5.25 shows the line-scanned EELS as the line crossed TiN/Si interface. There are no oxygen peaks, indicating that there is no SiO_2 at the interface. The peaks on the left (> 360) are due to Si background signals and the peaks in the center are due to Ti. Oxygen, if present, would have appeared near 530 eV.

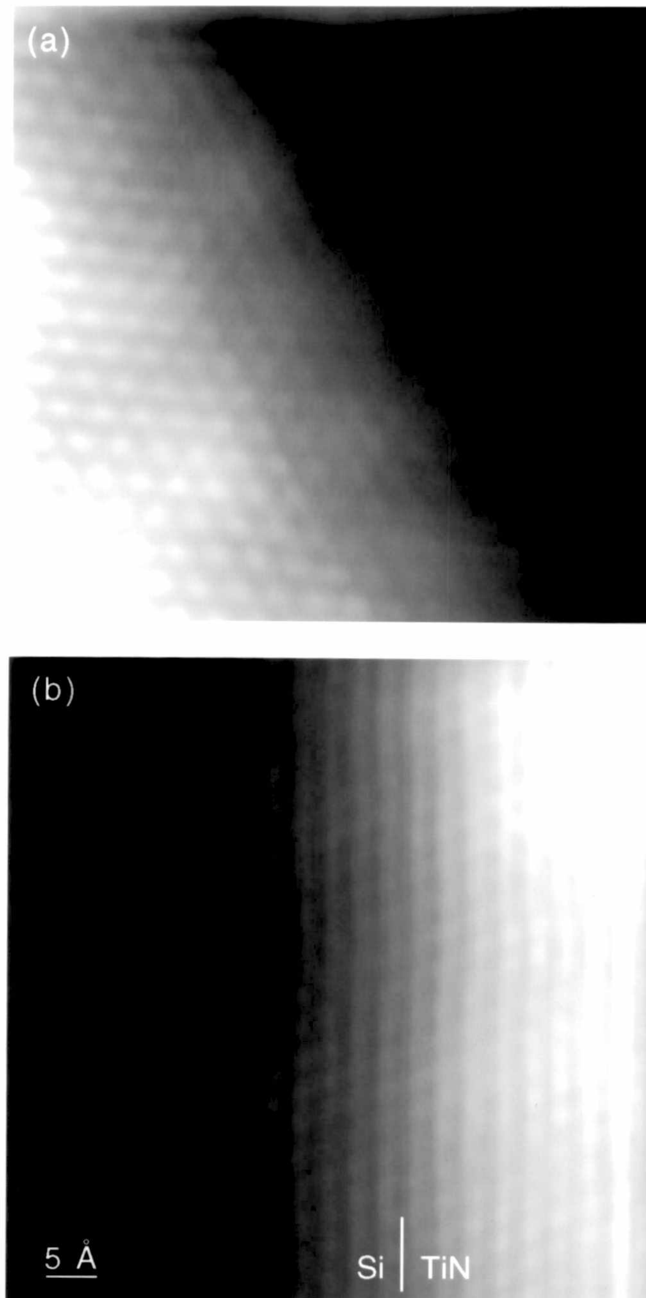

Figure 5.23. STEM images of TiN/Si along [110]. (a) bright-field and (b) Z-contrast dark-field.

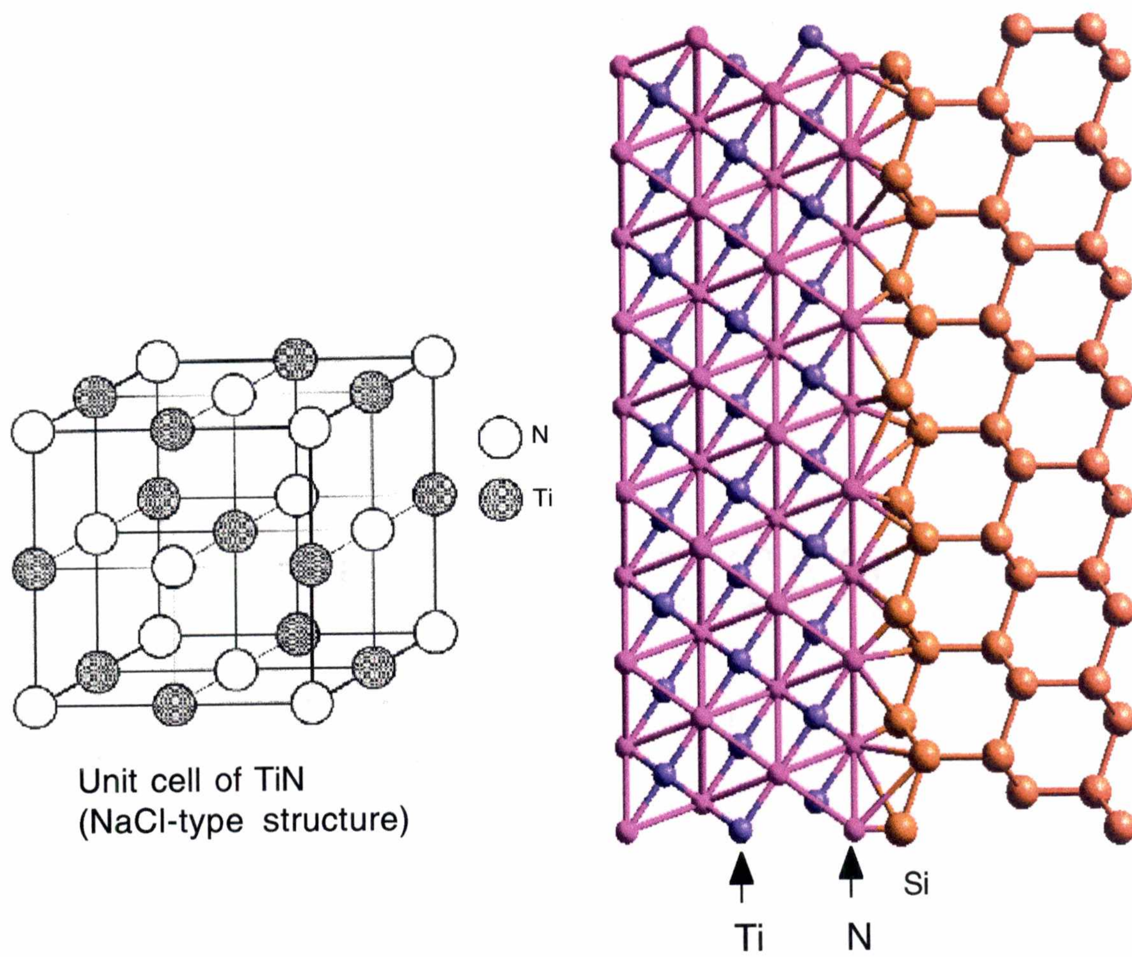

Figure 5.24. Schematic drawing of unit cell of TiN and bonding between TiN and Si substrate.

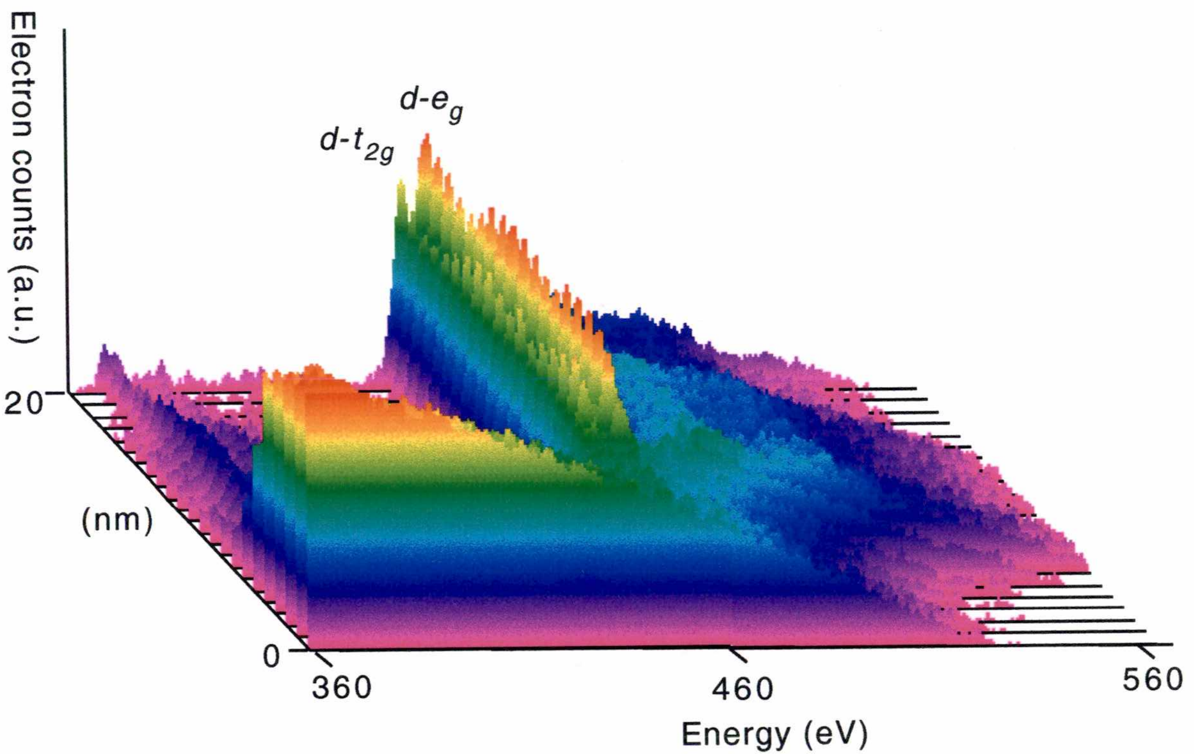

Figure 5.25. EELS spectra as the scan line crossed the TiN/Si interface. Ti-*d* edges, $d\text{-}t_{2g}$ and $d\text{-}e_g$, were shown.

5.9. Theoretical Calculations

X-ray diffraction data (lattice constant measurement) and the electron energy loss spectra (EELS) of titanium are compared in this section with *ab-initio* calculations. Since the cross section of electron-loss near-edge structure (ELNES) is proportional to the unoccupied electronic density of states, a simulated density of states was compared with the experimental spectrum.[102] In principle, the quantum mechanical wavefunction contains all the information about a given system. In order to get the wavefunction of the system, one would have to solve the Schrödinger equation exactly and then determine the allowed energy states of the system. In the case of the quantum mechanical problem of solids, it is impossible to solve the Schrödinger equation exactly for a many-particle system with as many as 10^{23} coordinates (all the electrons and nuclei). Approximations are normally made to simplify the problem without losing too much information. The simplest definition of density functional theory is a method of obtaining an approximate solution to the Schödinger equation of a many-particle system. Density functional theory (DFT) is an accurate, *ab-initio* theory that has proved extremely powerful since its inception by Hohenberg and Kohn (1964)[103] and Kohn and Sham (1965).[104]

The density functional theory, implemented as the full potential linearized augmented plane wave (FLAPW) method[105], was used for the calculations. The FLAPW method is self-consistent, and calculates both core and valence electrons separately. The core electrons are approximated using a "muffin-tin" description[105], and inside the muffin-tin radius the combination of radial function and spherical harmonics are used to describe the potential and charge density, and planewaves are used for the interstitial

region. A commercial package, the WEIN97 codes[105], was used for a series of calculations.

In principle, DFT gives a good description of the ground state properties, but for a practical calculation, the exchange-correlation potential must be approximated as a functional of the density. The exchange-correlation potential describes the effects of the Coulomb potential and the Pauli principle beyond a purely electrostatic interaction of the electrons. For the approximations to the exchange-correlation term, the so-called LDA[106] (local density approximation) and GGA (generalized gradient approximation)[107] have long been standard choices. (In the LDA the corresponding exchange-correlation potential is a local potential, hence its name.) The LDA is derived from the homogeneous electron gas and is only valid for systems with slowly varying charge densities. While the local density approximation (LDA) has exchange-correlation energy depending only on the local electron density at a given point, the GGA includes gradient terms of the electron density and is expected to be more accurate for rapidly varying electron densities, e.g. *d*-electrons. It has been demonstrated that GGA gives a considerable improvement of the ground state properties of solids, molecules, and atomic systems over calculations based on LDA.[108]

The space group of TiN is Fm3m with a lattice constant of 4.242 Å. 781 points were used for radial meshes, a Bohr radius of 2.05 Å was used for Ti, and a Bohr radius of 1.95 Å was used for the muffin-tin radius. The kinetic energy cutoff that determines the number of planewaves in the expansion and the number of reciprocal lattice k points used for the Brillouin zone integration are increased until the result converges. The

energy cutoff for planewaves was 4.0 Rydberg and 400 reciprocal lattice K-points were used. Ti 3*d*, 4*s* and N 2*s*, 2*p* electrons are considered as valence charges. The self-consistent criterion was 0.01 % difference between the old charge and the calculated new charge.

First, we obtained the energetically optimized lattice constant theoretically using both the LDA and GGA approximations. These results are shown in Fig. 5.26 and Fig. 5.27. To predict the equilibrium lattice constant of a solid, a series of total-energy calculations are executed to determine the total energy as a function of the lattice constant. As shown in the figures, the theoretical value for the equilibrium lattice constant is the value of the lattice constant at the minimum of this curve.[109] The lattice constant obtained from the LDA is 4.189Å, which is 1.24 % smaller than the experimental value, while it is 4.258 Å, 0.35 % larger with the GGA. Considering that the typical error range of lattice constants using the density functional theory is ~1% (larger with the GGA, smaller with the LDA), these results turned out to be reliable and in good agreement with X-ray diffraction experimental data, also much better than the previous calculations by Ahuja et al.[108] However, it appears that the GGA describes the equilibrium structure of TiN better than the LDA.

The density of states (DOS) for TiN were obtained by means of the LDA and GGA. The calculated DOS were very similar for the two cases and are shown in Fig. 5. 28(a) and (b) for the LDA and in Fig. 5.29 (a) and (b) for the GGA. Ti has cubic site symmetry with doubly degenerate d-e_g states and triply degenerate d-t_{2g} states. As shown in the figure, the density of states shows a metallic state with a Fermi level in the valence

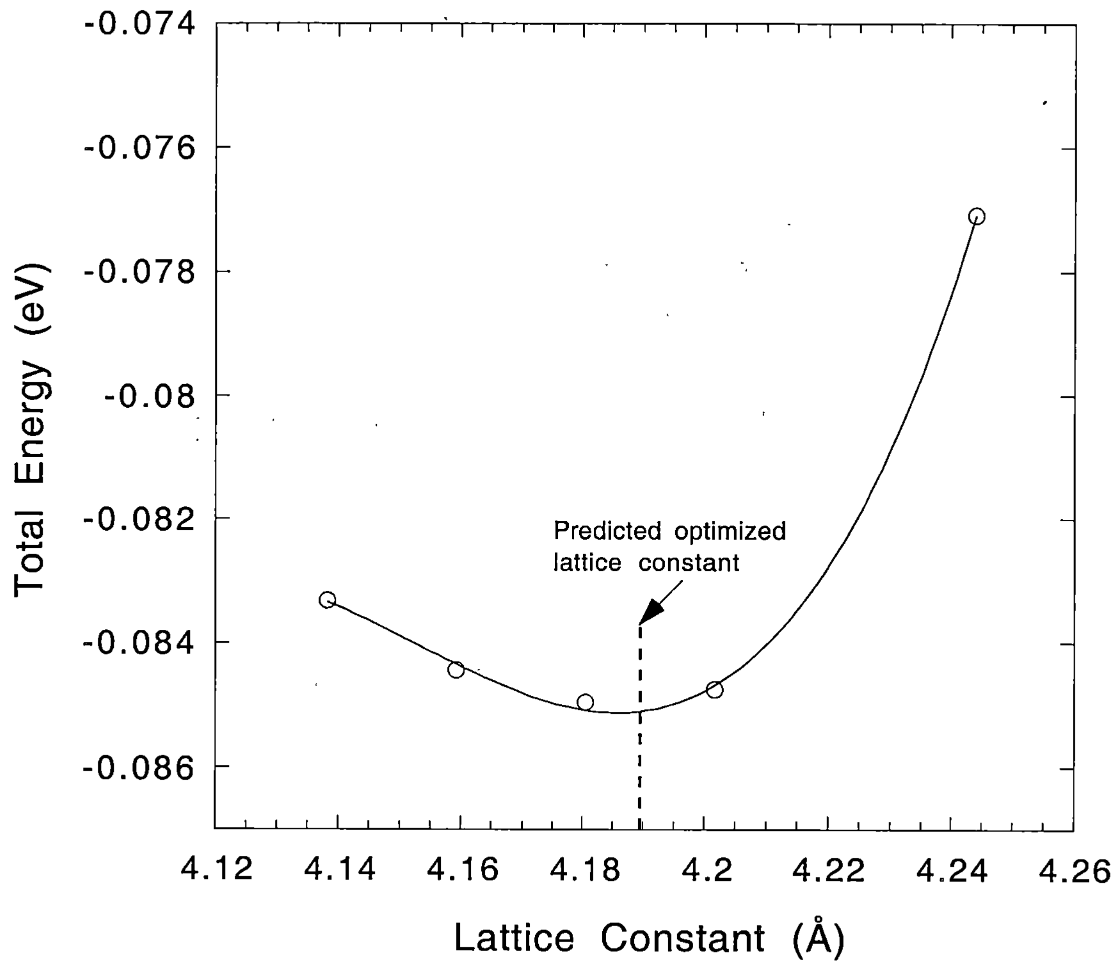

Figure 5.26. Theoretical determination of an equilibrium lattice constant by the LDA. The predicted lattice constant is determined by the minimum in the curve.

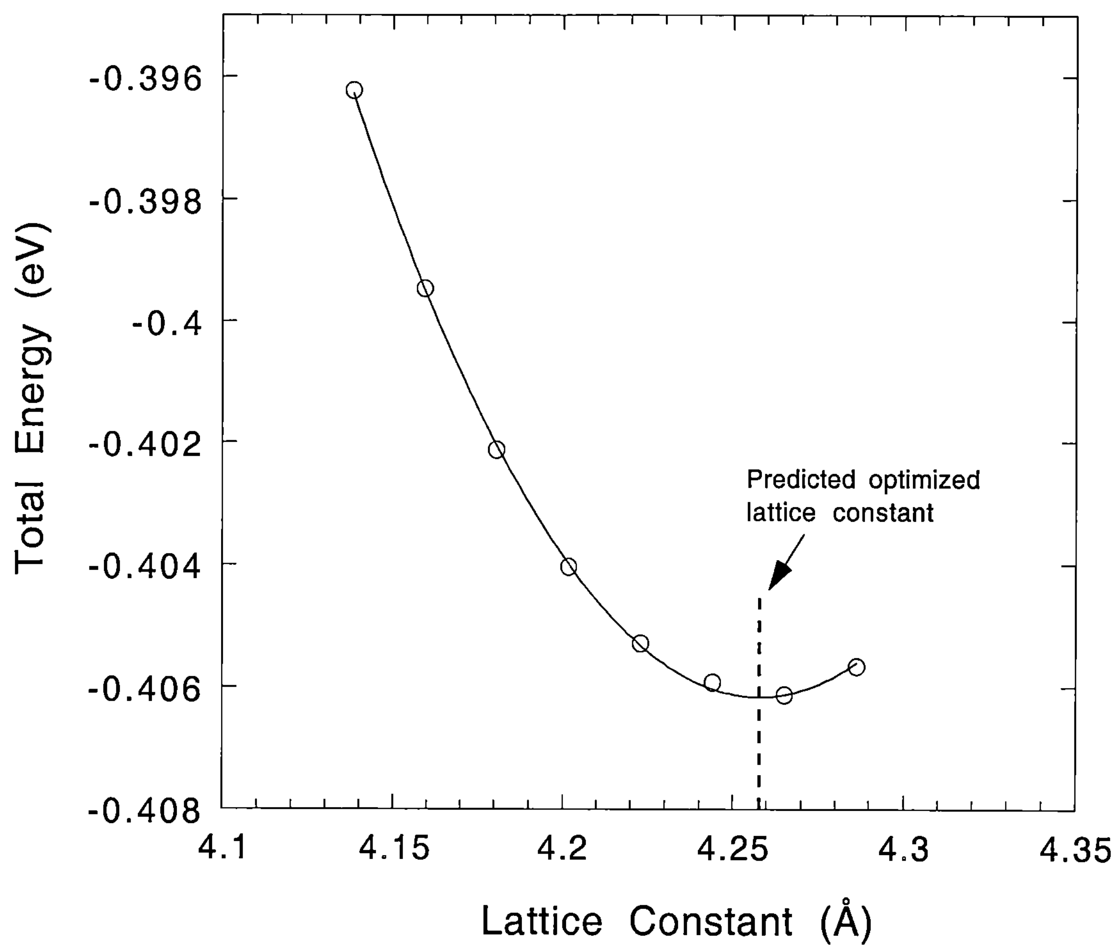

Figure 5.27. Theoretical determination of an equilibrium lattice constant by the GGA. The predicted lattice constant is determined by the minimum in the curve.

(a)

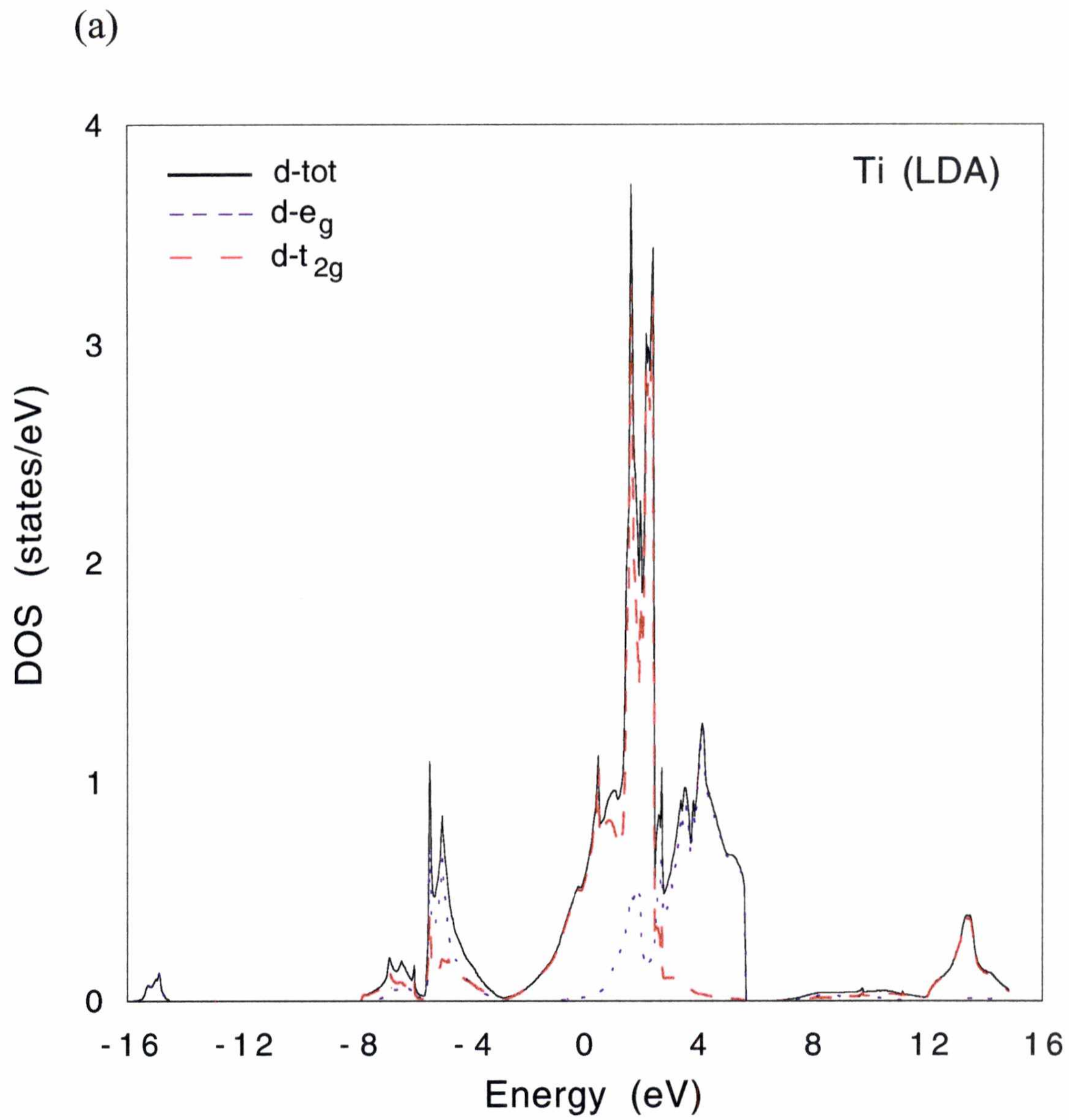

Figure 5.28. Calculated density of states (DOS) for TiN by LDA. (a) Ti.

(b)

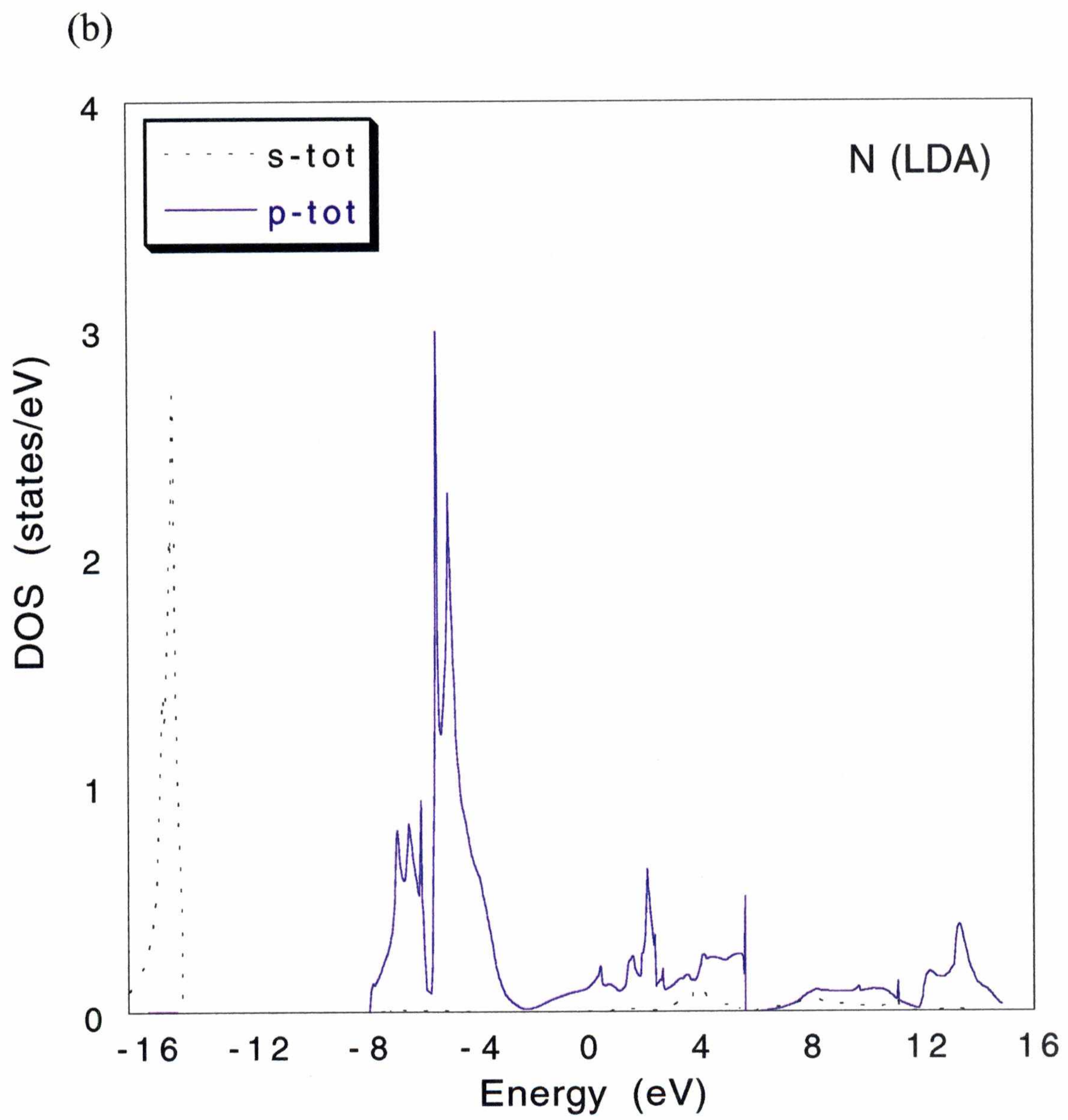

Figure 5.28. (continued) (b) N.

(a)

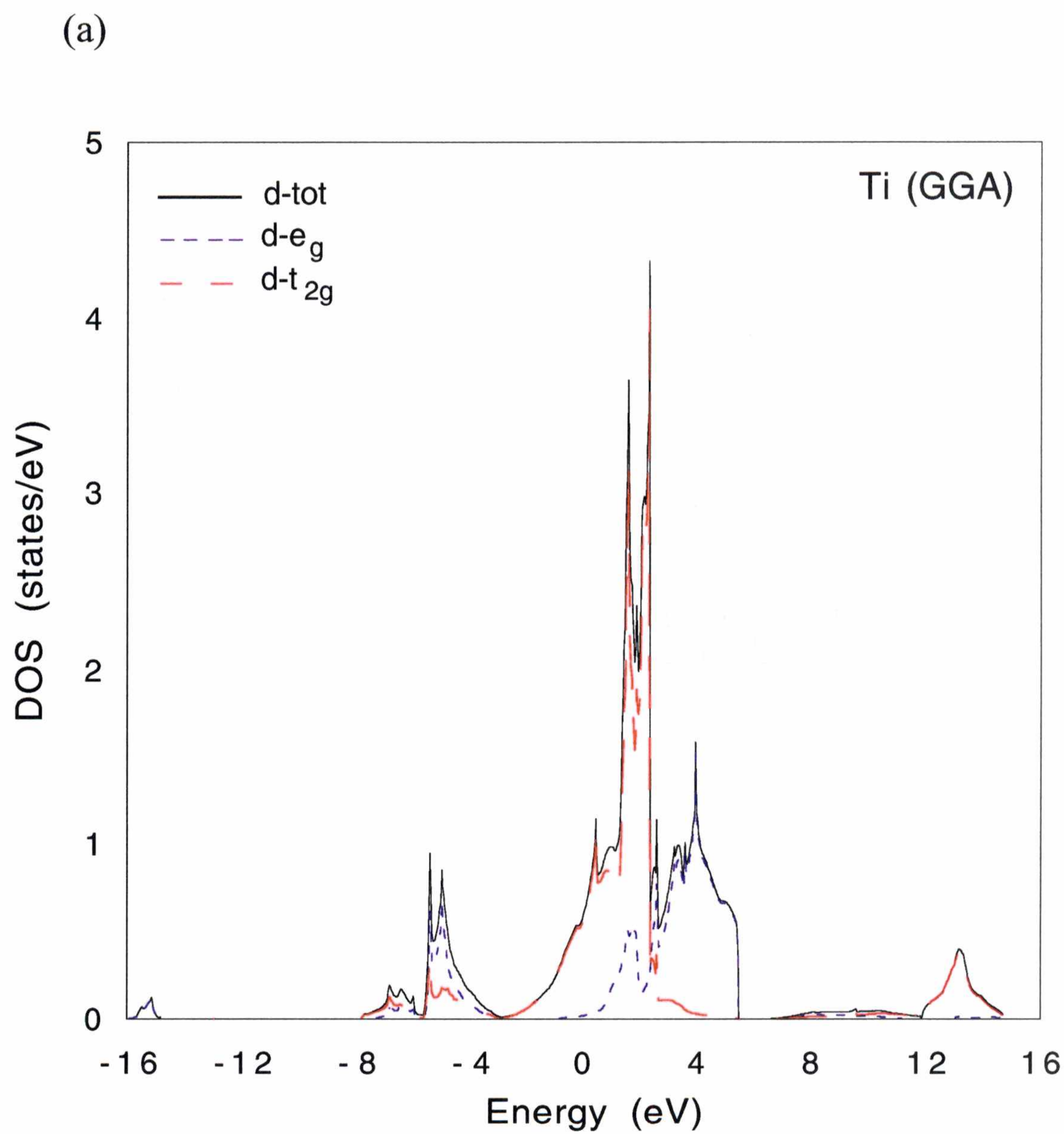

Figure 5.29. Calculated density of states for TiN by GGA. (a) Ti.

(b)

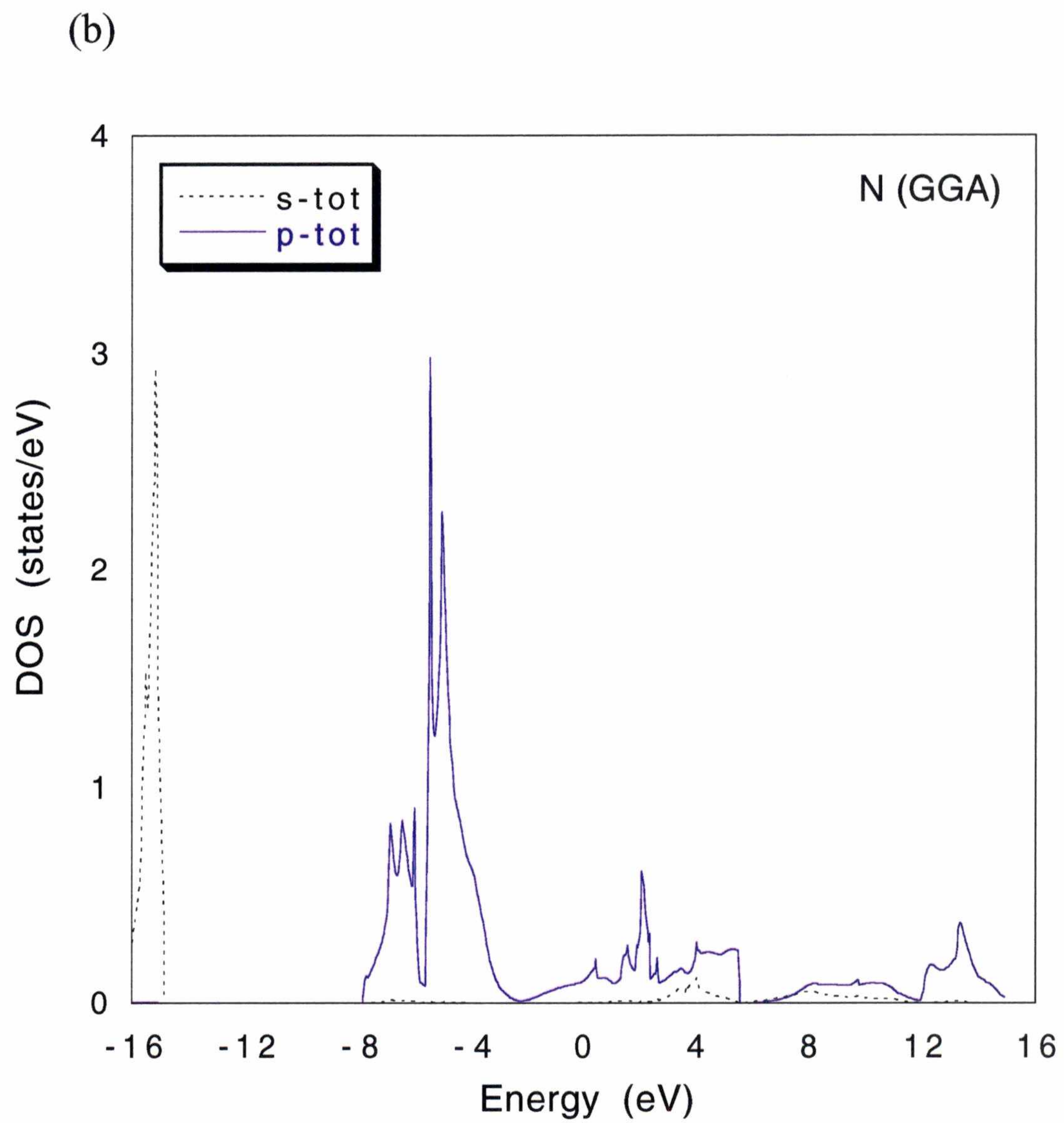

Figure 5.29. (continued) (b) N.

band, especially in the middle of the d-t_{2g} state. (The Fermi level lies on the sharply increasing peak that is mainly made up from the Ti d-t_{2g} states.) Therefore, the metallic property of TiN is dominated by this state originating from the transition metal atoms.

The experimentally obtained ELNES of the Ti-edge was shown previously in Fig. 5.25. The two peaks, d-t_{2g} and d-e_g, can be observed in the spectra and are separated by 2.67 eV (the experimental resolution was 1.3 eV full-width at half-maximum, FWHM). For comparison with theoretical calculations, the peaks in the DOS calculations were convoluted with an instrument broadening function (1.3 eV FWHM) and the result is shown in Fig. 5.30. As shown in the figure, the peak separation is 2.6 eV, in good agreement with the experimental value obtained previously. However, to make an exact quantitative comparison, the so-called Z+1 approximation[110] has to be employed. The approximation was not employed in the present research since it has a negligible effect for metals and metallic sample. We can see from the theoretical graphs (Fig. 5.28-Fig. 5.29) that the N-2*p* state and the Ti-3*d* state, especially Ti- d-e_g states, are strongly hybridized.

5.10. Electrical Resistivity Measurement and Analysis

One can describe the electrical conduction in metals using Matthiessen's Rule,[82] which is especially convenient in analyzing experimental data. This rule was suggested for bulk metals, but it is also valid for metallic films. The electrical resistivity of most common metals is dominated by collisions of the conduction electrons with vibrating

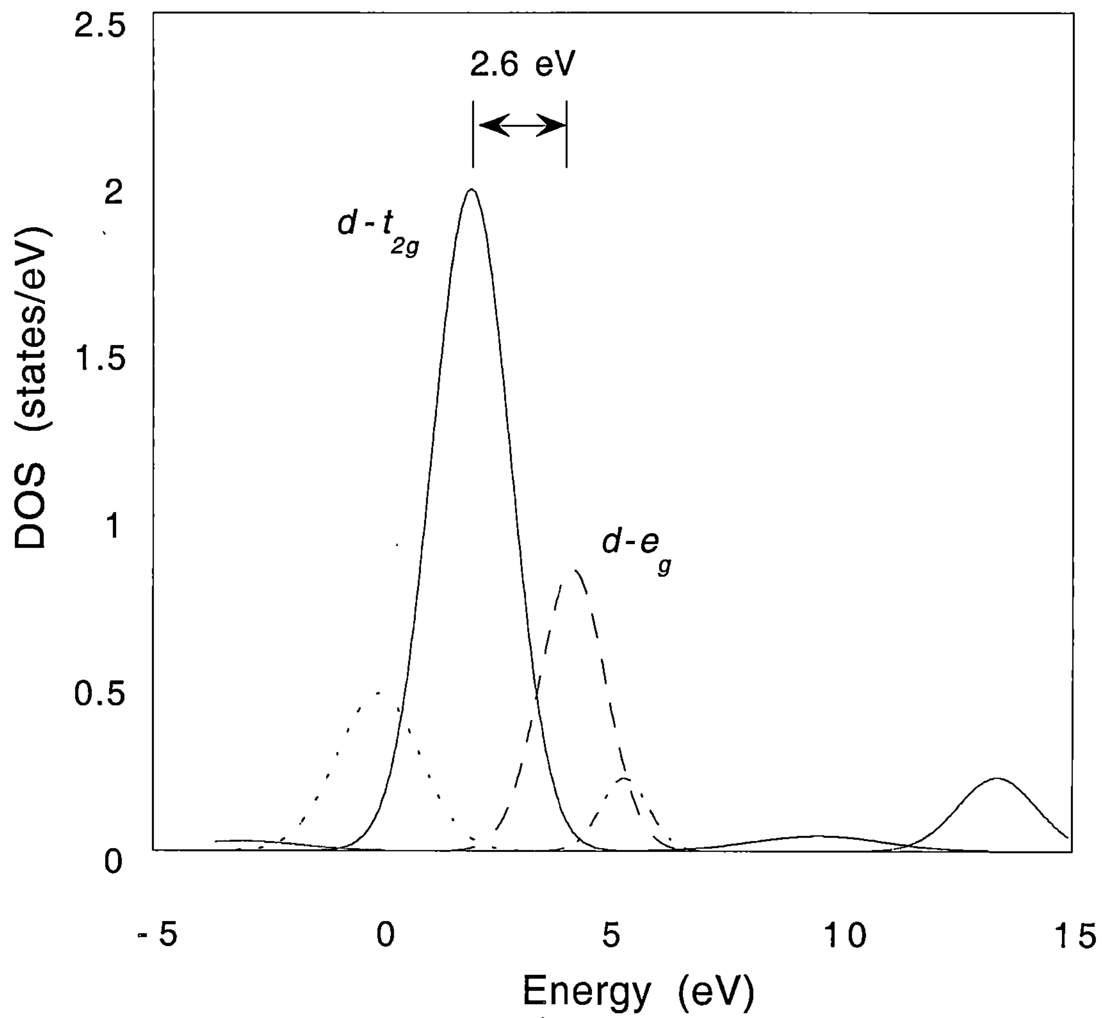

Figure 5.30. Convoluted density of states.

atoms (phonons) at room temperature and by collisions with impurity atoms and defects in the lattice at liquid helium temperature (4 K). Matthiessen's Rule simply states that the net resistivity is a sum of independent contributions of various electron-scattering processes. The total resistivity is given by[82]

$$\rho = \rho_L + \rho_i + \rho_d \tag{5.21}$$

where ρ_L, ρ_i, ρ_d, are resistivities caused by thermal phonons, impurities, and defects, respectively. Electron collisions with vibrating atoms are the source of the phonon (ρ_L) contribution and this effect increases rapidly with temperature. Defects, impurities, and grain boundaries locally disrupt the periodic electric potential of the lattice. Because of atomic valence and size differences at these singularities, electrons can be effectively scattered. It is observed often that ρ_L is independent of the number of impurities and defects when their concentration is low. Furthermore, ρ_i and ρ_d are independent of temperature. These empirical observations express Matthiessen's Rule and this is shown in Fig. 5.31 schematically.

Electrical resistivity measurements were performed using the Van der Pauw method with indium contacts. The temperature-dependent resistivity of a film grown at 750 °C and with different TOFs was measured from 10 K to 300 K and the results are shown in Fig. 5.32 (a) and 5.32 (b). All the samples showed metallic behavior, i.e. resistivity increased as temperature increased. This type of curve has been called a "universal" curve. Almost all of the pure elemental metals exhibit extended ranges of virtually linear resistivity-versus-temperature behavior at temperatures above about 0.2 of

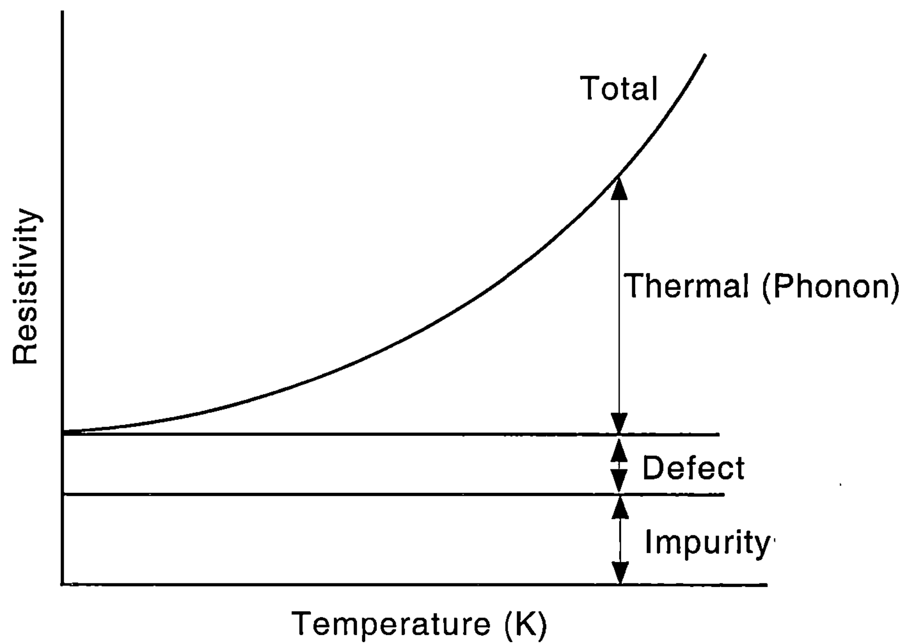

Figure 5.31. Schematic electrical resistivity variation as a function of temperature for a metal. Thermal (phonon), defect, and impurity contributions are shown.

(a)

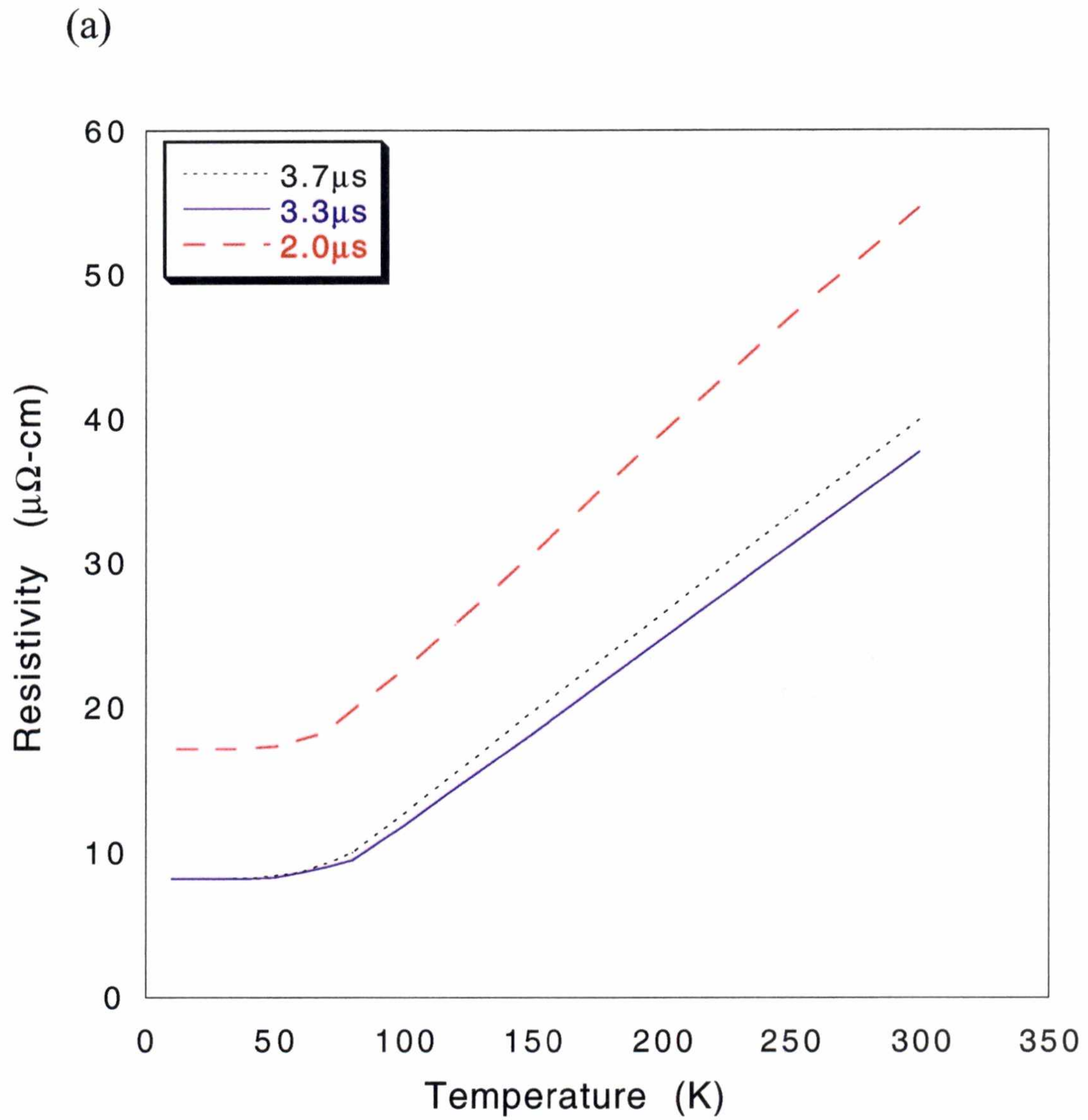

Figure 5.32 Resistivities as a function of temperature of TiN films grown (a) with 2.0, 3.3, and 3.7 s TOFs.

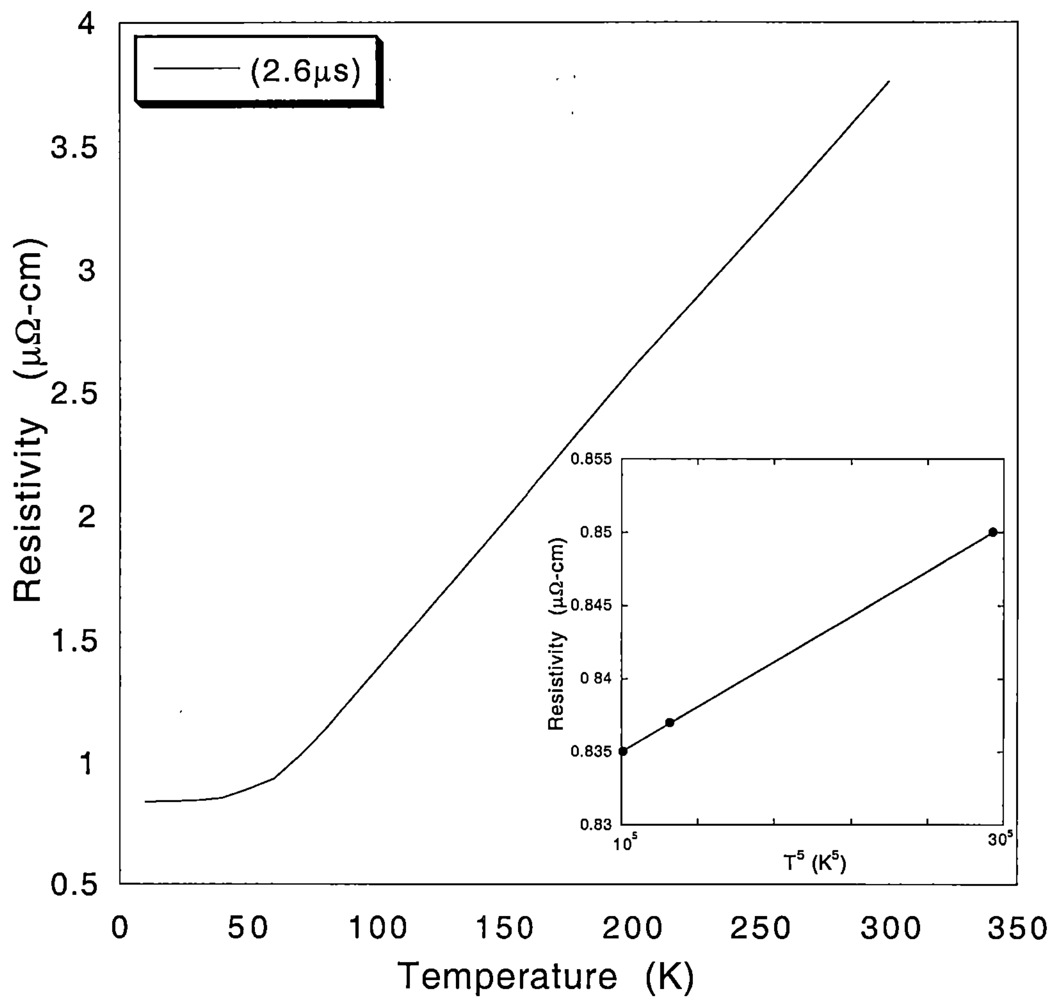

Figure 5.32. (continued) (b) with 2.6 μs TOF. Inset shows T^5 dependence at low temperatures.

the Debye temperature.[111] If we consider pure Ti metal (Debye temperature is 420 K), it can be expected that the linearity will occur beyond 84 K. In the higher temperature portion of the curve ($T \geq 71$ K), which is linearly varying with temperature, the temperature coefficient of resistivity (TCR), $d\rho/dT$, values were 0.1170 μΩ-cm/K, 0.0082 μΩ-cm/K, 0.0928 μΩ-cm/K, and 0.1084 μΩ-cm /K for the TiN films grown with 2.0 μs, 2.6 μs, 3.3 μs, and 3.7 μs TOF, respectively.

A wide range of room temperature resistivities are reported for TiN, ranging from 250 to more than 3000 μΩ-cm.[112] In the case of polycrystalline films, resistivity values are three times higher than single crystalline films [113] and these high resistivities were the result of grain boundaries, impurities, and sub-stoichiometry.[114] The previously reported lowest room temperature resistivity values of TiN films were 75 μΩ-cm (TiN/Si)[115], 20-25 μΩ-cm (TiN/Al_2O_3)[116], 18 μΩ-cm (TiN/MgO)[113], and 15 μΩ-cm (TiN/Si)[24].

The lowest room-temperature resistivity found here for TiN was 3.76 μΩ-cm (grown with a 2.6 μs TOF), which is very promising for contact metallization in advanced microelectronic devices, since this value is lower than any previously reported values. The resistivities of the TiN films decreased with decreasing temperature and approached their residual resistivity, $\rho_i(0)$, as T^5 approached 0 K. A linear relationship between resistivity and T^5 at cryogenic temperatures is shown in the inset of Fig. 5.32 (b). In this range, electron-electron scattering is important and the T^5 behavior may be altered by impurities.[111]

The resisitivity was observed to decrease as growth temperatures increased, while increasing resistivities were observed for increasing TOFs.

Generally, the resistivity was affected by preferred orientation, impurity content, microstructure of the film and film crystallinity. Since impurities were not detected from EDX and EELs analysis, the changes in resistivity are considered to be due to diffuse scattering of electrons from the film surface[82] and grain boundary scattering.[82,112] This conclusion is not unreasonable given the microstructures present in Figs. 5.15 and 5.17-5.19.

Chapter 6

CONCLUSION

6.1. Principal Results of This Work

High-quality single crystal TiN films have been grown epitaxially on Si(111) substrates using orthogonally crossed-beam reactive pulsed laser deposition. The following conclusions were drawn from this research.

(1) Orthogonally crossed-beam PLD, which is a modified version of conventional pulsed laser deposition, was demonstrated as a promising method to grow TiN films at moderate laser fluences and temperatures because of the enhanced reactivity caused by crossing the ablation plume with a pulsed-gas expansion. Singh's model was employed to explain scattering processes between the laser plume and the pulsed-gas expansion that were responsible for the enhanced reactivity in this pulsed laser deposition technique.

(2) An *in-situ* thermal cleaning method to obtain an atomically smooth and clean Si(111) substrate surface was developed. *In-situ* heating up to 900 °C was needed to obtain a clear, sharp, and streaky RHEED pattern indicating a two-dimensional surface structure. TiN films grown on substrates prepared in such a fashion exhibited superior electrical properties.

(3) Optimized growth conditions were developed and monitored by *in-situ* time-of-flight (TOF) measurements using an ion probe. TOFs of impinging species ranged from 2.0 to 3.7 μs, which corresponded to kinetic energies ranging from 155 eV to 45 eV, respectively. The crystallographic quality of the films was found to be a stronger function

of kinetic energy than of growth temperature, with optimal films resulting for a plume mean kinetic energy of ~92 eV.

(4) Optimal growth conditions (2.6 μs vacuum TOF) resulted in narrow X-ray rocking curve widths and mosaic spread values ($\Delta\omega$ =18 arc-min, $\Delta\phi$ =26 arc-min). To our knowledge, these are the lowest values reported to date for TiN films grown by any method.

(5) Surface morphology, film microstructure and growth mechanisms were investigated. Under optimal growth conditions, planar (2-D) epitaxial growth was maintained during the initial stages of growth and then the mode changed to island growth (Stranski-Krastanov growth mode). Three-dimensional growth modes were observed under slow-TOF conditions. The epitaxial relation between the film and the substrate was determined to be a result of domain-matching epitaxy with 9 units of TiN matching with 7 units of Si, which resulted in a 0.442 % effective mismatch.

(6) In general, low room-temperature resistivities were obtained. However, under optimum conditions a resistivity as low as 3.76 μΩ-cm was obtained and, to our knowledge, this is the lowest resistivity reported for TiN grown on any substrate. Consequently, such epitaxial TiN films might be used directly for contact metallurgy in advanced integrated circuit technology.

(7) EELS spectra confirmed the *absence* of oxygen at the interface between the TiN film and the Si substrate. The electron-loss near-edge structures also were compared with FLAPW calculations. The two peaks Ti d-t_{2g} and d-e_g were distinguished from the spectra with peak separation of 2.67 eV and agreed well with calculations.

(8) It is very important to control the growth conditions carefully to produce an appropriate environment for growing high quality epitaxial TiN films. In PLD, especially, more precise control of kinetic energies of the impinging species is important to promote surface diffusion.

6.2. Suggestions for Future Work

In this research, the growth conditions were mostly controlled by time-of-flight (TOF) measurements. However, time-of-flight quadrupole mass spectroscopy is needed to investigate scattering processes between the ablation plume and the gas pulse expansion and to identify impinging species on the substrate.

Although TiN thin films having the lowest resistivity to date were obtained in this research, the effect of defect structures on electrical properties should be investigated for high quality reliable devices, together with use of more nearly monoenergetic incident species in order to control defects, microstructure and properties.

References

REFERENCES

1. M. Y. Al-Jaroudi, H. T. G. Hentzell, S. E. Hornstrom, and A. Bengston, Thin Solid Films 190, 265 (1990).
2. T. Arai, H. Fujita, and M. Watanabe, Thin Solid Films 154, 387 (1987).
3. S. Kadlec, J. Musil, and J. Vyskocil, Surf. Coat. Technol. 54/55, 287 (1992).
4. M. Wittmer, B. Studer, and H. Melcion, J. Appl. Phys. 52, 5722 (1981).
5. N. Kumar, M. G. Fissel, K. Pourrezaei, B. Lee, and E. C. Douglas, Thin Solid Films 153, 287 (1987).
6. G. Gagon, J. F. Currie, G. Beique, J. L. Brebner, S. G. Dujrathi, L. Onellet, J. Appl. Phys. 75, 1565 (1994).
7. A. Sherman, Jpn. J. Appl. Phys. 30, 3553 (1991).
8. W. Li, X. He, H. Li, J. Appl. Phys. 75, 2005 (1994).
9. Y -I. Chen, J -G. Duh, Surf. Coat. Technol. 47, 371 (1991).
10. R. C. Glass, L. M. Spellman, S. Tanaka, and R. F. Davis, J. Vac. Sci. Technol. A 10, 1625 (1992).
11. C. M. Rouleau, S. Kang, and D. H. Lowndes, Appl. Phys. A 69, 441 (1999).
12. P. Tiwari, X. D. Wu, S. R. Foltyn, Q. X. Jia, I. H. Campbell, P. A. Arendt, R. E. Muenchausen, D. E. Peterson, T. E. Mitchell, and J. Narayan, Appl. Phys. Lett. 65, 2693 (1994).
13. S. Guha, and N. A. Bojarczuk, Appl. Phys. Lett. 72, 415 (1998).
14. A. Skerlavaj, Y. Claesson, and C. -G. Ribbing, Thin Solid Films 186, 15 (1990).

15. K. Antonova, et. al. Thin Solid Films 219, 157 (1992).

16. J. E. Greene, J. E. Sundgren, L. Hultman, I. Petrov, and D. B. Bergstrom, Appl. Phys. Lett. 67, 2928 (1995).

17. B. W. Karr, I. Petrov, D. G. Cahill, and J. E. Greene, Appl. Phys. Lett. 70, 1703 (1997).

18. P. Patsalas, C. Charitidis, S. Logothetidis, C. A. Dimitriadis, and O. Valassiades, J. Appl. Phys. 86, 5296 (1999).

19. U. C. Oh, J. H. Je, J. Appl. Phys. 74, 1692 (1993).

20. S. Ishihara, and M. Hanabusa, J. Appl. Phys. 84, 596 (1998).

21. Y. Tanaka, E. Kim, J. Foster, and Z. Xu, J. Vac. Sci. Technol. B 17(2), 416 (1999).

22. Y. Guoqing, C. Jingsheng, S. Ying, P. Haochang, Z. Dezhang, X. Hongjie, Z. Zhihao, Thin Solid Films 335, 59 (1998).

23. G. B. Smith, P. D. Swift, and A. Bendavid, Appl. Phys. Lett. 75, 630 (1999).

24. D. Craciun, and V. Craciun, Appl. Surf. Sci. 54, 75 (1992).

25. J. Narayan, P. Tiwari, X. Chen, J. Singh, R. Chowdhury, and T. Zhelva, Appl. Phys. Lett. 61, 1290 (1992).

26. R. Chowdhury, R. D. Vispute, K. Japannadham, and J. Narayan, J. Mater. Res. 11, 1458 (1996).

27. S. H. Kim, D. S. Chung, K. C. Park, K. B. Kim, and S. H. Min, J. Electrochem. Soc. 146, 1455 (1999).

28. R. Tobe, A. Sekiguchi, M. Sasaki, O. Okada, and N. Hosokawa, Thin Solid Films 281, 155 (1996).

29. H. M. Smith, and A. F. Turner, Appl. Opt. 4, 147 (1965).

30. H. Sankur, W. J. Gunning, J. Denatale, and J. F. Flintoff, J. Appl. Phys. 65, 2475 (1989).

31. R. Gross, P. Chaudhari, M. Kawasaki, M. B. Ketchen, and A. Gupta, Appl. Phys. Lett. 57, 727 (1990).

32. R. F. Xiao, H. B. Liao, N. Cue, X. W. Sun, and H. S. Kwok, J. Appl. Phys. 80, 4226 (1996).

33. P. Verardi, M. Dinescu, C. Gerardi, L. Mirenghi, and V. Sandu, Appl. Surf. Sci. 109-110, 371 (1997).

34. A. Gupta, B.W. Hussey, Appl. Phys. Lett. 58, 1211 (1991).

35. P. R. Willmott, R. Timm, P. Felder, and J. R. Huber, J. Appl. Phys. 76, 2657 (1994).

36. D. H. Lowndes, Experimental Methods in thr Physics Sciences, 30, 475 (1988).

37. H. Buhay, S. Sinharoy, and B. R. Lampe, The 4th International Symposium on Integrated Ferroelectrics, Monterey, March (1992).

38. A. V. Hamza, H. -P. Steinruck, J. J. Madix, J. Chem. Phys. 86, 6506 (1987).

39. J. E. Green , S. A. Barnett, J. E. Lundgren, and A. Rockett, Chapter 5 in Low Energy Ion/Surface Interactions During Film Growth, ed. By T. Itoh (Elsevier, Amsterdam 1988).

40. D. B. Chrisey, and G. K. Hubler, Pulsed Laser Deposition of Thin Films (John Wiley & Sons, New York, 1994).

41. B. Holzapfel, B. Roas, L. Schultz, P. Bauer, and G. Saemann-Ischenko, Appl. Phys. Lett. 61, 3178 (1992).

42. J. A. Greer, H. S. Kwok, Y. Kao, and D. Shaw, Superconductivity and Application (Plenum, New York, 1989) pp. 117-126.
43. K. B. Erington, and N. J. Ianno, Mater. Res. Soc. Proc. 191, 115 (1990).
44. M. Eddy, Fall Meeting of the Materials Research Society, Boston (1991).
45. R. K. Singh, and J. Narayan, Phys. Rev. B 41, 8843 (1990).
46. R. K. Singh, O. W. Holland, and J. Narayan, J. Appl. Phys. 68, 233 (1990).
47. R. Kelly, and R. W. Dreyfus, Surf. Sci. 198, 263 (1988).
48. R. F. Wood, and G. E. Giles, Phys. Rev. B 23, 2923 (1981).
49. R. K. Singh, and J. Narayan, Mater. Sci. Eng. B 3, 217 (1989).
50. T. Venkatesan, X. D. Wu, A. Inam, and J. B. Watchman, Appl. Phys. Lett. 52, 1193 (1987).
51. U. Sudarshan, N. W. Cody, M. J. Bozack, and R. Solanki, J. Mater. Res. 3, 825 (1988).
52. P. R. Willmott, and J. R. Huber, Rev. Mod. Phys. 72, 315 (2000).
53. J. F. Ready, Effects of High Power Laser Radiation (Academic, New York, 1971).
54. Zel'dovich, and Raizer, Physics of Shock Waves and High Temperature Phenomena (Academic, New York, 1966).
55. J. Narayan, W. L. Brown, R. A. Lemons, Eds., Laser-Solid Interactions and Transient Thermal Processing (North-Holland, New York, 1984).
56. F. F. Chen, Introduction to Plasma Physics (Plenum, New York, 1974).
57. J. M. Dawson, Phys. Fluids 7, 981 (1964).
58. J. Dawson, P. Kaw. And B. Green, Phys. Fluids 12, 875 (1969).

59. A. Caruso, and R. Gratton, Plasma phys. 10, 867 (1968).

60. N. G. Basov, V. A. Boiko, V. A. Dement'ev, O. N. Krokhin, and G. V. Skilikov, Sov. Phys JEPT 24, 659 (1967).

61. A. F. Haught, and D. H. Polk, Phys. Fluids 9, 2047 (1966).

62. W. L. Fader, Phys. Fluids 11, 2200 (1968).

63. T. P. Hughes, Plasmas and Laser Light (Wiley, New York, 1975).

64. B. Chapman, Glow Discharge Process (Wiley-Interscience, New York, 1980).

65. T. Terashima, K. Iijima, K. Yamamoto, Y. Bando, and H. Mazaki, Jpn. J. Appl. Phys. 27, 191 (1988).

66. R. W. Dreyfus, J. Appl. Phys. 69, 1721 (1991).

67. L. Wiedeman, and H. Helvajian, J. Appl. Phys. 70, 4513 (1991).

68. D. B. Geohegan, in Laser Ablation Mechanisms and Applications (Springer-Verlag, New York, 1991) p.29.

69. D. Sibold, and H. M. Urbassek, Phys. Fluids 16, 1149 (1973).

70. R. Kelly, A. Miotello, B. Braren, A. Gupta, and K. Casey, Nucl. Instrum. Methods Phys. Res. B 65, 187 (1992).

71. P. A. Thompson, Compressible Fluid Dynamics (McGraw Hill, New York, 1972) p. 397.

72. D. B. Geohegan, in Laser Ablation in Material Processing: Fundamentals and Applications, edited by B. Braren, J. J. Dubowski, and D. P. Norton, MRS Symposia Proceedings No. 285 (Materials Research Society, Pittsburgh, 1993) p. 27.

73. I. Weaver, J. Appl. Phys. 79, 7216 (1996).

74. D. K. Brice, J. Y. Tsao, S. T. Picraux, Nucl. Instrum. Methods B 44, 68 (1989).

75. P. Rabinzohn, G. Gautherin, B. Agius, and C. Cohen, J. Electrochem. Soc. 131, 905 (1984).

76. J. H. Comport, L. M. Garverick, and R. Reif, J. Appl. Phys. 62, 3388 (1987).

77. W. R. Burger, R. Reif, J. Appl. Phys. 62, 4255 (1987).

78. R. F. Wood, J. N. Leboeuf, K. R. Chen, D. B. Geohegan, A. A. Puretsky, Appl. Surf. Sci. 127-129, 151 (1998).

79. D. E. Powers, S. G. Hansen, M. E. Geusic, A. C. Pulu, J. B. Hopkins, T. G. Dietz, M. A. Duncan, P. R. R. Langridge-Smith, R. E. Smally, J. Phys. Chem. 86. 2556 (1982).

80. P. R. Willmott, R. Timm, and J. R. Huber, J. Appl. Phys. 82, 2082 (1997).

81. J. D. Swift, M. J. R. Schwar, Electrical Probes for Plasma Diagnostics, Iliffe, London (1970).

82. M. Ohring, The Materials Science of Thin Films, (Academic Press, 1992).

83. B. D. Cullity Elements of X-ray Diffraction, (Addison-Wesley, London,1978).

84. J. L. Jordon-Sweet, IBM J. Res. Develop. 44, 457 (2000).

85. L.J. Van der Pauw, Philips Res. Repts. 13, 1 (1958).

86. E. Bauer, Techniques of Metal Research (Interscience, New York, 1969), Vol. II, Part 2, p.502.

87. K.-T. Tu, J. W. Mayer, L. C. Feldman, Electronic Thin Film Science for Electrical Engineers and Materials Scientists (Macmillan, New York, 1992).

88. E. Bauer, Appl. Surf. Sci. 11/12, 479 (1982).

89. L. Hultman, H. Ljungcrantz, C. Hallin, E. Janzen, J-E. Sundgren, B. Pecz, and L. R.

Wallenberg, J. Mat. Res. 11, 2458 (1996).

90. P. R. Willmott, R. Timm, J. R. Huber, Appl. Surf. Sci. 127-129, 105 (1998).
91. K. Sano, M. Oose, and T. Kawakubo, Jpn. J. Appl. Phys. 34, 3266 (1995).
92. A. A. Iliadis, S. N. Andronescu, K. Edinger, J. H. Orloff, R. D. Vispute, V. Talyanky, R. P. Sharma, T. Venkatesan, M. C. Wood, and K. A. Jones, Appl. Phys. Lett. 73, 3545 (1998).
93. Van de et al. : E. van de Riet, U.K.P. Biermann, and J. Dieleman, Thin solid films 241, 13 (1994).
94. J. F. Young, J. E. Sipe, and H. M. van Driel, Phys. Rev. B 30, 2001(1984).
95. J. D. Fowlkes, A. J. Pedraza, and D. H. Lowndes, Appl. Phys. Lett. 77, 1629 (2000).
96. T. Zheleva, K. Jagannadham, and J. Narayan, J. Appl. Phys. 75, 860 (1994).
97. J. -S. Chun, I. Petrov, and J. E. Greene, J. Appl. Phys. 86, 3633 (1999).
98. R. D. Vispute, J. Narayan, K. Dovidenko, K. Jagannadham, N. Parikh, A. Suvkhanov, and J. D. Budai, J. Appl. Phys. 80, 6720 (1996).
99. P. D. Nellist, and S. J. Pennycook, Advances in Imaging and Electron Physics, 113, 147 (2000).
100. D. E. Jesson, and S. J. Pennycook, Incoherent Imaging of Crystals using Thermally Scattered Electrons, Proc. Roy. Soc. A449, 273 (1993).
101. S. J. Pennycook, and D. E. Jesson, Ultramicro. 37, 14 (1991).
102. R. F. Egerton, Electron Energy-Loss Spectroscopy in the Electron Microscope, 2nd ed. (Plenum Press, New York ,1996).
103. P. Hohenberg, and W. Kohn, Phys. Rev. 136, B864 (1964).

104. W. Kohn and L. J. Sham, Phys. Rev. 140, A1333 (1965).

105. P. Blaha, K. Schwarz, and J. Luitz, WIEN97, K. Schwarz, Vienna University of Technology, Vienna 1999 The original copy-righted WIEN-code, which was published by P. Blaha, K. Schwarz, P. Sorantin, and S. B. Trickey, in Comput. Phys. Commun. 59, 399 (1990).

106. R. G. Parr, and W. Yang, Density Functional Theory of Atoms and Molecules (Oxford University Press, New York, 1989).

107. J. P. Perdew, and Y. Wang, Phys. Rev B 33, 8800 (1986).

108. R. Ahuja, O. Eriksson, J. M. Wills, and B. Johansson, Phys. Rev. B, 53,3072 (1996).

109. M. C. Payne, M. P. Teter, D. C. Allan, T. A. Arias, and J. D. Joannopoulos, Rev. Mod. Phys. 64, 1046 (1992).

110. S. Köstlmeier, and C. Elsässer, Phys. Rev. B, 60, 14025, (1999).

111. D. D. Pollock, Electrical Conduction in Solids : An Introduction (American Society for Metals, New York, 1985).

112. P. Leclair, G. P. Berera, and J. S. Moodera, Thin Solid Films, 376, 9 (2000).

113. B. O. Johansson, J. -E. Sundgren, J. E. Greene, A. Rockett, and A. Barnett, J. Vac. Sci. Technol. A, 303 (1985).

114. L. E. Toth, Transition Metal Carbides and Nitrides, (Academic Press, New York, 1971).

115. H. Jeon, J. -W. Lee, Y. -D. Kim, D. -S. Kim, and K. -S. Yi, J. Vac. Sci. Technol. A 18, 1595 (2000).

116. R. D. Vispute, V. Talyansky, R. P. Sharma, S. Choopun, M. Downes, T. Venkatean, Y. X. Li, L. G. Salamanca-Riba, A. A. Iliadis, K. A. Jones, and J. McGarrity, Appl. Surf. Sci. 127-129, 431 (1998).

VITA

Sukill Kang was born in Jeonju, the southern part of Korea on December 17, 1965. He attended the Jeonbuk National University, from 1984 to 1988, where he received his Bachelor of Science degree in Physics. He admitted to the graduate school of the Western Illinois University, Macomb, IL and earned his Master of Science degree in 1995. In the fall of 1995, he entered the graduate school of Physics and Astronomy in the University of Tennessee, Knoxville. In 1998, he worked as a professional intern for Semiconductor physics, thin films and photovoltaic materials group in Oak Ridge National Laboratory. He worked on oxides and nitrides thin films growth and also on nanostructured materials processing. He will continue his career as a post-doctoral fellow in metal and ceramic division at Oak Ridge National Laboratory.